Development of a coupled numerical-experimental facility to model the fluid-structure interactions of the human vocal folds

by

David E. Sommer

A thesis
presented to the University of Waterloo
in fulfillment of the
thesis requirement for the degree of
Master of Applied Science
in
Mechanical Engineering

Waterloo, Ontario, Canada, 2014

I hereby declare that I am the sole author of this thesis. This is a true copy of the thesis, including any required final revisions, as accepted by my examiners.

I understand that my thesis may be made electronically available to the public.

Abstract

Voiced speech is a complex process that involves the exchange of energy between the air flow from the lungs and the elastic tissue of the vocal folds. Accurate modelling of the fluid-structure interactions of speech is paramount to understand the physical phenomena. These interactions have been studied with both experimental and numerical models. Numerical models of speech rely on over-simplified models to describe the airflow, while experimental investigations fail to accurately capture the energy exchange from the fluid to the tissue. To address these shortcomings, a coupled numerical-experimental facility is proposed for modelling speech, where the tissue is solved numerically and fluid pressure on the folds is measured experimentally in real-time.

Fifteen times physiological scale mechanical models of the vocal folds are instrumented with pressure sensors to record the spatial pressure distribution over the surface of the model. A propylene glycol solution, with a viscosity of $\mu = 0.01$ Pa s, is selected as the working fluid to allow for matching of the Reynolds, Euler, and Strouhal numbers. A motion system independently actuates each vocal fold model to replicate the two primary modes of physiological vocal fold motion. A real time controller reads the pressure distribution on the vocal fold model surface, scales it to physiological levels, and applies the loading to the Steinecke and Herzel two-mass numerical model of the vocal folds. The response is calculated at each time step under the current pressure loading. The resulting position and velocity outputs are scaled up to experimental size and the vocal fold models are moved accordingly.

A custom constant pressure differential flow tunnel is constructed from fibreglass to provide flow through the vocal fold models. The flow of water through the empty test section of the tunnel shows the axial velocity is spatially uniform within 10% and the temporal fluctuations are 6.8% at the middle of the test section. Installing the vocal fold models, with their inherent contracting geometry, the temporal fluctuations in the flow are reduced to 2.4%. These variations are likely to be reduced when the more viscous glycol working fluid is used.

The facility is tested with experiments of incrementally increasing complexity to validate its operation. A single degree of freedom step response test and wind tunnel test characterize the dynamical response to pressure changes. Modelling the response of a single vocal fold model loaded by an impinging jet validates motion system and control algorithms. Flow through the vocal fold models installed in the test section in static and driven configuration exhibit representative flow behaviour as compared to prior studies. These tests demonstrate the facility's ability to model the fluid-structure interactions of human speech with unprecedented levels of control and flexibility.

Acknowledgements

I would like to thank my supervisor, Professor Sean Peterson, for his unwavering support in all my pursuits, academic and otherwise. You are an excellent scientist and a great friend.

I would also like to acknowledge the invaluable assistance of the technicians at the University of Waterloo Engineering Machine Shop for their creativity and expertise; you saved me endless hours of trying to do things the wrong way. I would especially like to thank Rick Forgett and Phil Laycock for their invaluable discussions and for their patience with my endless stream of questions.

Most of all, I would would like to thank my father Steve. You instilled the desire for learning and understanding at a young age and have worked tirelessly ever since to support me in its pursuit.

Table of Contents

List of Figures

Chapter 1

Introduction

Research interest in the field of human phonation is primarily motivated by the desire to garner improved physical understanding of the mechanics of human speech and to apply this knowledge to diagnose and treat individuals suffering from speech disorders. The prevalence of voice disorders in the general population is approximately 30% over a lifetime and even higher in professions that have higher vocal demands [1]. Improved methods to model the complex physical interactions that give rise to human speech are necessary to further the field, with the ultimate goal of improved diagnosis and treatment of speech disorders. Of particular interest, is the coupled energy exchange between the airflow from the lungs and the viscoelastic tissue of the vocal tract. A novel experimental facility is proposed to attempt to address the limitations of existing models.

1.1 Background

The production of human speech has been shown to be the result of complex coupled physical interactions between the air flow from the lungs, the tissues of the vocal tract, and the acoustic field that we perceive as speech [2–4]. To understand these interactions, and the research efforts made to reveal and characterize them, a brief background is presented in this section. The basic anatomy of the tissues of the vocal tract and their motions during speech are described.

1.1.1 Fundamentals of the anatomy of human speech

To make communication of anatomical concepts easier, the standard anatomical terms describing location are shown in Figure 1.1. These terms will be used when referring to the anatomy of the vocal folds and throughout the remainder of this chapter. Although this standard is used consistently in the literature, coordinate systems more typical of mathematical systems are employed in later chapters as they are better suited to the analytical framework.

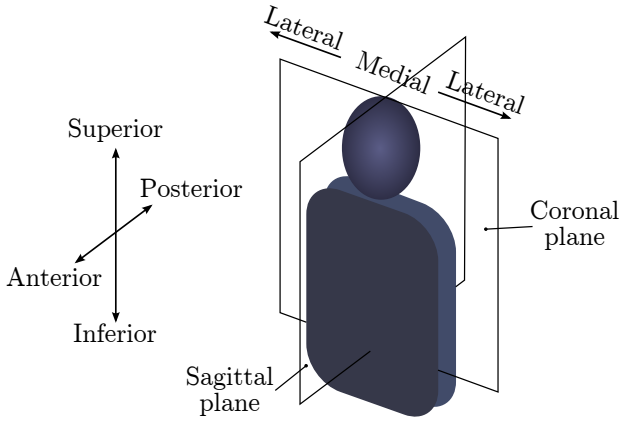

Figure 1.1: Anatomical terms of location for a human faced towards the reader.

As seen in Figure 1.1, the coronal plane forms a slice that splits the body into an anterior and posterior half. A coronal section of the neck reveals the anatomy of the larynx, shown in Figure 1.2a). Air flows from the lungs via the trachea and is forced through the narrow gap between the vocal folds, known as the glottis, and continues in the superior direction in the supraglottal tract towards the mouth. The fundamental sound source of human speech has been demonstrated to be caused by the pulsatile flow of air through the glottis. Pulsatile flow arises due to a coupled energy exchange between the airflow from the lungs and the viscoelastic nature of the vocal fold tissue [4]. The now widely accepted myoelastic theory of phonation suggests the pulsatile glottal flow arises from self-sustained oscillations of the elastic tissue of the vocal folds, acting as a passive oscillator, excited by the energy provided by the airflow from the lungs [4, 5].

Figure 1.2b) shows a close up view of the medial surface of the left vocal fold, revealing the three primary tissue layers that make up the folds. The medial surface, the surface of

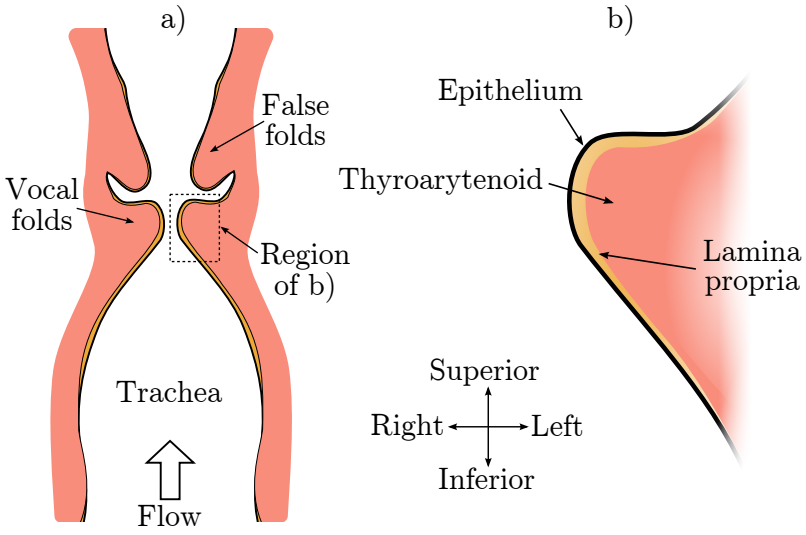

Figure 1.2: Anatomy and physiology of human voice production. a) A cross-section in the coronal plane through the larynx, and b) close up section of the vocal fold anatomy showing the three primary tissue layers that make up the vocal folds.

the vocal folds in contact with the air flow from the lungs, is coated with a thin epithelium. The lamina propria sits beneath the epithlium, and together the two tissues form what is collectively referred to as the mucosa [6]. The mucosa stretches over the thyroarytenoid muscle, which constitutes the majority of the bulk of the vocal fold. The mucosa and underlying muscle are not rigidly attached, rather the mucosa sits loosely over the thyroarytenoid, similar to how the scalp sits on the head [2, 7].

1.1.2 Motion of the vocal folds

Anatomical interest aside, the layered composite structure of the vocal folds plays a crucial role in determining their dynamics. The loosely fitting mucosa on the stiffer underlying muscle is key to the efficient transfer of energy from the airflow to the tissue. The vibration of the vocal folds is complex and has been shown to demonstrate highly non-linear and chaotic behaviour [8, 9]. Despite this, both experimental [10] and numerical [11] models of the vocal folds have shown that the first two eigenmodes contain more than 85% of the energy of vibration during model voice. This is consistent with what is observed in voice; a strong periodic signal modulated with an underlying small amplitude chaotic component

[8]. The two primary eigenmodes are, as depicted in Figure 1.3, a bulk displacement in the medial-lateral direction, and a rotation of the medial surface in the coronal plane.

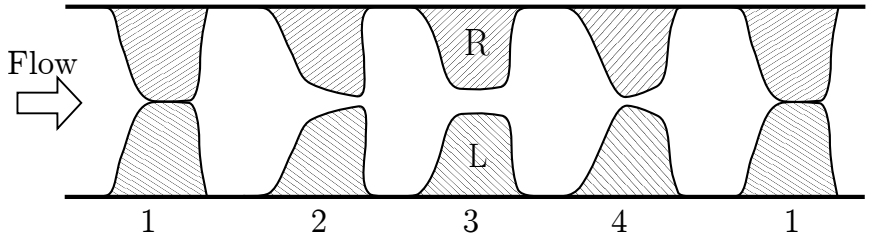

Figure 1.3: Coronal section of the vocal folds showing the primary motion through one phonatory cycle of a healthy speaker. Adapted from [12].

At the beginning of a phonatory cycle, with the vocal folds beginning in contact as shown in frame 1 of Figure 1.3, elevated subglottal pressure causes a net force to act to deform the vocal folds in the medial-lateral direction, as well as slightly in the inferior-superior direction. The glottis opens slightly to form a converging duct, which can be seen in frame 2 of Figure 1.3. A converging glottis accelerates the air smoothly and a centrally oriented jet emerges from the glottal exit [3]. After fully opening, the restorative force of the elastic tissue begins to close the glottis. A divergent duct, as shown in frame 4 of Figure 1.3, forms during the closing phase. In the divergent duct, the glottal jet exhibits asymmetric flow attachment with a bimodal distribution to either side [3]. The transition from a convergent to divergent glottis is referred to as the mucosal wave. The mucosal wave is hypothesized to be a key factor in the self-sustained oscillation of the vocal folds, and has been shown to increase the efficiency of energy transfer from the air to the tissue [5,13].

The bulk oscillation of the vocal folds, visible when viewed from the superior direction has been well characterized since a laryngoscope was first used to view the glottis in the mid 1850s, and captured with video in the 1950s [14]. The mucosal wave, more difficult to observe from directly above, has been observed in excised larynges [10], in animal layrnges [15], and also *in vivo* in humans with laser techniques [16] and 3-D stereo-endoscopy [17]. See Sommer et al. [17] for a more comprehensive review of measurement of the vocal fold dynamics.

1.2 Current state of the art

Investigations into the fluid structure interaction of human speech hitherto can be broadly characterized into two basic categories: numerical and experimental. An overview of the two model categories, both with their respective advantages and disadvantages, is provided in the following sections. This section is not intended as an exhaustive review of the literature, only of sufficient depth to motivate and give context to the present work.

1.2.1 Experimental flow studies

Experimental investigations of glottal flows have been formally pursued since at least the 1930s. Flow through simplified glottal geometries were considered in an effort to understand the pressure drop of airflow across the glottis and the fluid structure interaction with the vocal folds [18, 19]. Experimental studies offer the advantage of physically accurate flow but the difficulties lie in relevantly representing the glottal geometry, measuring the quantities of interest, and incorporating the coupled interaction of the flow and the dynamic vocal fold structure.

1.2.1.1 Rigid glottal duct flow studies

Studies of the flow through rigid ducts intended to resemble the geometry of the glottis were the earliest studies of the fluid dynamics of speech and are still on going. Early experiments of Wegel consisted of a simple brass tube with brass plates forming a slit of variable width [19]. Van den Berg constructed duct representations of the larynx with dimensions based roughly on castings from a normal cadaveric larynx [18]. The geometry of experimental glottal models has been refined considerably from the original simple rectangular representation towards more physiologically relevant shapes [20]. Scherer et al. [21] tested the glottis in different configurations and compared to earlier works, in pursuit of a more satisfactory glottal geometry. The M5 geometry proposed by Scherer et al. [22] is used frequently in rigid glottal duct flow studies and also for synthetic self oscillating studies, discussed in Section 1.2.1.4. The obvious limitation of rigid glottal flow studies is the lack of consideration given to the dynamic motion of the vocal folds, and the subsequent pulsatile flow that arises.

1.2.1.2 Pulsatile flow studies

Pulsatile flow studies are a relatively simple way to incorporate the transient nature of the flow into rigid glottal models. Originally, the behaviour of the glottal jet, specifically the occurrence of the Coanda effect, observed in rigid models was believed to be an artefact of the non-physiological steady flow [23, 24]. The investigators reached this conclusion by proposing that, during the phonatory cycle, there was insufficient time for the asymmetric flows to develop. However, this was later disproved by a pulsatile flow facility more dynamically similar to physiological flows [25]. Pulsatile facilities, while capturing the transient nature of the flow, do not capture the effects of the moving boundaries of the changing glottal geometry.

1.2.1.3 Driven vocal fold model studies

Driven models of the vocal folds seek to incorporate the motion of the vocal folds, particularly the changing glottal area, when making observations of the flow behaviour. Driven models capture one half of the fluid-structure interaction; that is, the motion of the structure affects the fluid but the pressure field of the fluid has no effect on the dynamics. The importance of transient flow and the effects of the moving wall have been elucidated by driven vocal fold studies, ranging from a simple cam driven orifice [26] to independently actuated multiple axes vocal fold motion [27]. An advantage of driven models is they can be scaled above physiological size and slowed below physiological vibration rates to afford measurement access while still maintaining the relevant flow physics, as discussed in more detail in Section 2.1.1. Particle image velocimetry (PIV) has been used to measure the time resolved spatial velocity distribution in driven vocal fold models, giving detailed spatial and temporal resolution of the flow field [27, 28].

Although an advantage over static and pulsatile flow experiments, driven models do not capture the causal energy exchange of human speech. Energy is supplied by the air flow from the lungs and the vocal folds act as passive oscillators. In the case of driven models, the models may impart energy on the flow at some points in the phonatory cycle. The impact of neglecting the coupled nature of the fluid and structure in driven models has yet to be well isolated.

1.2.1.4 Self-oscillating synthetic models

Synthetic models of the vocal folds can be manufactured from viscoelastic engineered materials such as polyurethane [13] and silicone rubber [29]. They are cast into the vocal fold

shape, such as the M5 geometry [5, 30], and flow is supplied from a pressurized reservoir. The models undergo a self-oscillation, similar to that of the vocal folds. Self-oscillating synthetic models are limited in that they must be one-to-one physiological scale. The mechanical properties of the tissue, or synthetic analogue, do not scale as the governing flow physics do. Restriction to physiological scale obfuscates observation and measurement at fast oscillations and small length scales. Furthermore, fabricated synthetic models do not offer the ease of parametric studies that numerical studies and driven experimental studies do, as a new model must be constructed for each set of parameters. PIV measurements of the flow structures superior of the glottis have been made in self oscillating synthetic models [30], but the small scale and inaccessibility precludes detailed observations within the glottis.

1.2.2 Numerical flow studies

Numerical models of the vocal fold dynamics have root in the 60's when computers were first used to model the coupled motion of the vocal folds as well as the acoustics of the vocal tract [31] and have now grown to full high fidelity and fully coupled models of an individual's anatomy [11]. These simulations attempt to model both the tissue vibration and the air flow to gain insight into the fluid-structure coupling and resulting vocal fold dynamics. The evolution of numerical modelling of the vocal fold dynamics is briefly captured in the following sections; progressing from reduced order tissue models with 1-D inviscid flow solutions, reduced order models with improved flow solutions, and to reduced order and higher order models with computational fluid dynamics solutions of flow.

1.2.2.1 Reduced order tissue models

As discussed in Section 1.1.2, two primary modes capture the majority of the energy of vibration of the vocal folds. Ishizaka and Flanigan [31] first proposed the use of two spring-mass-damper oscillators to capture the two primary modes of the vocal fold motion, known as a two-mass model (2MM). As shown in Figure 1.4a), the two masses have springs and dampers to capture the viscoelastic nature of the vocal fold tissue as well as a third spring to connect the two masses. Two masses are used to model each of the left and right vocal folds. Aerodynamic forces are applied to the surface of the masses by solving the pressure loading through the glottis. A 1-D inviscid solution is used to model the pressure based purely on the minimum area between the masses. These 2MM have since been extended to multi-mass models, demonstrated in Figure 1.4c), that can have any number of masses in the inferior-superior and left-right direction [32, 33]. Furthermore, multi-mass models

with more than one level have also been employed in an effort to recreate the anatomical structure of the vocal folds [34]. A full review of reduced order models can be found in [2].

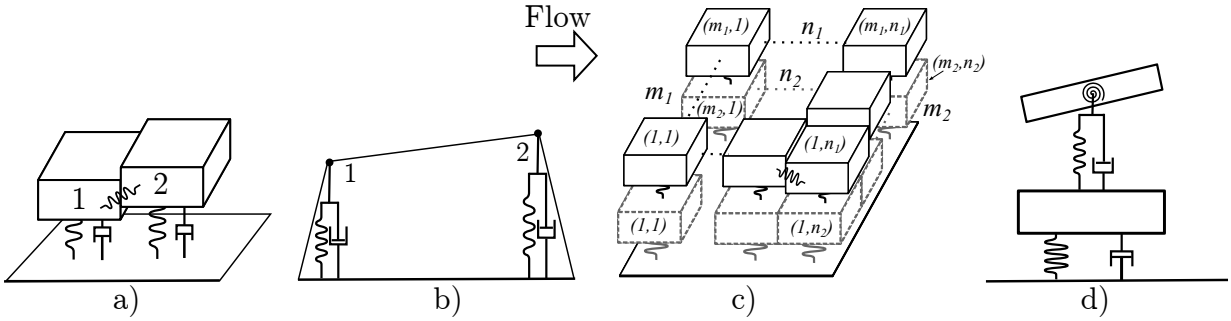

Figure 1.4: An overview of the common types of reduced order numerical models of the vocal fold tissue. Adapted from [2].

The original 2MM used non-linear springs in an attempt to better simulate the mechanical properties of tissue. Steinecke and Herzel [35], simplified the 2MM with linear springs and demonstrated that much of the same behaviour is observed. Steinecke and Herzel also introduced an asymmetry factor Q, allowing for different mass, spring, and dampening values between the left and right vocal fold models. The asymmetry parameter is useful in modelling the asymmetries observed in healthy speakers and especially for modelling unilateral paralysis, where one side of the glottis will suffer damage to the innervation [2,35]. For different subglottal pressure P_s, the pressure supplied from the lungs, and asymmetry factor Q the dynamics of the 2MM were shown to be rich and complex. A vibration regime map of the Steinecke and Herzel 2MM is shown in Figure 1.5a), taken from Sommer et al. [36]. In these regime maps, the ratios shown, such as 1:2, indicate the number of maxima of the right mass versus the left mass over one full period. That is, a 1:2 ratio means the right mass has one maxima while the left mass has two over a single period.

It was found that much of the rich and complex dynamics that were observed in the 2MM are a ramification of their discrete block geometry, which can cause abrupt non-physiological closure of the vocal folds [36]. This abrupt closure causes a brief spike in aerodynamic loading that has a marked effect on the dynamics. Removing this non-physiological artefact with an *ad hoc* fix causes the dynamics to change significantly, as shown in Figure 1.5b). An aerodynamically smooth version of the 2MM, as shown in Figure 1.4b), condenses the masses to single points creating a continuous, more physiological, trapezoidal geometry. The dynamics of the aerodynamically smooth model are demonstrated by the vibratory regime map of Figure 1.5c). Two-mass models with both rotational

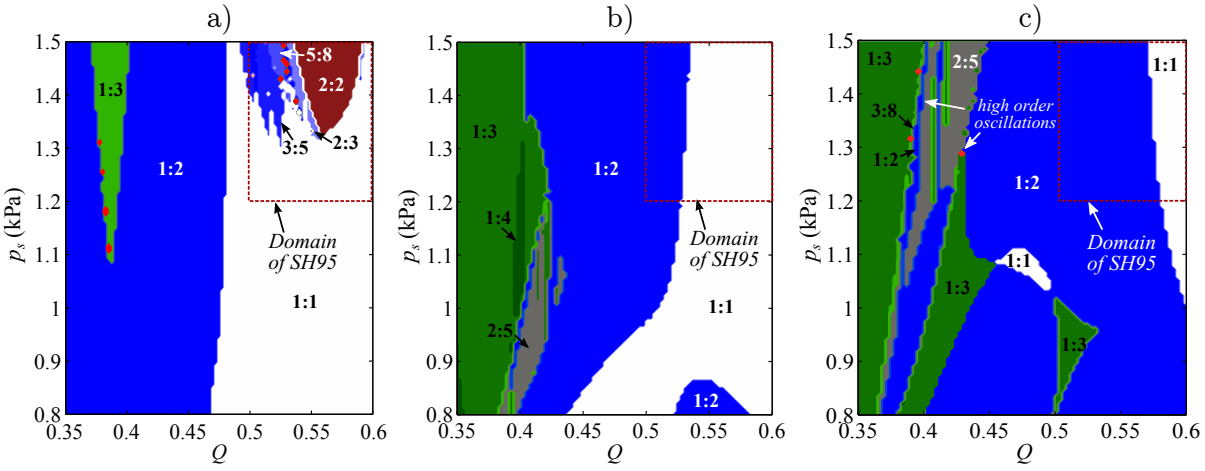

Figure 1.5: Vibratory regime maps of two mass models of the vocal folds for a) the original Steinecke and Herzel 2MM (SH95) [35], b) a modified version with no abrupt closure, and c) an aerodynamically smooth model like the one shown in Figure 1.4b).

and translational degrees of freedom, shown in Figure 1.4d), are also employed [37, 38]. Known as bar-plate models, these models capture the layered structure of the vocal fold tissue while also providing an aerodynamically smooth surface.

By far the biggest limitation of the reduced order model is the non-physical treatment of the aerodynamic loading. A 1-D inviscid flow solution is used in most studies to solve for the time varying aerodynamic loading on the vocal folds. Experimental investigations, as discussed in Section 1.2.1, have shown the flow field through the glottis to be highly complex with many viscous flow behaviours such as flow separation, vortex shedding, transition to turbulence, and asymmetric skewing of the glottal jet [3].

1.2.2.2 Improved flow solutions

More physical flow solutions have been proposed to address the disparity between the observed experimental flow phenomena and the simplified treatment employed in reduced order models. An *ad hoc* correction has been proposed to add separation effects [37], as well as a more physics-based method by solving the momentum integral equations [39,40]. A theoretical flow solver for the intraglottal flow, incorporating the boundary layer development and separation, has been proposed [12]. A Falkner-Skan similarity solution is used to solve the flow over a rotating and translating flat plate, used to represent the

medial surface of the vocal folds. These improved flow solutions, coupled with reduced order tissue models, offer a good tool for broad parameter studies as they attempt to capture the fluid-structure interactions in a computationally inexpensive package.

1.2.2.3 Computational fluid dynamics studies

Computational fluid dynamics (CFD) has been applied, in varying degrees of complexity, to the fluid-structure interactions of speech. CFD has been used with simple reduced order models discussed in Section 1.2.2.1, as well as higher order tissue models. Tao and Jiang [8] use an aerodynamically smoothed version of the Steinecke and Herzel model, similar to Figure 1.4b), coupled to a CFD solution to the Navier-Stokes equations. Initially, the marked changes of dynamics over the original Steinecke and Herzel 2MM were attributed to the inclusion of a viscous flow solution. However, as previously mentioned, the simple switch from discrete block geometry to aerodynamically smooth model geometry elicits considerable changes itself. The CFD model does help to elucidate how the flow field affects vocal fold dynamics and show that even for symmetric tissue properties, flow asymmetries occur [2].

CFD models of the glottal flow have also been paired with more detailed dynamical models of the vocal fold tissue by finite element analysis (FEA). Thomson et al. [5] conducted a FEA model of the coupled fluid-structure problem and compared it to an experimental synthetic self-oscillating model. This provided insight into the energy transfer mechanisms of speech. Recently, direct numerical simulation of a subject specific model of phonation was studied [11]. This used high resolution computed tomography to digitize the anatomy of a specific patient and to model the flow through the glottis. These studies capture the fluid-structure coupling and provide more detailed views of the dynamics. Although, with their intense computational costs, these models are not appropriate for broad parameter studies. Numerical models of fluid flow require validation against representative experiments, which is not consistently found in the speech literature.

1.2.3 Prior work on numerical-experimental facilities

The problem of modelling complex fluid-structure interactions is by no means unique to the field of speech research. Fluid-structure coupling of a variety of bluff bodies in cross flows has been exhaustively investigated (see, for example, [41]). A canonical example of such fluid-structure interaction problems is the fluctuating pressure loading acting on a cylinder in a cross flow. Both driven and free-vibration experimental studies have been

performed to characterize the behaviour of cylinder motion and resulting flow in the wake [42]. Limitations in the suspension system of free-vibrating apparatus motivated Hover et al. [43] to propose a force-feedback coupled numerical-experimental facility. Their facility utilizes a horizontal cylinder mounted on each end with load-cells to measure the force on the cylinder. The cylinder is towed through a tow tank and the measured force is fed into a controller that calculates the dynamic response of a free-vibrating cylinder with specified structural parameters. Based on the calculated response, a servo motor updates the cylinder's position and velocity accordingly. Thus, the force-feedback apparatus is, in effect, in free-vibration with the structural response determined by software and the fluid loading determined by experiment. The system was originally envisioned for modelling undersea cables in currents, and a more generalized and improved version of the system has since been developed [44]. The recent version of the facility has demonstrated excellent agreement with prior experiments. This hybrid approach to fluid-structure experiments allows for studies that would have been difficult or impossible to achieve with traditional methods, such as experiments with arbitrary non-linear restoring springs [45].

Using force-feedback in these experimental facilities presents some limitations. Given that the experimental models are of finite length, end effects will affect the force experienced on the body. The relative contribution to the loading on the model will decrease as the aspect ratio of the model increases but will always remain finite. This is problematic when drawing conclusions on the 2-D dynamics of the cylinder when the fluid loading is in fact a 3-D phenomenon. Another limitation of force-feedback facilities is the inability to resolve the spatial distribution of surface pressures over the body. Only the net force on the body, the integration of all pressures across the surface as well as body forces, is measured. Valuable information of the fluid-structure coupling is gained from knowledge of the pressure loading and its spatial and temporal variation.

1.3 Proposed facility

In reviewing the current state of the art of vocal fold modelling in Section 1.2, some of the limitations of each method are identified. Experimental flow studies offer excellent insight into the flow behaviour, but rigid, pulsatile, and driven experiments all fail to capture the fluid-structure coupling that is vital to speech. Self-oscillating synthetic models prove difficult for accurate measurement and lack the flexibility of easy parameter modification. Numerical models, although capturing the fluid-structure coupling, either employ non-physical simplifying assumptions about the fluid dynamics, or are too computationally expensive for broad parameter studies. Numerical models also require validation against

representative experiments.

A novel modelling approach is proposed that aims to capture the fluid-structure coupling and incorporates the flexibility of numerical tissue models with the physical relevance of experimental flow solutions. A coupled numerical-experimental system, similar to those described in Section 1.2.3, is proposed to study the human vocal folds. In place of force, the pressure distribution across the medial surface is used as an input to the dynamical model. Use of pressure as a control input allows for a true 2-D implementation of the model where only pressures in the mid-plane of the model, far from finite edge effects, are used to calculate loading. PIV measurements in the same plane as the pressure taps can be synchronized with the pressure data to give spatially and temporally resolved data on the intraglottal flow field as well as the surface pressure. Tissue dynamics are solved at each time step by applying the measured pressure loading to one of the reduced order numerical models discussed in Section 1.2.2.1. Modelling the dynamics in software allows for simple changes to parameters, as well as modelling arbitrarily complex tissue mechanical properties.

1.4 Research objectives

The proposed facility is developed with the purpose of addressing the following broad research objectives:

1. quantify the importance of capturing the fluid-structure coupling in models of flow through the glottis
2. provide a representative experiment with which numerical simulations can be validated
3. identify the salient features of the glottal flow to focus future model development.

These broad objectives guide the development of the proposed facility, and dictate design decisions.

Chapter 2

Pseudo Self-Oscillating Pressure Feedback Apparatus

In an effort to overcome the shortcomings of existing modelling architectures outlined in the previous chapter, a combined experimental-numerical approach is pursued. The development of the facility is outlined in this chapter, progressing from a system level design to detailed development.

2.1 Architecture and preliminary Design

A schematic overview of the requisite elements of a coupled numerical-experimental facility for vocal fold studies is shown in Figure 2.1. Sensors draw information from the physical domain as inputs to the controller, and actuators manipulate the physical apparatus in accordance with the outputs of the dynamical model solved on the controller.

Preliminary requirements for each element of the architecture of Figure 2.1 is considered in this section. First, the experimental flow facility is considered at a high level, to determine what the optimal scale and working fluid is, as these drive preliminary actuator and sensor requirements. Controller requirements are primarily driven by the computational requirements of solving the dynamical model and other input, output, and control tasks.

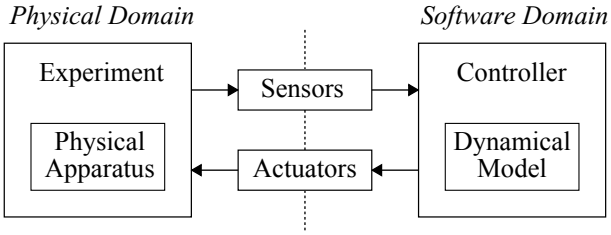

Figure 2.1: Schematic overview of the requisite elements of the coupled numerical-experimental facility.

2.1.1 Fluid flow

The primary objective guiding the design of the flow facility is to achieve a system that produces physically representative flow conditions to garner improved understanding of the fluid dynamics of human speech. To this end, it is paramount that the non-dimensional parameters that govern the flow through the glottis are maintained between the physiological and experimental scales. The three pertinent non-dimensional parameters are the Reynolds, Strouhal, and Euler numbers, defined as

$$Re = \frac{\rho v L}{\mu} \tag{2.1}$$

$$Eu = \frac{\Delta P}{\rho v^2} \tag{2.2}$$

$$St = \frac{f L}{v} \tag{2.3}$$

where ρ is the fluid density, μ is the fluid viscosity, v is the velocity of the flow L is the characteristic length scale, and ΔP is the transglottal pressure drop. The fundamental frequency of oscillation of the vocal folds, f, is the characteristic frequency of oscillation, and the characteristic length scale, L, is set as the nominal glottal gap. These non-dimensional parameters are used to scale between experimental and physiological values, while maintaining equivalent flow physics. By combining equations 2.1, 2.2, and 2.3, the equivalent fundamental frequency and transglottal pressure drop of a representative experimental facility are derived in terms of physiological values and experimental parameters as

$$f_{\text{exp}} = \frac{\rho_{\text{phys}}}{\rho_{\text{exp}}} \frac{\mu_{\text{exp}}}{\mu_{\text{phys}}} \left(\frac{L_{\text{phys}}}{L_{\text{exp}}} \right)^2 f_{\text{phys}} \tag{2.4}$$

$$\Delta P_{\text{exp}} = \frac{\rho_{\text{phys}}}{\rho_{\text{exp}}} \left(\frac{\mu_{\text{exp}}}{\mu_{\text{phys}}} \right)^2 \left(\frac{L_{\text{phys}}}{L_{\text{exp}}} \right)^2 \Delta P_{\text{phys}} \tag{2.5}$$

where the subscripts "exp" and "phys" indicate experimental and physiological values respectively.

Length scales less than 7.5 times larger than physiological scale are deemed too difficult to machine and would not allow enough room for sufficient instrumentation. Models larger than 20 times physiological scale are too big to manufacturer with the available machinery and would add significant cost. Figure 2.2 shows the scaled experimental values of period of oscillation and transglottal pressure drop, plotted over the range of possible scales and for working fluids with viscosities ranging from that of water up to a fluid 15 times as viscous.

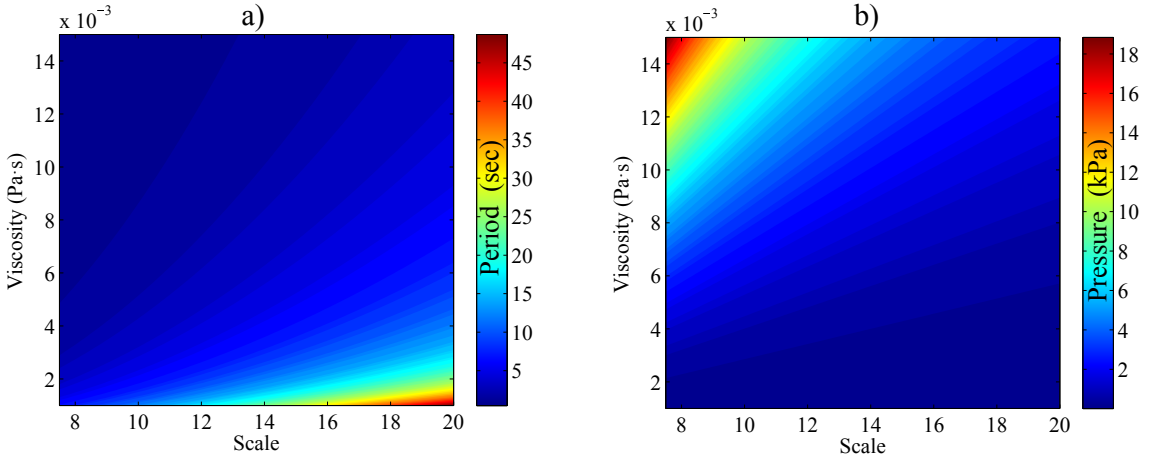

Figure 2.2: Scaled experimental values for a) period of oscillation and b) transglottal pressure drop, as functions of experiment working fluid viscosity and scale compared to physiological size.

To guide the initial selection of possible model scales and working fluids for the facility, initial constraints are imposed on acceptable values of oscillation frequency and transglottal pressure drop. Limitations on oscillation frequency and scale are imposed by actuator

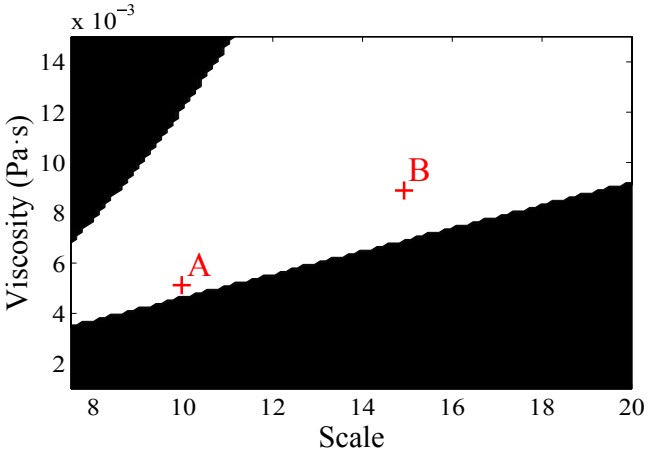

Figure 2.3: Region of fluid viscosity-model scale combinations that satisfy the criteria of $\Delta P \geq 1$ kPa and $T \geq 1$ s. Points A and B indicate the two candidate design points.

specifications, limiting how quickly and over what amplitude the model can oscillate. Limitations on transglottal pressure drop are imposed by pressure transducer specifications, namely the accuracy with which the model surface pressures can be resolved. It is therefore preferable to maximize oscillation period, while also maximizing transglottal pressure drop; this ensures the most flexibility in specifying actuator and pressure transducers.

It is desirable to use inexpensive miniature printed circuit board (PCB) mounted pressure transducers, which allow for a high spatial resolution of pressure sensing with many sensors and more packaging flexibility. To resolve pressure changes through the glottis with the PCB mounted pressure transducers, it is desired to have a transglottal pressure drop greater than $\Delta P = 1$ kPa for preliminary sizing. To mitigate non-inertial effects on the pressure measurements and to relax actuator and control algorithm requirements, a minimum oscillation period of $T = 1$ sec for the experimental apparatus, which is equivalent to 135 Hz physiological, is specified. After applying the two aforementioned constraints to the functions plotted in Figure 2.2, an acceptable set of fluid viscosity and model scale combinations is defined. The set of possible combinations of parameters is demarcated by the white region of Figure 2.3. The two points, A and B, in Figure 2.3 indicate the two possible design points considered. Point A is for a model 10 times larger than physiological scale, using a fluid viscosity of 5×10^{-3} Pa s. This viscosity is selected because it is the viscosity of a 50% by volume concentration of propylene glycol and water at 21°C. The viscosity of an aqueous propylene glycol solution is strongly dependent on temperature as well the mixture fraction of propylene glycol. Figure 2.4 shows the viscosity of different

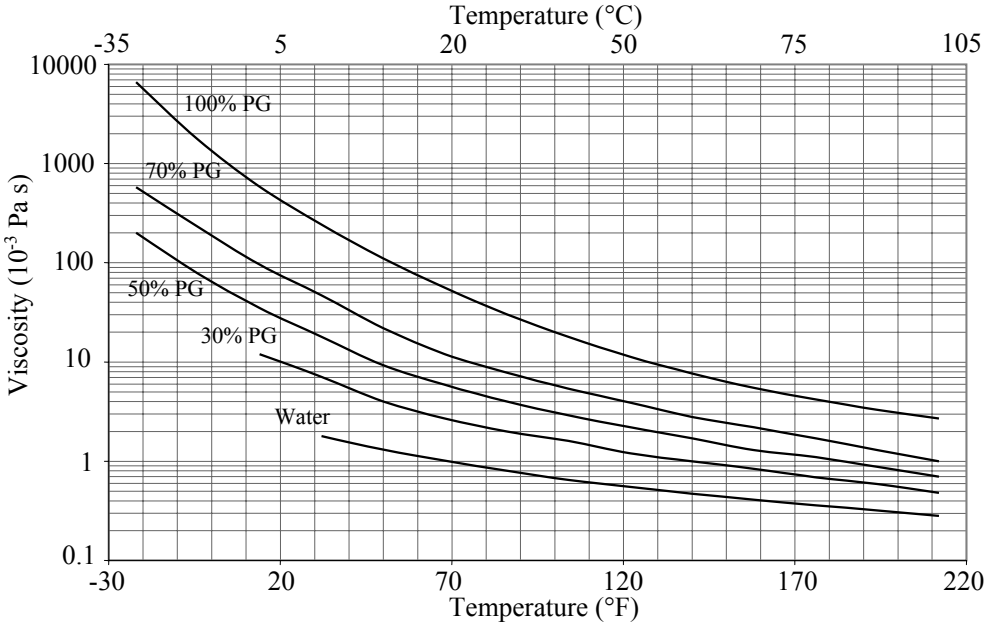

Figure 2.4: Viscosity of different concentration aqueous solutions of propylene glycol as a function of temperature [46].

concentrations of propylene glycol solutions as a function of temperature.

Point B corresponds to a model of 15 times physiological scale, and a viscosity of a 50% aqueous propylene glycol at 15°C, which equals 9×10^{-3} Pa s. Point A yields a transglottal pressure drop that is 77% of physiological scale, and an oscillation period of 2.5 seconds for a physiological frequency of 135 Hz, while point B yields a transglottal pressure drop that is 117% of physiological scale, and an oscillation period of 3.0 seconds. Point B is selected due to the higher pressures and slower motion, and the increased scale allows for more flexible instrumentation packaging. The design viscosity can be achieved with a 50% aqueous glycol solution with moderate chilling.

2.1.2 Controller requirements

In order for the coupled numerical-experimental framework to function correctly, it is paramount that the controller (the software domain) and the experimental apparatus (the physical domain) be as synchronized in time as possible. To this end, a real-time controller with high determinism is essential for proper implementation of the proposed facility. Higher loop rates will increase the systems ability to accurately model the physical

phenomena. At each time step, which must be accurately defined against wall-clock time, the controller must complete the functions outlined schematically in Figure 2.5. Blocks indicate individual functions, whereas the inputs and outputs of each function are indicated in italics between function blocks.

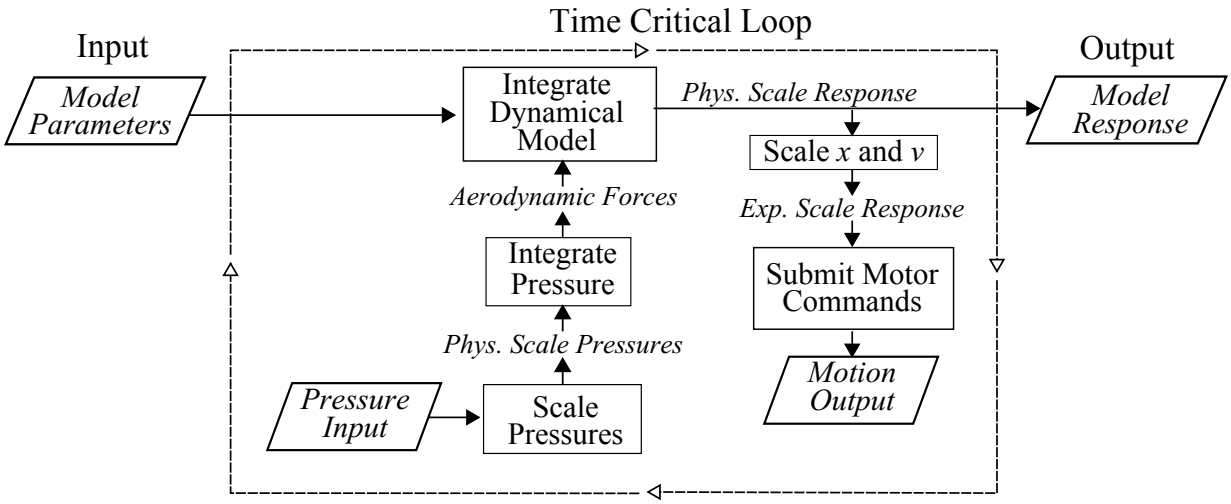

Figure 2.5: Function block schematic of the main controller algorithm.

Model parameters, set prior to simulation execution, dictate the dynamical response of the tissue model, and include information pertaining to the mass, spring, and dampening values of the dynamical model. Along with pressure signals, which need to be sampled at each iteration, these parameters provide the inputs to the dynamical model. As mentioned in Section 2.1.1, the use of small PCB mounted pressure sensors is preferable; these sensors typically do not include analogue-to-digital conversion or any signal conditioning. Thus, it is required that the controller support analogue voltage input.

Information passed between the physical domain and software domain (*i.e.* inputs and outputs of the controller) must be scaled, as per the non-dimensional parameters considered in Section 2.1.1, to move between the applicable physiological or experimental scale. This operation must be conducted to scale the measured experimental pressure values to physiological scale as input to the dynamical model, and to convert the position and velocity values output from the dynamical model to experimental scale. Motion commands are sent to the actuation system at each iteration, to carry-out the experimental-scale motion solved by the dynamical model for the current time step.

2.1.3 Motion requirements

As discussed in Section 1.1, the majority of the vibrational energy of the vocal folds is contained in the first two modes, namely a bulk translation and a rotation of the medial surface. Two mass models use two masses to capture these two degrees of freedom. Thus, two actuators are required for each of the left and right vocal fold models. Any combination of two rotating or translating axes would provide the two requisite degrees of freedom. Two options are considered, two slide inputs, and one slide and one rotational input:

- Two slide inputs benefits from a simple mapping to two-mass models. as the two scaled mass positions correspond directly to the input control rod positions. To provide the requisite degrees of freedom, one control rod must be pin jointed to the vocal fold model, while the second is pin jointed and allowed to slide, as shown in Figure 2.6a).
- Designs featuring one slide input and one rotational input allow for a simpler mechanical design as the actuation system can also provide the structure to support the vocal fold model without additional bearings, hinges, or slides within the tunnel as shown in Figure 2.6b).

To minimize complexity, the actuation system that supports the vocal fold models from a single axle that can rotate and translate, as shown in Figure 2.6b), is selected. Preliminary motion requirements that are used to guide actuator system design are primarily derived from analysing the response of reduced order numerical models for a variety of model parameters. Given that the reduced order models of the vocal folds use simplified flow solvers, it is expected that the aerodynamic forces, and therefore the dynamic response, observed in the numerical-experimental facility will vary from that of reduced order models. In spite of these differences, the inviscid flow models give an order of magnitude estimate of the aerodynamic forces for given input parameters. Furthermore, higher fidelity CFD fluid models coupled to reduced order tissue models demonstrate aerodynamic forces of comparable order to those obtained in inviscid flow solutions [8].

The two-mass model of [35], with the corrected contact stresses of Sommer et al. [47], and aerodynamic smoothing as specified by Sommer et al. [36], is used to assess preliminary estimates of motion requirements. A subglottal pressure of approximately 15 cmH_2O is used, as this is considered to be at the maximum of the range of human phonation. The physiological scale output of the simulation, as well as experimentally scaled values, are given in Figure 2.7. Experimental scaling is calculated using the parameters identified in Section 2.1.1, of $\mu = 5 \times 10^{-3}$ Pa s and 15 times physiological length scale. Physiological

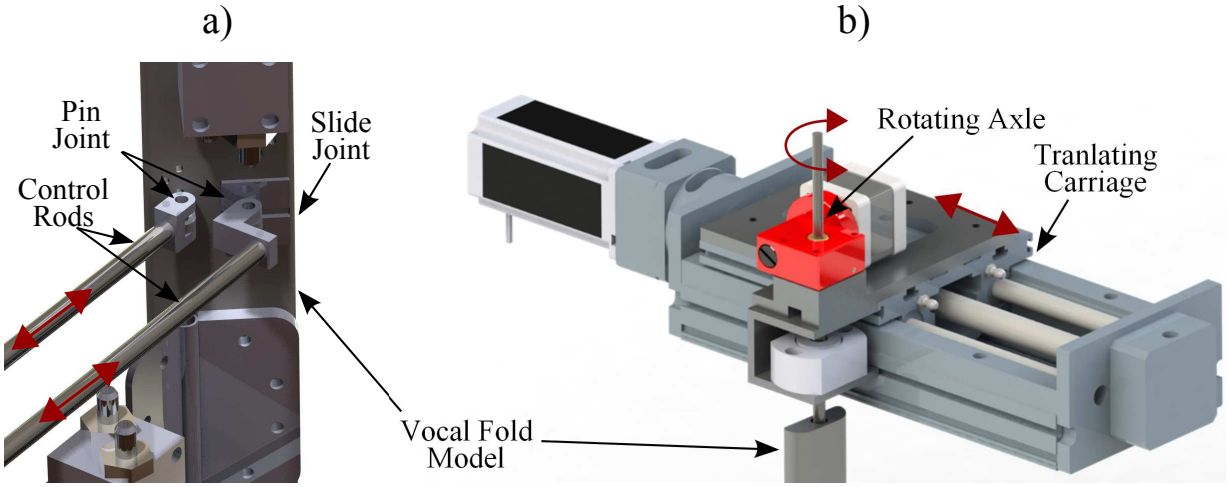

Figure 2.6: Two possible designs to acheive two degree of freedom motion of a vocal fold model; a) two slide inputs and b) one slide and one rotational input.

scale simulations yield maximum amplitudes of oscillation of approximately 1 mm for the inferior mass, with the system oscillating at a fundamental frequency of 130 Hz. For the experimental scale and working fluid selected in Section 2.1.1, this corresponds to a maximum amplitude of oscillation of 15 mm at a frequency of 0.32 Hz. To account for differences in the dynamics caused by experimental fluid loading, and to provide a margin for error, the translating axes of the actuation system are designed to specifications twice that suggested by the simulations. This equates to a system capable of a max linear speed of 70 mm/s, with a range of motion of at least 60 mm.

The same simulation results are used to form initial requirements for the rotational axes of motion. The angle formed by the difference between the inferior and superior masses of the 2MM gives a rough estimate of the range of rotational motion the experimental vocal fold models will undergo. A motion system capable of going from $-30°$ to $30°$ at a frequency of 0.32 Hz is determined based on the simulation results. With a factor of safety of 2, this equates to a max rotational speed of 23 RPM, and a range of motion $-60°$ to $60°$.

Given that the vocal fold models will not be of considerable mass, and that the maximum acceleration of the model is predicted by the simulations to be less than 0.1 m/s^2, the dynamic loads will be very low. Thus, the limiting factor for specifying the force capabilities of a motion system is resisting the pressure loading of the fluid on the vocal fold model surface. At the selected model scale and fluid properties, the maximum transglottal

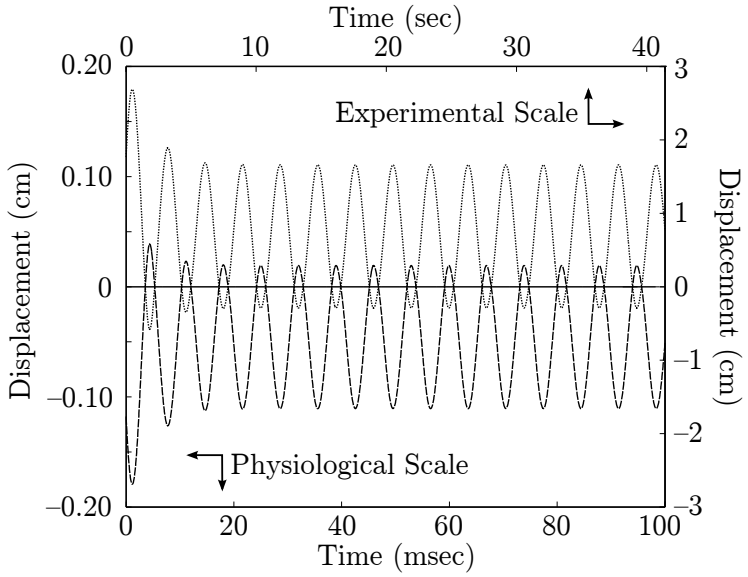

Figure 2.7: Comparison of physiological and experimentally scaled simulation results of the motion of the left ($\cdots$) and right (- - -) inferior mass. The model is an aerodynamically smooth SH95 model, with $P_s = 1.5$ kPa. Note the use of 'msec' for physiological time scale, and 'sec' for experimental.

pressure drop is 18 cmH_2O. For a closed glottis, the integrated fluid loading against the leading face of each vocal fold model is 33.9 N in the streamwise direction and 28.4 N in the cross flow direction.

2.2 Detailed design

With the initial requirements for the motion system, computer, and flow experiment established, the detailed design of the specific embodiments are presented in this section.

2.2.1 Vocal fold geometry

The M5 model geometry of Scherer et al. [22] is used as a basis for the geometry of the physical vocal fold models. This geometry has been used extensively in static [22, 25, 48], self oscillating synthetic [5, 30], and driven model [27] studies, and thus allows for direct comparison to prior work. Comparison of the model in static and driven configurations

can be used as a benchmark of the present work against prior studies, and the effect of capturing the fluid-structure coupling in the self-oscillating run mode can be more easily isolated.

2.2.1.1 Rigid vocal fold assembly

The M5 geometry, shown in Figure 2.8, is defined for a given glottal angle θ by a series of equations presented in [22]. The radius of the leading edge r_1 is constant for all angles, while the radius of the exit of the glottis r_2 varies as a function of glottal angle.

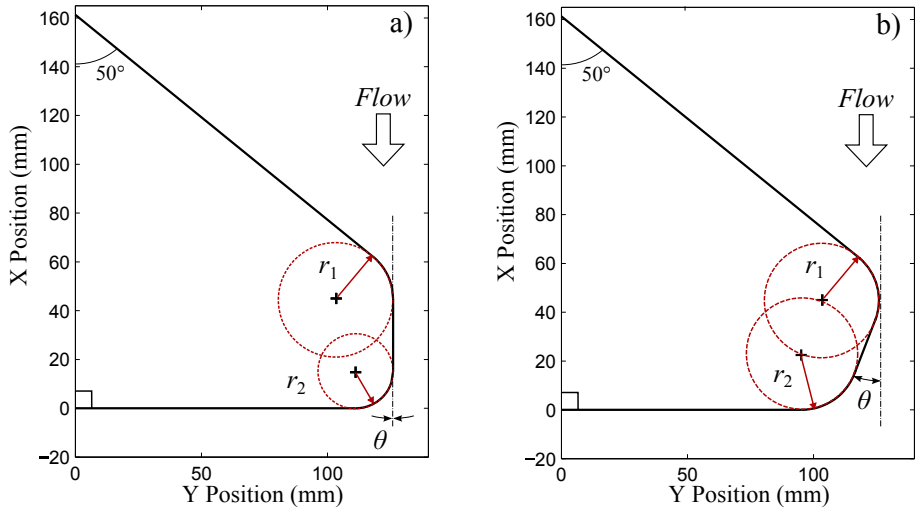

Figure 2.8: M5 model geometry of a left vocal fold model at the experimental scale for a half glottal angle of a) $\theta = 0°$ and b) $\theta = -20°$

The geometry of the M5 model for $\theta = 0°$ is selected. Although exit radius varies with glottal angle, the exit radius for $\theta = 0°$ is the average between the divergent and convergent values. The M5 geometry for $\theta = 0°$ can be described by two circles and 3 lines forming tangents to the circles. Inlet and outlet surfaces of the glottal duct are formed by lines extended from the tunnel wall to intersect the leading and exit radii at a tangent point, as shown in Figure 2.8. This geometry can be implemented in practice with a rigid medial surface, that can be translated and rotated, with flexible sheets extending to the tunnel walls to form the continuous surface of the vocal fold model.

The rigid part of the vocal fold is shown in Figure 2.9a). It consists of a aluminium plate that forms the medial surface and two aluminium tubes halved to form the inlet and exit radii – this forms an extrusion of the M5 geometry that is 150mm in length. The plate

and tubes are mounted to a series of aluminum parts formed on a CNC milling machine such that the plate and tubes form a smooth continuous surface. The assembly is mounted to a shaft that connects to the actuation system to manipulate the position of the vocal fold model.

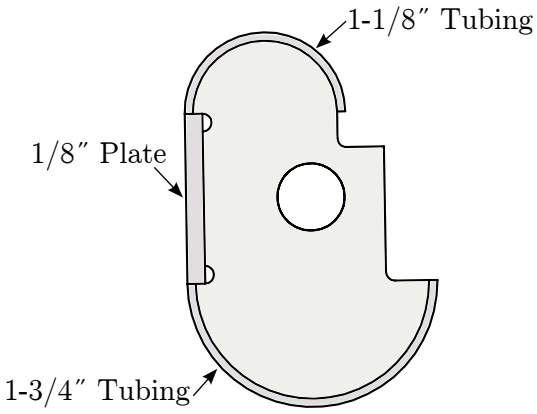

Figure 2.9: Rigid assembly that forms the vocal fold geometry.

2.2.1.2 Continuous surface of vocal fold geometry

A continuous surface must be present to form a boundary for the fluid flow as the vocal fold models rotate and translate. To this end, two plastic sheets are fixed to the ridged vocal fold model assembly, as shown in Figure 2.10a). One sheet attaches to the leading edge of the vocal fold and the other to the trailing edge. The sheets are kept in tension throughout the vocal fold model range of motion with a set of extension springs. Determining the stiffness and lengths of the springs is non-trivial: if the tension is too low the vocal fold geometry will not be predictable and if the tension is too high it will impede the motion of the vocal fold model. The limiting cases that drive the spring stiffness selection are the maximum midpoint deflection when the glottis is open, with no spring pretension, and the maximum tension force when the glottis is closed, with maximum spring pretension.

A simplified model is pursued to optimize the spring stiffness and geometry. It is assumed that the sheet does not deform and all deformation comes from the extension of the spring, as shown in Figure 2.10b). The system is assumed to be planar (*i.e.* no variation along the width of the sheet), so it is modelled as a string with the pressure loading condensed to a point load F acting at the midpoint of the string. The string is

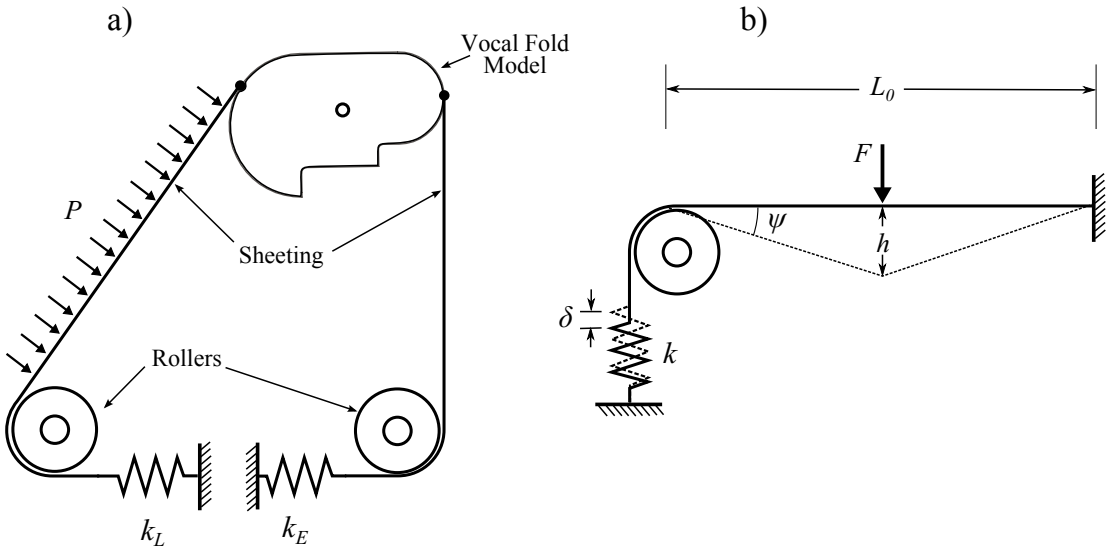

Figure 2.10: Membrane tensioning system. a) Schematic overview of the vocal fold membrane kept in tension with springs as the vocal fold model translates and rotates, and b) the simplified problem for analysis showing pertinent quantities.

initially of length L_0, the midpoint deflection of the sheet is h, the spring stiffness is k, and the spring deformation is δ.

A force balance at the middle of the string (where the load is applied) gives

$$F = 2F_{\mathrm{t}} \sin(\psi) \tag{2.6}$$

where F is the applied load, F_{t} is the string tension, and ψ is the deflection angle as shown in Figure 2.10b). The length of the sheet before loading is L_0 and after loading is L' where $L' = L_0 + \delta$, the angle ψ is found as

$$\psi = \arccos \frac{L_0}{L'} = \arccos \frac{L_0}{L_0 + \delta} \tag{2.7}$$

Tension must be the same throughout the sheet, therefore the force on the spring will also be F_{t}. Combining Equations 2.6 and 2.7 with Hooke's law yields

$$F = 2k\delta \sqrt{1 - \left(\frac{L_0}{L_0 + \delta} \right)^2} \tag{2.8}$$

This relates the applied load F and the deformation of the spring δ for a given spring stiffness and initial length. Deflection h is related to the spring deformation by Pathagorean

theorem as

$$h = \frac{1}{2}\sqrt{(L_0 + \delta)^2 - (L_0 + \delta_{pt})^2} \tag{2.9}$$

With equations 2.8 and 2.9 the deflection h can be estimated for an applied load F. Figure 2.11a) plots deflection as a function of applied load for springs ranging in stiffness from $k = 2.5$ $\frac{\text{N}}{\text{cm}}$ to $k = 100$ $\frac{\text{N}}{\text{cm}}$ for an initial length $L_0 = 140$ mm under no pretension. This configuration corresponds to the case that the vocal fold model is positioned at the closest distance to the tunnel wall (a wide open glottis).

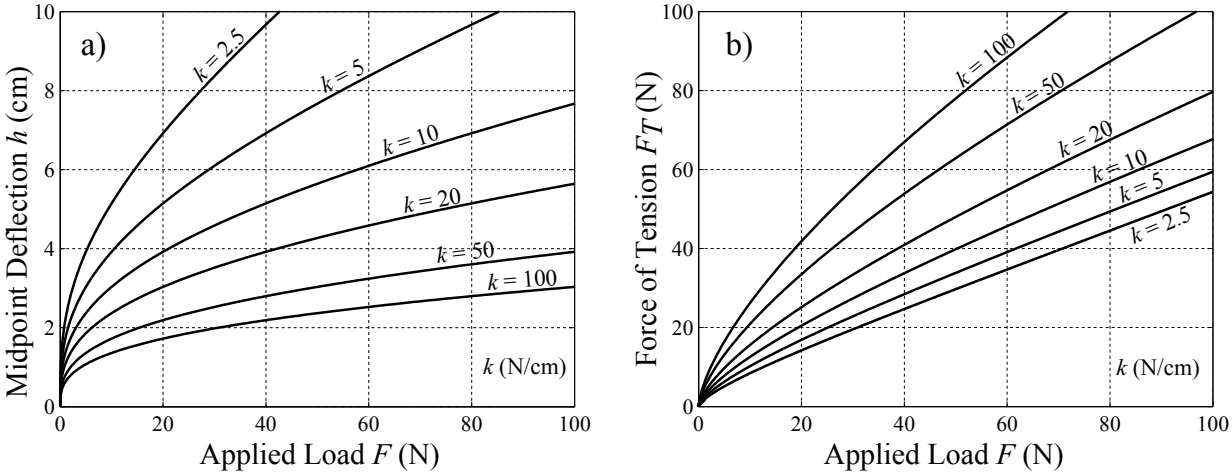

Figure 2.11: Design charts for spring selection for an open glottis (no pretension) with $L_0 = 140$ mm. a) Midpoint deflection h as a function of applied load F and, b) tension force F_T in the sheet as a function of applied load F.

To select the appropriate spring stiffness, the method is as follows: the estimated loading on the sheet upstream of the glottis is estimated to be $F \approx 40$ N as found in Section 2.1.3. A maximum permissible midpoint deflection is selected to be 3 cm, which will occur when the vocal fold models are closest to the walls and the pretension in the spring is at a minimum. A spring stiffness that will meet the deflection limit under the given applied load is chosen from Figure 2.11a). For the selected spring stiffness the force of tension in the sheet is found with 2.11b), which is fed into the actuator design requirements as the load acting on the vocal fold models. The force of tension acting on the vocal fold model should be less than 50 N, though to minimize the force requirements for the actuators the minimum possible tension force is preferred. A spring of stiffness $k = 50$ $\frac{\text{N}}{\text{cm}}$ or higher meets the permissible deflection limit under the 40 N applied load, which leads to a tension force of $F_T = 54$ N.

Translating the vocal fold model 23 mm to the midline causes the spring to deform approximately 30 mm, thus pretensioning the spring; this configuration, a closed glottis, corresponds to the highest pretension in the springs. Figure 2.12a) relates the midpoint deflection to applied load for a sheet pretensioned such that $\delta_{pt} = 30$ mm, making the initial length $L_{0,2} = L_0 + \delta_{pt} = 170$ mm.

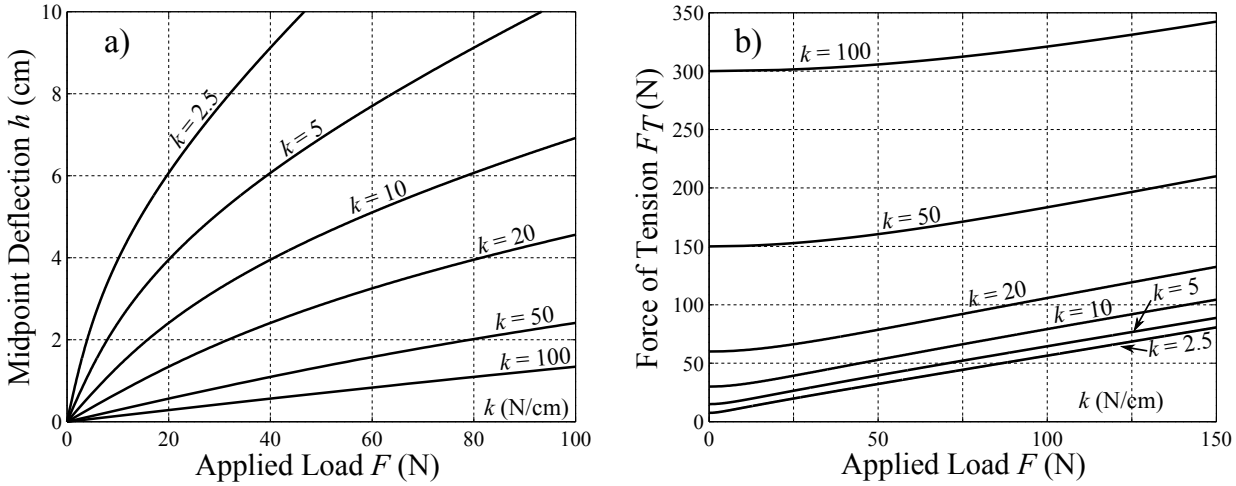

Figure 2.12: Design charts for spring selection for closed glottis (maximum pretension) with $L_{0,2} = 170$ mm. a) Midpoint deflection h as a function of applied load F and, b) tension force F_T in the sheet as a function of applied load F.

Using the spring stiffness selected from the no pretension case, $k = 50 \frac{\text{N}}{\text{cm}}$ the maximum force of tension is found with Figure 2.12b), to be $F_T = 150$ N with no applied load and $F_T = 157$ N under the 40 N load. These tension forces are well above the established limit of $F_T < 50$ N. The high tension forces required to mitigate sheet deflection render the system proposed in Figure 2.10 impractical. A system with a central support, shown schematically in Figure 2.13 is analysed in pursuit of reducing the deflection and tension requirements.

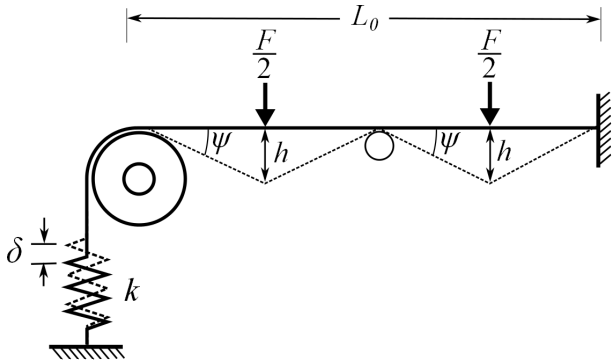

Figure 2.13: Simplified model for a centrally-supported sheet tensioned with extension springs.

Following the same method as the unsupported case, the midpoint deflection h for a given applied load F is solved for springs of various stiffness and given as Figure 2.14a).

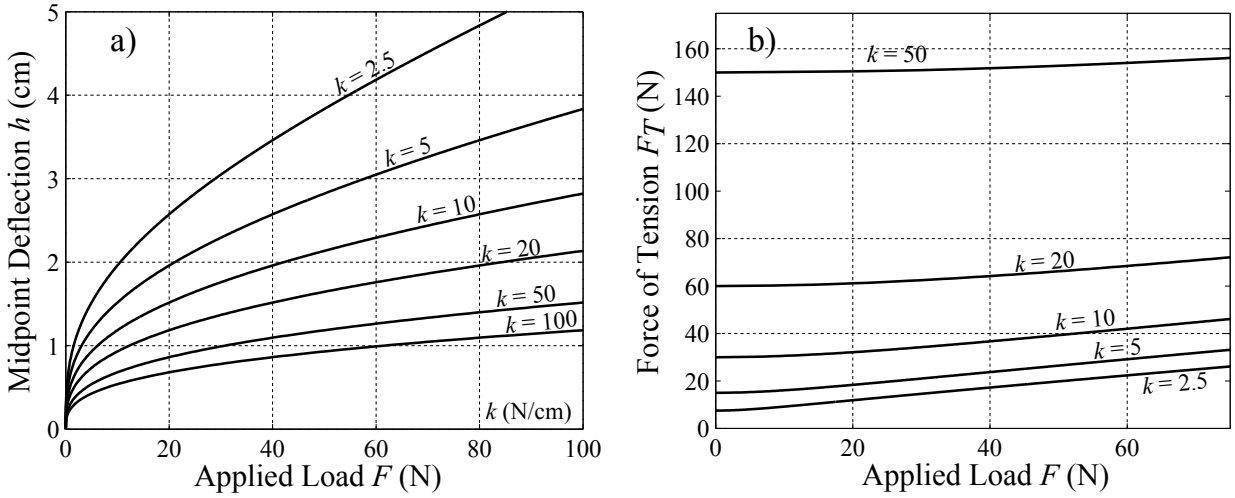

Figure 2.14: Design charts for spring selection for a centrally supported tensioned sheet. a) Midpoint deflection h as a function of applied load F for an open glottis (no pretension) with a central support, and b) tension force F_T in sheet as a function of applied load F.

The central support reduces the spring stiffness required to maintain the $h < 3$ cm design constraint, and can be satisfied by a spring of stiffness $k = 5$ $\frac{\text{N}}{\text{cm}}$. Figure 2.14b) gives the force of tension for a closed glottis with $\delta_{pt} = 30$ mm as a function of applied load

for the centrally supported design. Under the design load of $F = 40$ N a force of tension of $F_T = 23.8$ N is predicted. The addition of the central support reduces the maximum force of tension by almost an order of magnitude, making it well within the prescribed limits.

Based on the analysis conducted herein, an extension spring tensioned vocal fold cover sheet is feasible provided an additional central support is added to the structure. A maximum force of tension of $F_T \approx 25$ N is prescribed as an input to designing the actuators and support system – noting that each vocal fold will be loaded by both the upstream and downstream tensioned sheets.

The embodiment of the mechanism designed in the previous analysis is shown in Figure 2.15. Transparent sheets of cellulose acetate are used to form the continuous surface from the vocal fold model to the springs. The acetate sheets are selected as they are flexible while still offering some structure.

Three springs, each of stiffness $k_i = 2\ \frac{\text{N}}{\text{cm}}$, are arranged in parallel and attached to the upstream section of sheet, giving an effective stiffness of $k_{\text{eff}} = 6\ \frac{\text{N}}{\text{cm}}$. The springs have an unstretched length of 35 mm and are capable of a deflection $\delta_{\text{max}} = 35$ mm – which meets the force and range of motion specifications of the above analysis. The downstream sheet is tensioned with two springs, each of stiffness $k_i = 3.2\ \frac{\text{N}}{\text{cm}}$ giving an effective stiffness $k_{\text{eff}} = 6.2\ \frac{\text{N}}{\text{cm}}$ and a max deflection of $\delta_{\text{max}} = 21.2$ mm, slightly below the target maximum range of motion of 23 mm.

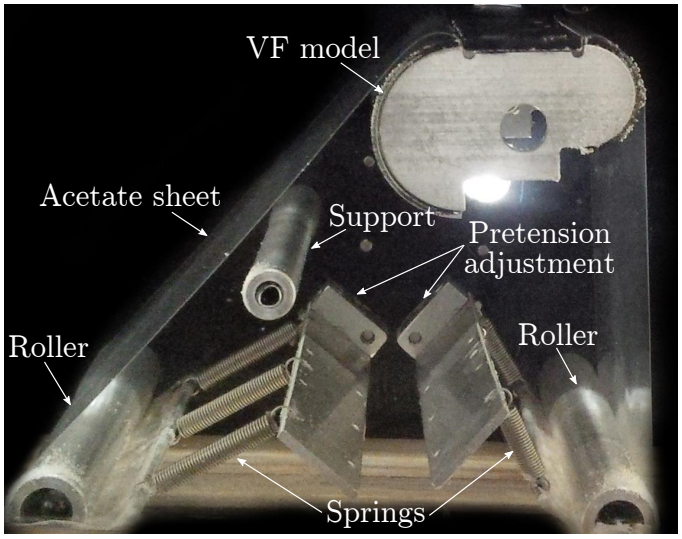

Figure 2.15: As built vocal fold sheet system, showing a) VIEW and b) view from below as installed in test section.

The distance between the rollers and the fixed end of the springs can be varied by rotating the plate that the springs connect to. The 25 mm wide plate, pivoted off center, allows for the distance from the upstream roller to be varied from 40 mm to 78 mm, allowing for fine adjustment of the spring pretension.

2.2.2 Motion mechanism

To provide the requisite degrees of freedom, two motors are required for both the left and right vocal fold models to actuate the translational and rotational motion of the models. The motion system must also provide the structural support of the vocal fold models in the test tunnel.

2.2.2.1 Translational axis actuator

The analysis completed in Section 2.1.3 specifies a max linear speed of 70 mm/s with a maximum range of motion of 60 mm; these values provide a starting point for actuator selection. For the selected actuation strategy, with one translational and one rotational degree of freedom for each vocal fold model, the rotational actuation system will have to travel on the end effector of the translational system. The rotational system will rotate a shaft to which the vocal folds are mounted and the translational system will slide the entire rotational system back and forth, as shown in Figure 2.6b). This means the translational system must be capable of supporting the static and dynamic loads of the entire rotational system, as well as the vocal fold assembly. This includes the fluctuating pressure loading that the fluid applies to the vocal fold models, as well as the tension force applied from the tensioned vocal fold sheet covers. It is therefore important that the slide be capable of smooth and repeatable motion under varying forces and moments.

Linear motion slide systems, which incorporate an actuating screw and linear bearings into one package, are capable of resisting very high loads. Ball screw units provide greater efficiency and lower backlash over acme screw designs. Ball bearing linear guides can withstand higher loads than bushing designs and provide smoother motion with less stiction, which could introduce non-linearities. A linear motion slide system with a ballscrew drive and ball bearing guides is selected as the best option. Thomson Linear's 2RB series is selected as it offers high rigidity and repeatability of ± 0.005 mm and can be configured to any stroke length from 0 to 1951 mm.

For lead screws (both acme and ball type screws) the linear speed and force at the nut are

$$\dot{s} = \frac{N}{60} l \tag{2.10}$$

$$F = \frac{2\pi\tau\eta}{l} \tag{2.11}$$

where $\dot{s}$ is the linear speed of the slide, N is the speed of the motor rotation in revolutions per minute, l is the screw lead, τ is the input torque, and η is the efficiency of the screw. These equations allow the slide performance to be evaluated in terms of the input motor specifications.

Given the relatively low speed requirements, both stepper motors and brushless DC servo motors are considered to drive the slide. Stepper motors offer 3 advantages over brushless DC motors in this application: high holding torque, simple control, and low cost. The primary limitation of stepper motors is their precipitous torque falloff at high speeds. It is therefore important that the motor and slide combination is considered carefully to ensure the speed and force requirements can be satisfied. The Kollmorgen T22 NEMA 23 stepper motor with 280 oz-in holding torque is selected because of its relatively high torque, availability, low cost, and well integrated control options. The torque-speed curves for the T22 stepper motor are given in Figure 2.16a) showing both 24 and 36 volt DC excitation.

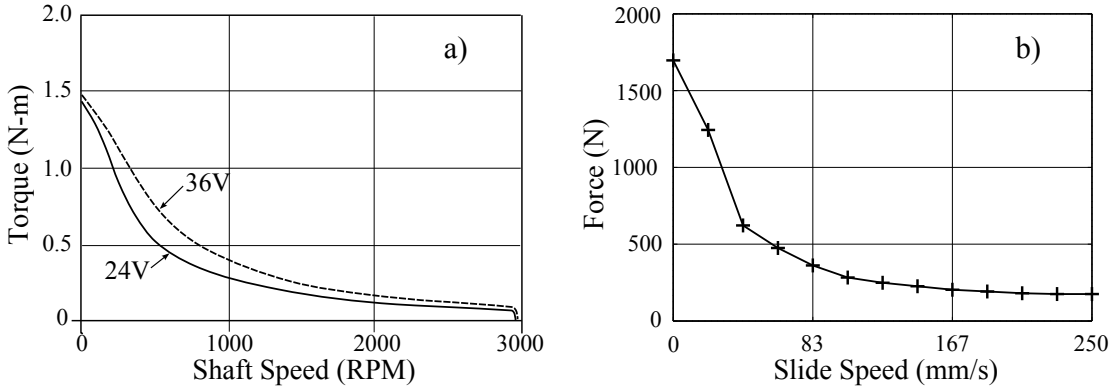

Figure 2.16: Slide performance based on motor torque. a) Speed-torque curve for NEMA 23 stepper motor (Kollmorgen T22xxLC), and b) approximate speed-force curve for a Thomson Linear 2RB12 ballscrew coupled to the stepper motor.

With Equations 2.10 and 2.11, the performance of a 2RB12 linear motion slide driven by the stepper motor can be estimated. The linear force available in the direction of

motion (without causing missed steps) is plotted against slide speed for a 2RB12G slide with a screw lead $l = 5\ \frac{\text{mm}}{\text{rev}}$ and efficiency $\eta = 0.9$ for a T22 stepper motor with 24VDC excitation. Recalling the speed requirements from Section 2.1.3, the maximum design speed for the slide is 70 $\frac{\text{mm}}{\text{s}}$. At this speed, the stepper motor and slide combination can provide approximately 450 N of force, which is well above both the static and dynamic translational load requirements.

2.2.2.2 Rotational axis actuator

The analysis completed in Section 2.1.3 specifies a maximum rotational speed of 23 RPM. The speed range of small stepper motors is 0 to 3000 RPM but the available torque, as shown in Figure 2.17a), is quite low. A reduction gear can be used to reduce the speed and increase the available torque. An Ondrives US Corporation gearbox provides a worm wheel reduction gear with a standard NEMA 17 motor mount, shown in Figure 2.17b), such that the motor can be attached directly to the gearbox with no additional support or mounting hardware. The gearboxes are available in a range of reduction ratios from 10:1 to 120:1.

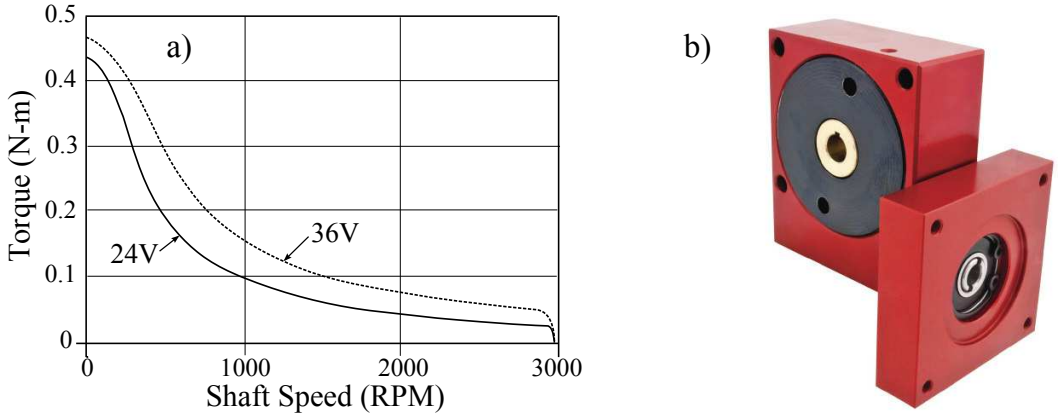

Figure 2.17: Rotational axis speed and torque. a) Torque-speed curve for Kollmorgen CTP12EL NEMA 17 stepper motor, and b) the Ondrives 10:1 reduction gearbox with NEMA 17 direct face mount.

Noting the stepper motor's rapid torque fall-off with increasing speed, a high reduction ratio will have diminishing returns on torque; especially when considering the decreased efficiency of high reduction ratio worm wheel gears. For a 10:1 reduction ratio gearbox, the specified rotation speed is obtained with a motor speed range of 0 and 230 RPM. The

10:1 Ondrives gearbox has an efficiency of approximately 86%, which leads to an available output torque at full speed of 2.6 N m with the stepper motor under 24 V excitation. For this configuration, the torque specifications are four times that required to rotate the vocal fold model if the tensioned sheet were attached only to one side, representing a worst case torque loading scenario. The speed specifications are an order of magnitude greater than required but, given the poor high speed performance of stepper motors, this margin will be significantly smaller in practice.

2.2.2.3 Motion system integration and assembly

The components specified in Sections 2.2.2.1 and 2.2.2.2 form the basis for the motion system. The rigid frame of each vocal fold model is mounted on a shaft that the rotational actuation system rotates. The entire rotational system is mounted to the slide of the translating motion stage such that the shaft can be independently translated and rotated.

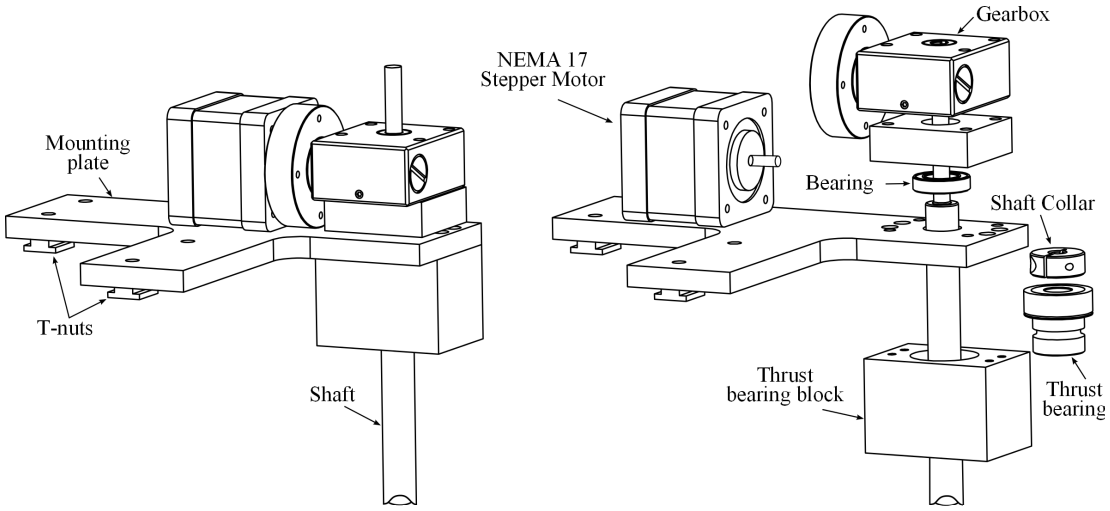

Figure 2.18: Components of the rotational actuation system in assembled (left) and exploded (right) views.

The rotational assembly, that mounts to the stage, is shown in Figure 2.18; no fasteners are included in the diagrams. To support the static and dynamic loads acting on the vocal fold models and to provide smooth and repeatable motion, the shaft is supported by two radial bearings as well as one thrust bearing. A shaft collar clamped to the shaft provides a bearing surface for transferring thrust loading from the shaft. Bearing blocks transfer all shaft loads directly to the mounting plate, which is machined from a single piece of

aluminium plate. The motor face mounts directly to the gear box input flange. The shaft has a clearance fit within the gearbox such that any radial deflection is not transferred to the gears, while drive torque is transferred by means of the shaft key. The mounting plate is bolted to the T-nut slots of the translational carriage such that the whole system moves. Left and right actuator systems are identical and are mounted rotated 180° from one another such that the shafts share a common translational axis, as shown in Figure 2.19.

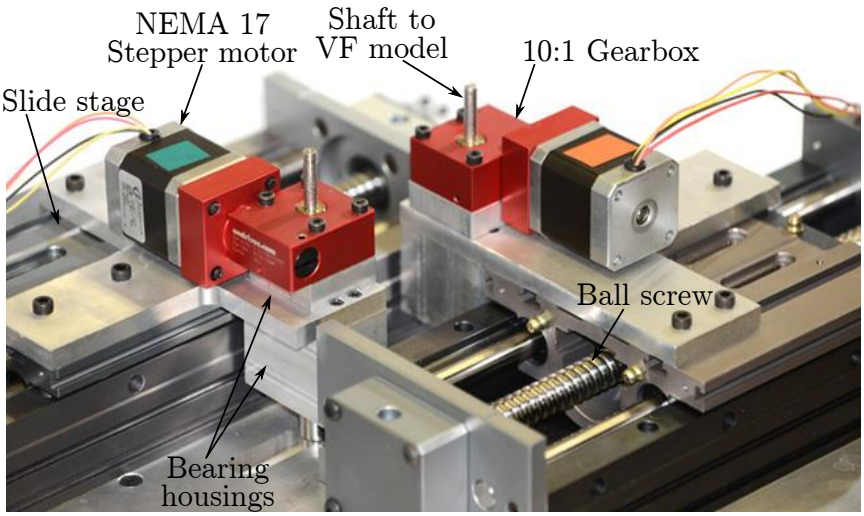

Figure 2.19: Photograph showing the assembled motion system with the rotational axis mounted on the translating slide.

2.2.3 Pressurization sealing

In contrast to many other flow phenomena of engineering interest, such as external flow around bluff bodies and airfoils, the flow through the glottis is an internal duct flow. Pressure variations in the streamwise direction are the primary quantity of interest. Consequently, the apparatus and flow tunnel must be sealed to prevent the pressure normalizing to the atmospheric pressure of the ambient. Significant leakage through the shaft penetration would result in de-pressurization and a loss of conservation of mass between the inlet and outlet of the glottal model.

Sealing the shaft penetrations is complicated by the fact that the shafts translate in addition to rotating. O-rings and radial shaft seals are ubiquitous in sealing rotating and translating shafts in engineering applications (*e.g.* propeller shafts, crankshafts, pistons,

and hydraulic rams). These sealing methods, are however, only effective for rotation and translation that is coaxial with the shaft. Translation in the plane normal to the axis of the shaft presents a greater challenge to seal adequately. This is further exacerbated by the fact that the left and right shafts share a coincident path of translation, to enable the left and right vocal fold models to rotate with mirrored symmetry (see Figure 2.24).

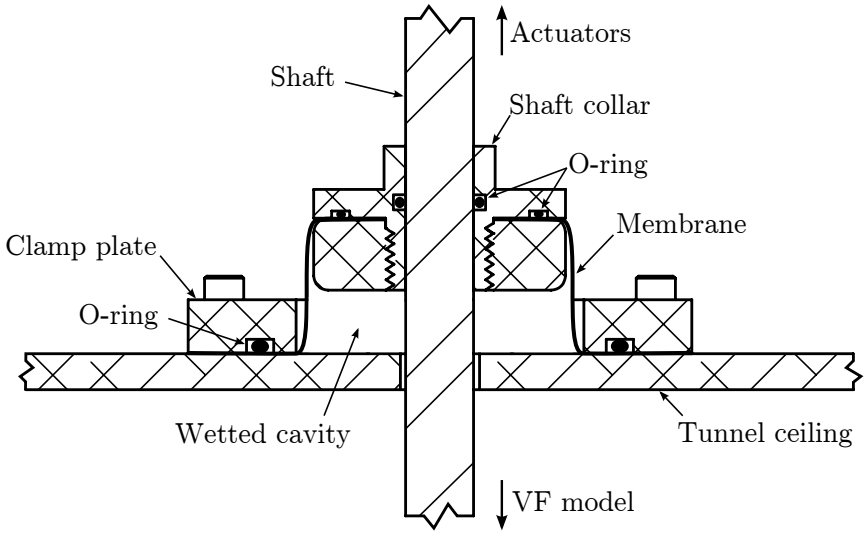

Figure 2.20: Shaft seal system. A shaft collar and membrane allow the shaft to rotate and translate as the vocal fold models are actuated.

Several shaft seal systems are considered and tested; the most effective of which utilizes a shaft collar to effectively decompose the shaft motion into its two constitutive components of rotation and translation, such that they can be treated separately as shown in Figure 2.20. An o-ring seated in the shaft collar seals against the shaft allowing it to rotate independent of the collar. A membrane stretches between the two shaft collars and to the ceiling of the tunnel. A clamp plate seals the membrane to the tunnel ceiling, and two discs thread onto the shaft collars to seal the membrane to the collar with static o-ring seals. Extra material between the two collars and to the clamp plate, in addition to the pliability of the membrane material, affords movement of the shaft relative to the clamp plate without tearing the membrane.

2.2.4 Surface pressure measurement

Accurate measurement of the pressure along the vocal fold model surface is important as it is the link between the fluid and structural dynamics. The pressure along the surface of the rigid vocal fold model, analogous to the medial surface of the vocal folds, will vary both spatially and temporally. Measuring the pressure along the surface is made difficult by the fact that the vocal fold models move, and even more so since the motion is not of constant velocity. Two methods are considered for measuring the pressure distribution across the moving surface: one, plumbing flexible tubes from the pressure taps to stationary transducers; and two, attaching transducers directly to the moving surface. Option one has the advantage of being able to keep the pressure transducers dry and out of the working fluid as well as far greater flexibility in packaging and transducer selection. The shortcoming of this method is that as the surface moves it will change the shape of the flexible tubes, thus inducing a pressure change within the tube. Conversely, with option two, mounting the transducers directly to the moving surface mitigates the issue of running flexible tubing, though this configuration presents its own set of issues. As the surface rotates and translates with changing velocity, the transducers experience varying accelerations. This presents the possibility of causing deflection of the transducer diaphragm as a result of the non-inertial reference frame. Moreover, mounting directly on the vocal fold model presents engineering constraints of packaging the transducers into the small space and ensuring the electronics are capable of correct operation submerged in the aqueous working fluid. Although both configurations present challenges, option two is selected since the amount of 'phantom pressure' caused by diaphragm deflection is estimated to be very small given the low acceleration rates calculated from the preliminary studies completed in Section 2.1.3.

Given that the pressure transducers are to be mounted directly to the vocal fold model, the use of small sensors is necessary to be able to meet the small volume available for mounting on the back of the vocal folds. The use of PCB mounted miniature pressure transducers also offers the advantage of an order of magnitude cost reduction as compared to larger, albeit more precise, laboratory pressure transducers. Omega PX-40 PCB mount pressure sensors, shown in Figure 2.2.4a), are selected as they are one of the few stock PCB sensors available that are compatible with liquid working fluids. The PX-40 is configured to have a measurement range ± 6.67 kPa (± 50 mmHg) and provides signal conditioning and temperature compensation. Power is supplied with 5V DC input and the sensors give an analog voltage output ranging between 1V and 4V.

The transducer diaphragm is compatible with wetting liquids but the electronics and atmospheric vent require dry air; thus the sensors are mounted within a waterproof container. The container, shown in Figure 2.2.4b), has waterproof perforations for the pressure

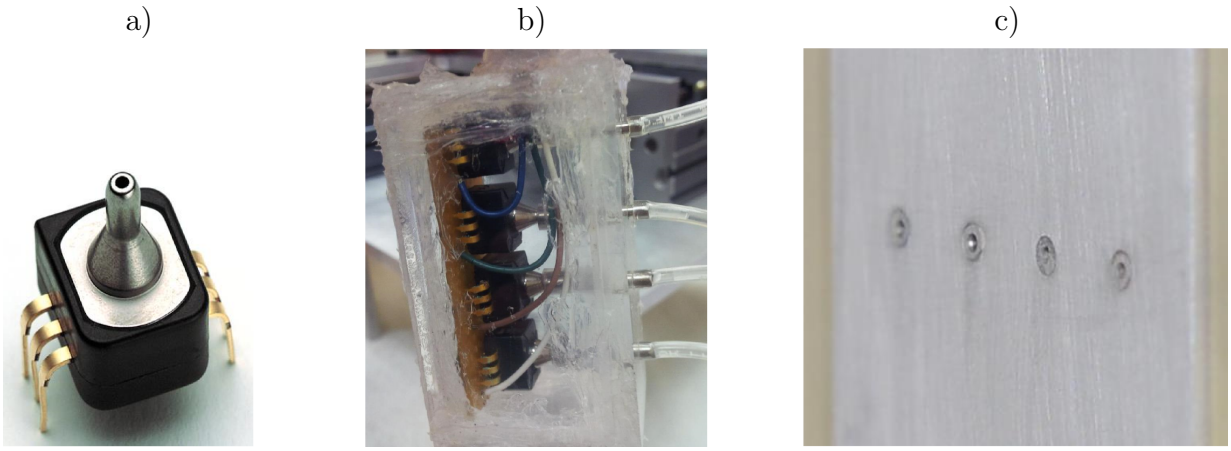

Figure 2.21: Surface pressure measurement system. a) a PX-40 pressure sensor, b) four PX-40 sensors mounted to a circuit board and enclosed in water proof case, and c) pressure taps in the surface of the aluminium rigid vocal fold model plate.

hoses to attach and for the power and signal cables to be routed outside of the tunnel. Mounted directly to the back of the vocal fold model, the sensor enclosure moves with model. Tubes are routed from the sensor enclosure to four stainless steel pressure taps press fit into the rigid model assembly. Each pressure tap is flush mounted to the surface of the aluminium plate to minimize flow disturbance, shown in Figure 2.2.4c). The pressure tap holes are diameter $d_t = 0.5$ mm, and are spaced a distance $l_t = 6$ mm centre-to-centre, giving a ratio of $\frac{l_t}{d_t} = 12$.

Pressure sensors are calibrated using a simple water head tank apparatus; the sensor being calibrated is attached to a mount at a known height and the water level in the tank is adjusted. At each water level, the voltage output of the sensor is recorded. An example of the calibration curves of two of the eight pressure sensors of the vocal fold models is given in Figure 2.22. The manufacturer specified linearity error is 0.80% and the two sensor calibration curves shown in Figure 2.22 are fit with a linear regression yielding first order equations for pressure in terms of voltage. The linear fit gives a norm of residuals of 0.029 V and 0.019 V for the presented sensors. The largest residual of all sensors is 0.0225 V which equates to a pressure discrepancy of 0.316 cmH_2O.

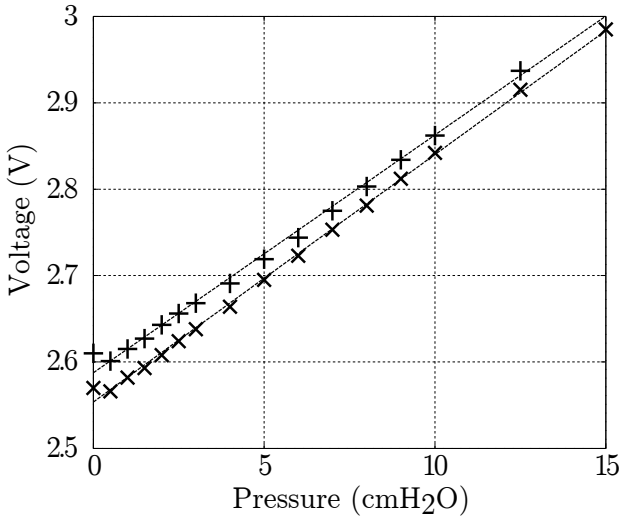

Figure 2.22: Pressure sensor calibration. Results of a calibration test for two pressure sensors, including the calibrated linear fit for each sensor.

2.3 Controller and Software

Section 2.1.2 introduces the broad requirements of a system to control the pseudo-self-oscillating vocal fold facility. In the coupled numerical-experimental framework, the controller provides the dynamical response of the system being modelled. The controller must also control the motion of the actuators to ensure that the dictated dynamical response is realized physically.

2.3.1 Controller selection

The primary requirements that guide controller selection are that the controller offer:

- real-time/deterministic performance
- simple integration with motion system
- at least 12 analog inputs for pressure sensors
- digital input/outputs for switching and indicating
- and be simple to program and debug.

Of the many real-time controller systems from several manufacturers considered, the National Instruments cRIO platform is selected, primarily on the basis of the configurable

nature of the modular design and the out-of-the-box integration with motor controllers. National Instrument's LabView development environment is used to program the cRIO with development conducted on a host computer and sent to the real-time target over a local network. The cRIO-9074 is configured with a 9205 analog voltage measurement module to read pressure sensor inputs, and four 9512 stepper motor control modules to output motion commands to the stepper motor drives for each of the four motion axes.

LabView code is developed to execute the main loop structure outlined previously in Figure 2.5; algorithms to carry out the solution to the dynamical equations, developed in Section 2.3.2, and to solve the inverse kinematic problems, outlined in Section 2.3.3, are developed in MATLAB and implemented on the real-time target using the MathScript node within the LabView environment. The full MATLAB code is included as Appendix C, which the LabView code has been validated against.

2.3.2 Dynamical equation solution

Although any tissue model could in theory be used, the two mass model of Steinecke and Herzel [35] is selected as it is relatively common in speech research and well documented, and it allows for easy incorporation of asymmetric tissue properties. The two masses correspond well with the two degree of freedom motion system described in Section 2.2.2 and the computational requirements of solving the governing equations are very low compared to higher order finite element tissue models. The contact dynamics are updated as per Sommer et al. [47]. The two mass model shown in Figure 2.23 is represented by equations 2.12a and 2.12b for the left and right side masses respectively. The asymmetry factor Q ranges $0 < Q \leq 1$ to control the degree of asymmetry between the left and right sides, as per previous models [35, 47]. An asymmetry factor of $Q = 1$ refers to symmetrical tissue properties. Equation 2.12a and 2.12b are derived assuming that the right vocal fold is affected by the asymmetric properties (*i.e.* $k_{1,\mathrm{R}} = Qk_{1,\mathrm{L}}$). Where $i = [1, 2]$ and $j = [1, 2] \neq i$ for the inferior and superior masses. The masses have length w in the medial-lateral direction (into the page in Figure 2.23).

$$m_{i,\mathrm{L}}\ddot{x}_{i,\mathrm{L}} + r_{i,\mathrm{L}}\dot{x}_{i,\mathrm{L}} + k_{i,\mathrm{L}}x_{i,L} + \Theta(-a_i)c_{i,\mathrm{L}}\left(\frac{Q}{Q+1}\right)\left(x_{i,\mathrm{L}} + x_{i,\mathrm{L}} + \frac{a_{0,i}}{l}\right) + \\ + k_{c,L}(x_{i,\mathrm{L}} - x_{j,\mathrm{L}}) = F_{i,\mathrm{L}} \quad (2.12a)$$

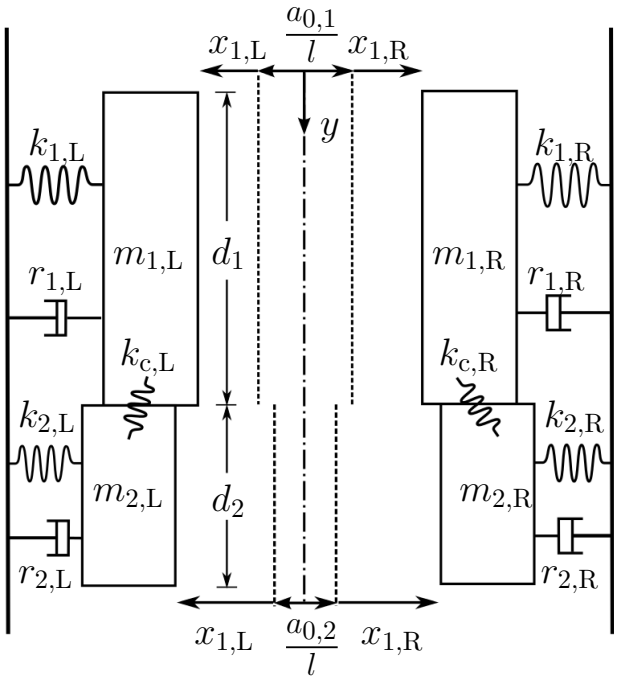

Figure 2.23: Two-mass model of Steinecke and Herzel used as the numerical tissue model governing the dynamic response of the model vocal folds.

$$m_{i,\mathrm{R}}\ddot{x}_{i,\mathrm{R}} + r_{i,\mathrm{R}}\dot{x}_{i,\mathrm{R}} + k_{i,\mathrm{R}}x_{i,\mathrm{R}} + \Theta(-a_i)c_{i,\mathrm{R}}\left(\frac{1}{Q+1}\right)\left(x_{i,L} + x_{i,\mathrm{R}} + \frac{a_{0,i}}{l}\right) + \\ + k_{c,\mathrm{R}}(x_{i,R} - x_{j,\mathrm{R}}) = F_{i,\mathrm{R}} \quad (2.12\mathrm{b})$$

The external forces $F_{i,\mathrm{L}}$ and $F_{i,\mathrm{R}}$ are the aerodynamic forces applied to each mass. For the case of the Steinecke and Herzel model, the force on the inferior mass ($i = 1$) is the integral of the pressure loading across the mass

$$F_{1,\mathrm{L}} = \int_{y=0}^{y=d_1} wP_{\mathrm{L}}(y)\,\mathrm{d}y = wd_1\bar{P}_L \quad (2.13\mathrm{a})$$

$$F_{1,\mathrm{R}} = \int_{y=0}^{y=d_1} wP_{\mathrm{L}}(y)\,\mathrm{d}y = wd_1\bar{P}_R \quad (2.13\mathrm{b})$$

where $P_{\mathrm{L}}(y)$ and $P_{\mathrm{R}}(y)$ are the distributions of surface pressure on the vocal folds moving along the streamwise direction, and w is the thickness of the blocks. The pressure on

the superior masses ($i = 2$) is assumed to be equal to atmospheric pressure, such that $F_{2,\mathrm{L}} = F_{2,\mathrm{R}} = 0$ at all times. The average pressures $\bar{P}_{\mathrm{L}}$ and $\bar{P}_{\mathrm{R}}$ are used in place of the resolved pressure distribution as only the force on the block, and no moment, is of interest.

In actual implementation, the surface pressure measurements are made at discrete locations along the rigid vocal fold model surface and the pressures measured across the experimental vocal fold surface must be scaled to the physiological scale before they can be input into the dynamical model. The average pressure measured across the model surface is calculated and converted to physiological scale as given by equations 2.14a and 2.14b

$$\bar{P}_{\mathrm{L}} = \left(\frac{\Delta P_{phys}}{\Delta P_{exp}}\right) \frac{1}{n} \sum_{k=1}^{n} P_{L,exp,k} \tag{2.14a}$$

$$\bar{P}_{\mathrm{R}} = \left(\frac{\Delta P_{phys}}{\Delta P_{exp}}\right) \frac{1}{n} \sum_{k=1}^{n} P_{R,exp,k} \tag{2.14b}$$

where $P_{L,exp,k}$ is the pressure measured at a pressure tap location on the vocal fold model surface, and n is the number of pressure taps across the model surface. For the present configuration $n = 4$ for the four pressure sensor design outlined in Section 2.2.4.

With the differential equations derived analytically, it remains to implement an algorithm to numerically approximate solutions at each time step of the real-time loop. A 4^{th} order accurate Runge-Kutta scheme is selected to solve the temporally discretized differential equations. The full code is included as Appendix C.

2.3.3 Inverse kinematics and collision detection

Commanding the motion of the physical vocal fold models with the output of the numerical model necessitates the use of functions to move between the numerical and physical domain. In addition to the non-dimensional scaling parameters discussed in Section 2.1.1, a mapping must be computed between the desired position of the vocal fold models and the requisite motor commands to achieve it. A kinematic model of the vocal fold geometry, based on the geometry designed in Section 2.2.1.1, is formulated to relate the actuator inputs to the desired positions dictated by the numerical tissue model as shown in Figure 2.24. The input quantities are the slide positions, s_{L} and s_{R}, and the shaft angles, θ_{L} and θ_{R}. These inputs are related, by the geometry of the vocal fold models, to the positions $X_{1,\mathrm{L}}$, $X_{1,\mathrm{R}}$, $X_{2,\mathrm{L}}$, and $X_{2,\mathrm{R}}$, which correspond to the positions of the masses of the numerical model scaled up by the model scale. These are referred to as the map points. With the geometric

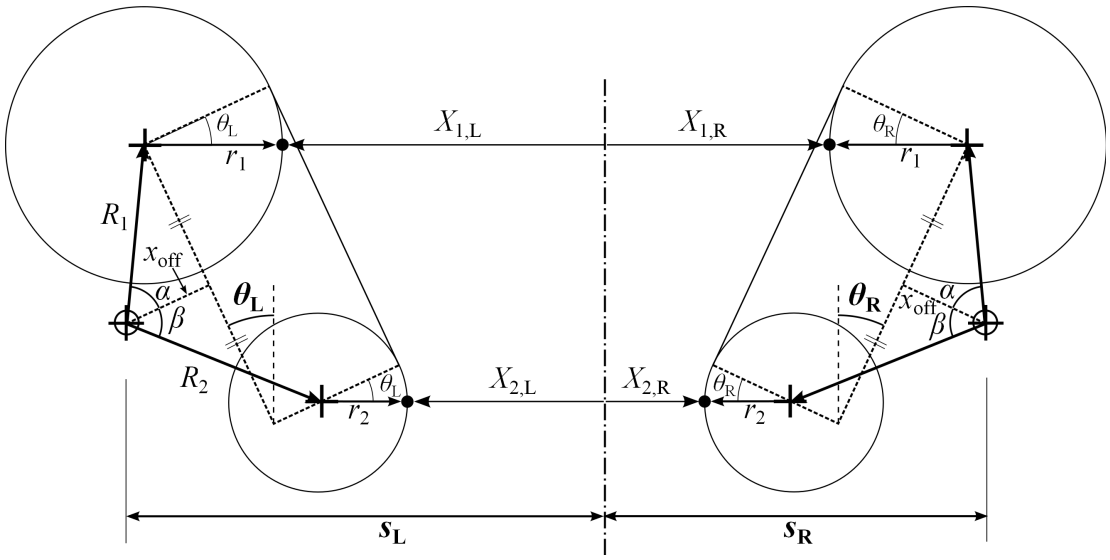

Figure 2.24: Position vector analysis of physical vocal fold model geometry relating the map points to the actuator inputs.

quantities shown in Figure 2.24, the relation between the map points and the actuator inputs are given by

$$X_{1,\mathrm{L}} = R_1 \cos\left(\theta_{\mathrm{L}} + \alpha\right) - s_{\mathrm{L}} + r_1 \tag{2.15a}$$
$$X_{2,\mathrm{L}} = R_2 \cos\left(\beta + \theta_{\mathrm{L}}\right) - s_{\mathrm{L}} + r_2 \tag{2.15b}$$
$$X_{1,\mathrm{R}} = -R_1 \cos\left(-\alpha - \theta_{\mathrm{R}}\right) + s_{\mathrm{R}} + r_1 \tag{2.15c}$$
$$X_{2,\mathrm{R}} = -R_2 \cos\left(\beta + \theta_{\mathrm{R}}\right) + s_{\mathrm{R}} + r_2 \tag{2.15d}$$

Equation 2.15 forms the forward kinematic model giving the map points in terms of the actuator inputs. The inverse kinematic model is sought, giving the requisite actuator inputs to achieve the desired map points. Solving equation 2.15b for θ_L gives

$$\theta_L = \arccos\left(\frac{X_{2,\mathrm{L}} + s_{\mathrm{L}} - r_2}{R_2}\right) - \beta_{\mathrm{L}} \tag{2.16}$$

Substituting equation 2.16 into equation 2.15a gives a relation for s_{L} in terms of the map points and geometry as

$$f_{\mathrm{L}} = R_1 \cos\left[\arccos\left(\frac{X_{2,\mathrm{L}} + s_{\mathrm{L}} - r_2}{R_2}\right) - \beta + \alpha\right] - s_{\mathrm{L}} - X_{1,\mathrm{L}} + r_1 = 0 \tag{2.17}$$

which can be solved for the slide position s_{L}. The same procedure is implemented to form the relationship for s_{R}.

$$f_{\mathrm{R}} = R_1 \cos\left[\beta - \alpha - \arccos\left(\frac{s_{\mathrm{R}} - X_{2,\mathrm{R}} - r_2}{R_2}\right)\right] + r_1 - s_{\mathrm{R}} + X_{1,\mathrm{R}} = 0 \tag{2.18}$$

The non-linearities introduced by the inverse cosine function make a simple inversion impossible. Since derivatives of the functions are available, Newton-Raphson method is used to solve for s_{L} and s_{R}. The derivative of f_{L} with respect to s_{L}, for example, is

$$f'_{\mathrm{L}} = \frac{R_1 \sin\left[\alpha - \beta - \arccos\left(\frac{X_{2,\mathrm{L}} + s_{\mathrm{L}} - r_2}{R_2}\right)\right]}{\sqrt{1 - \left(\frac{X_{2,\mathrm{L}} + s_{\mathrm{L}} - r_2}{R_2}\right)^2}} - 1 \tag{2.19}$$

With the function and its derivative available, the zeroes are estimated by iterative computation of equation 2.20 for both s_{L} and s_{R}, where j is the iteration index, as

$$s_{j+1} = s_j - \lambda \frac{f_j}{f_{j'}} \tag{2.20}$$

The inverse kinematic algorithm must execute at each time step, so rapid convergence of the iterative solution of equation 2.20 is important to maintain determinism at fast loop cycles. Slide positions from the previous time step are used as the initial guess in the iterative solution since, over the small time step, the displacement of the vocal fold model will be small and the previous position offers a very close estimate of the current position. Using such a good initial guess allows for considerable over relaxation without divergence. With $\lambda = 3$, convergence to a tolerance of 0.01 mm is typically achieved in less than ten iterations. The MATLAB function written to implement the inverse kinematic solution is included as Appendix D.

Chapter 3

Flow Tunnel

A flow tunnel is used to represent the air flow from the lungs that passes through the glottis. As mentioned in Section 2.1.1, an aqueous propylene glycol solution will be used as the working fluid to meet the non-dimensional scaling parameters for the vocal fold experiments. The tunnel should provide as steady and as uniform a flow as possible, and must be capable of meeting the flow and pressure requirements dictated by the design of the pseudo-self-oscillating apparatus described in Chapter 2.

3.1 Design

The major components required for the water tunnel are illustrated schematically in Figure 3.1. The pseudo-self-oscillating apparatus (referred to as the apparatus in this section) will be fixed in the test section of the water tunnel, while the remaining components of the tunnel system serve to provide a constant pressure driven flow, as uniformly as possible, through the test section.

The working liquid enters the tunnel at the inlet, maintained at an elevated constant pressure. Low velocity flow in the settling chamber allows any fluctuations from the inlet to dampen, and flow conditioning screens or honeycomb reduce spatial variations and remove non-axial components of the flow. A contraction accelerates the flow, enforcing a negative pressure gradient that reduces boundary layer growth and improves flow uniformity through the test section. Exit drains allow the liquid to leave the flow tunnel and return to a reservoir below. A pump provides the pressure to circulate the water through the system. Given that the flow tunnel should be somewhat portable and fit through a standard double-wide door, the dimensions of the footprint are limited to 4 feet wide by 8 feet long.

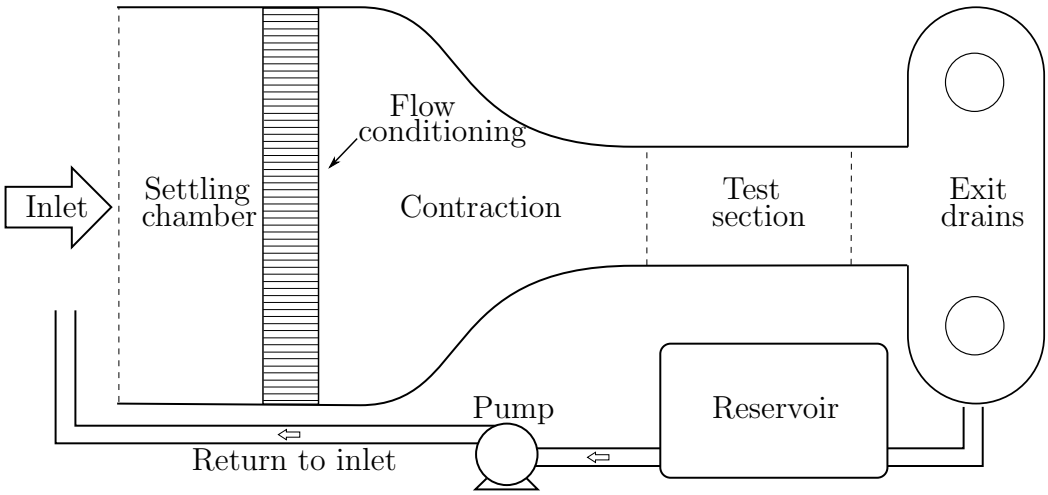

Figure 3.1: Schematic overview of the various components required for the flow tunnel system.

Flow through the test section should be spatially uniform and steady in time. These requirements are more relaxed in the case of the present design compared to typical research tunnels as the natural extreme contraction of the glottis to form the very narrow glottal gap makes this flow less sensitive to the quality of the flow entering the test section. Since flow through the vocal folds is a pressure driven flow, the pressure drop across the vocal fold models in the test section, analogous to the transglottal pressure drop, drives the design of the flow tunnel. A constant elevated pressure at the inlet of the test section provides energy to the flow while the flow rate will vary based on the vocal fold geometry.

3.1.1 Test section

The test section is considered first as the contraction, flow conditioning, inlet, and exit dimensions will all be a product of the test section dimensions and the flow requirements.

3.1.1.1 Dimensions

Inner dimensions of the test section are prescribed by the vocal fold apparatus geometry determined in Section 2.2.1. The test section is the wide enough to fit the left and right M5 geometry vocal fold models opposite one another plus a maximum glottal gap between

the vocal folds of 20 mm. Figure 3.2 shows the important inner dimensions that are to be maintained.

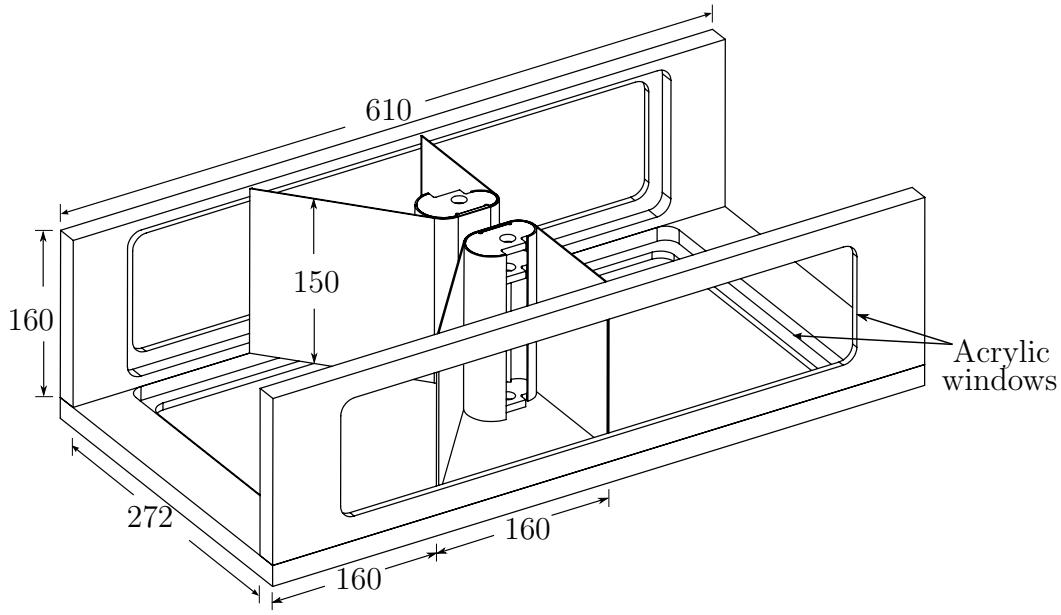

Figure 3.2: Pertinent dimensions of test section, showing some components of the vocal fold apparatus positioned in the test section. All dimensions are in millimetres.

Three acrylic windows are included in the test section design to afford optical axis for measurements and observation. The window in the test section floor, parallel to the 2-D flow plane of interest, provides the primary optical access. Two windows in the test section walls allow for easier positioning of components during installation, viewing any out-of-plane flow, and other observations. A fourth window in the drain section provides optical access for a laser sheet for particle image velocimetry (PIV) measurements. The floor, side wall, and drain windows provide optical access from three perpendicular directions.

The region of particular interest is the exit of the glottis and the behaviour of the jet issuing from the gap between the vocal folds. Consequently, the vocal fold models are biased towards the upstream end of the test section, allowing for easier visualization of the flow downstream of the glottal gap.

3.1.1.2 Estimate of maximum flow rate

An estimate of the maximum flow rate is required to design the components of the tunnel. The pressure drop at the inlet, losses through the honeycomb, pipe sizing, and the pump requirements will all be dictated by the flow rate of the fluid. All design calculations are based on the maximum flow rate as the viscous losses through all components will be greatest.

The expected flow rate is estimated based on previous experimental studies of the M5 vocal fold geometry [22, 25, 27]. Maximum centreline velocities through the vocal fold models, measured in the previous studies for different transglottal pressure drops, provide an estimate of flow rate for the present study. As a conservative estimate, the maximum centreline velocity observed with PIV in the pulsatile [25] and driven [27] studies of Erath and Plesniak are scaled to the parameters of the present experiment. The flow rate and area cannot be scaled directly between different experiments because the aspect ratio of the M5 geometry is not preserved across all studies.

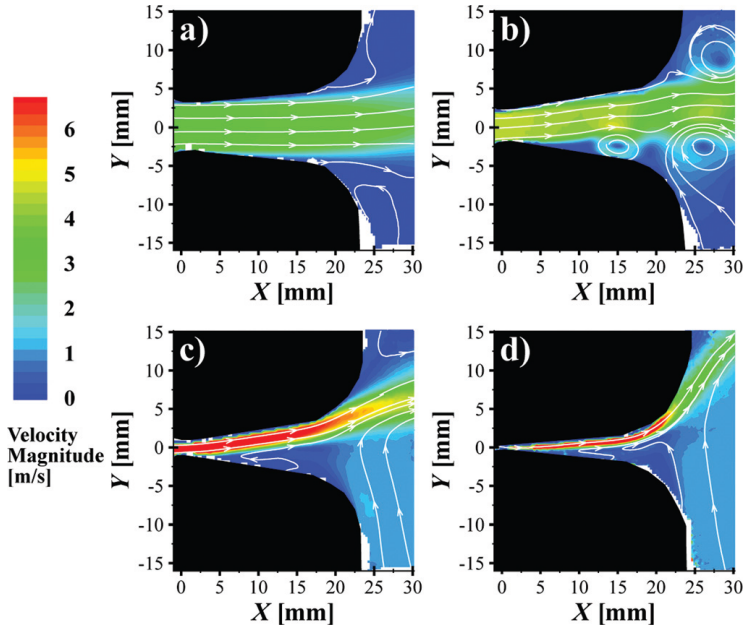

Figure 3.3: PIV results from Erath and Plesniak [27]. Jet velocities for a driven model of the vocal folds at 7.5 times physiological scale, for a physiological scale flow rate of $Q_{\text{mean}} = 253$ mL/s.

The jet velocities shown in Figure 3.3 are used with the minimum glottal gap to estimate

the flow rate per unit length of the extruded geometry. The velocities shown in Figure 3.3 correspond to the experimental scale of the 7.5 times model in air (3.14 times the velocity scale of the present study). Velocity fields throughout the oscillation period are given at $t/T_{\text{open}} = 0.6$, $t/T_{\text{open}} = 0.7$, $t/T_{\text{open}} = 0.8$, and $t/T_{\text{open}} = 0.9$ for Figure 3.3 a) through d) respectively. Flow rates per unit length for the open glottis of Figure 3.3a) and Figure 3.3b) are both approximately 0.02 m^2/s and the closing glottis of Figure 3.3c) yields a flow rate per unit length of approximately 0.012 m^2/s. Scaling these values to the velocity and length scales of the present experimental facility gives a prediction of $Q_{\text{max}}/l = 0.013$ m^2/s. For the 150 mm long M5 model extrusion used in the present study, this results in a estimated maximum flow rate of $Q_{\text{max}} = 0.0019$ $\text{m}^3/\text{s} = 1.9$ L/s for the physiological upper limit of speech.

3.1.2 Inlet

In contrast to most water tunnels, which provide constant flow rate through a closed recirculating loop, this tunnel provides a constant static pressure difference across the model. The flow rate will vary based on the changing geometry of the apparatus. To this end, a stack of fluid at the inlet provides constant head pressure. A pump refills the stack constantly, and the excess flow is diverted back to the reservoir, as shown in Figure 3.4b). The height of the overflow tap is adjusted to vary the head pressure such that $P_{\text{inlet}} = \rho g h$. The stack was originally configured such that flow enters the stack from the top and returns to the reservoir from a tap below. This configuration, however, caused significant mixing of air into the inlet liquid which resulted in air entering the tunnel. The configuration shown in Figure 3.4b), with the inlet below the return tap, solved the air entrainment problem.

Three inlet stacks provide flow into the settling chamber. The inlet pipes are constructed from ABS schedule 40 pipe of diameter $D = 3$ inches ≈ 76 mm and spaced evenly across the inlet a distance $s = 340$ mm centre-to-centre (see Figure 3.4a)). The pipes are perforated with small holes of diameter $d = 1/2$ inch ≈ 13 mm. The number of holes in the pipe is selected such that the total area of the holes is equivalent to the cross sectional area of the pipe, that is

$$\begin{aligned} A_{\text{holes}} &= A_{\text{pipe}} \\ N\frac{\pi}{4}d^2 &= \frac{\pi}{4}D^2 \\ N &= \frac{D^2}{d^2} \end{aligned} \tag{3.1}$$

which, for the hole and pipe diameters selected, requires $N = 36$ holes for each of the three

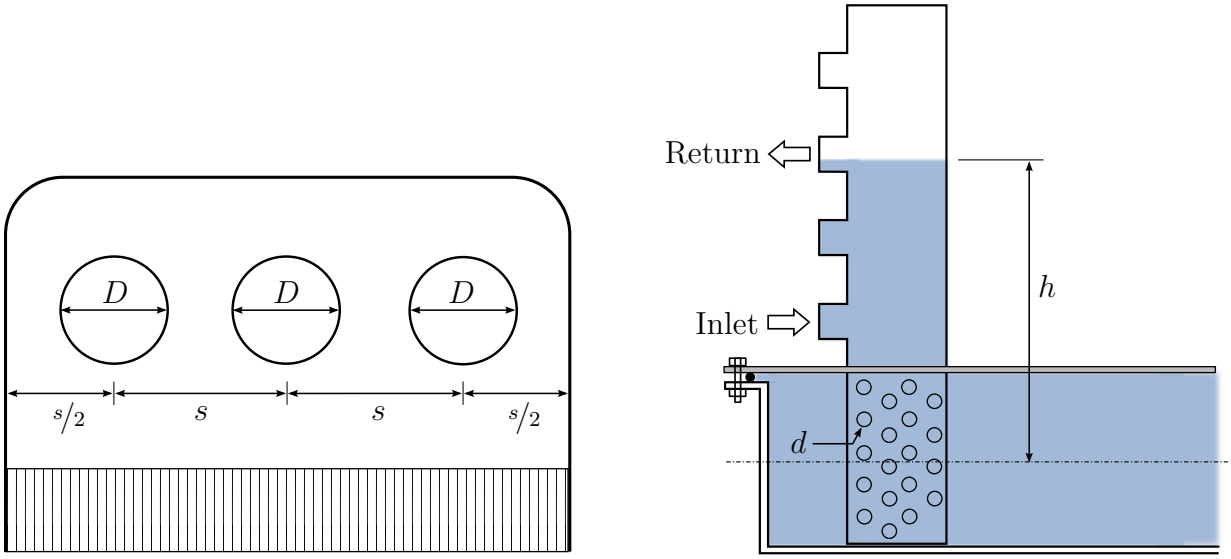

Figure 3.4: Inlet section of flow tunnel. a) Plan view showing three inlets evenly spaced across the inlet section of the settling chamber, and b) side view showing the stack providing static pressure to the inlet section.

inlet pipes. Based on the maximum flow rate estimated in Section 3.1.1.2, the maximum Reynolds number within the inlet pipes is $Re_{\mathrm{D,inlet}} \approx 10^3$ and $Re_{\mathrm{d,inlet}} \approx 150$ through the perforations.

3.1.3 Flow conditioning

Flow conditioning elements are incorporated into the tunnel design in an effort to improve the spatial and temporal uniformity of the flow. The flow conditioning elements also ensure the flow conditions at the test section are as specified for the model.

3.1.3.1 Honeycomb

Screens and honeycomb are used ubiquitously in flow tunnels as flow conditioning elements. When designed correctly, the pressure drop across the element slows high velocity flow regions and improves flow uniformity while reducing turbulence intensity [49–51]. Honeycomb, being more structurally robust than screens, is better suited for use in a water tunnel. Honeycomb offers the further advantage of minimizing lateral velocity components,

as the developed flow exiting the honeycomb cell will ideally only contain an axial component. Existing literature on the topic of flow conditioning with honeycomb is primarily anecdotal and observation based [49, 50], but some more formal analysis has also been considered [51, 52].

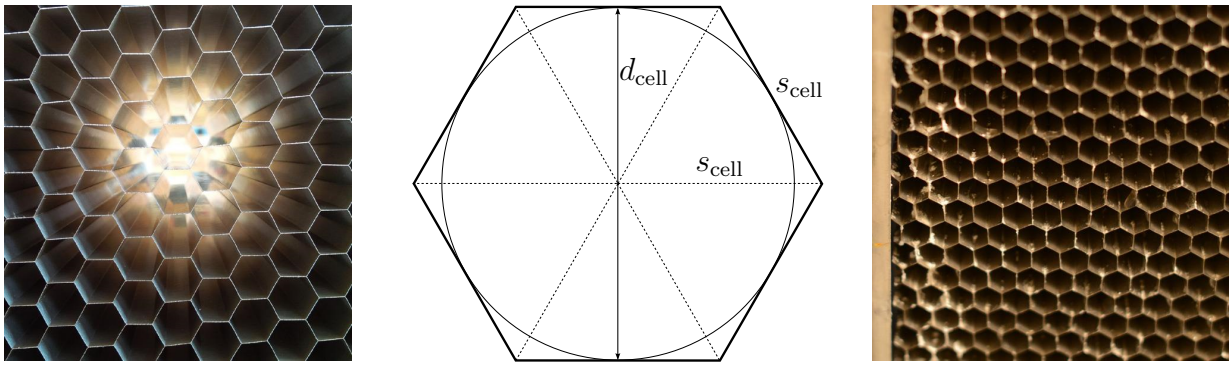

a) b) c)

Figure 3.5: Honeycomb flow conditioning element. a) Close up view of honeycomb cells before installation in the tunnel, b) schematic view of the geometry of the hexagonal honeycomb, and c) fouled honeycomb cells after testing in non-deionized water.

For the present honeycomb the length of the cell is $L_{\text{cell}} = 3.75$ inches and each cell has a flat-to-flat distance of $d_{\text{cell}} = 0.35$ inches, referring to Figure 3.5. Assuming the honeycomb cells are regular hexagons, this corresponds to a side length of $s_{\text{cell}} = 0.202$ inches. The ratio $\frac{L_{\text{cell}}}{d_{\text{cell}}} = 10.7$ is close to the ideal range proposed by Mehta *et al.* [49, 50]. The honeycomb spans the width and height of the settling chamber, which requires the honeycomb to be 18 cells in height and 130 cells in width giving 2340 cells total; also within the recommended ranges [49, 50].

Annihilation of the transverse fluctuations at the exit of the honeycomb cells is dependent on the assumption that fully developed flow has been reached in the length of the cell [52]. Based on maximum flow rate estimated in Section 3.1.1.2, the Reynolds number within the cell based on the cell diameter is $Re_{\text{d,cell}} = 11.5$, making it well within the laminar regime. This analysis assumes the flow to behave as it would in a circular duct of diameter d_{cell}, such as the circle inscribed within the hexagon of Figure 3.5b). For laminar pipe flow, the commonly accepted correlation to estimate the entrance length L_{e} is

$$\frac{L_{\text{e}}}{d} \approx 0.06Re \tag{3.2}$$

based on laminar boundary layer development [40, 53]. The very low velocities in the settling chamber and the relatively high viscosity of the propylene glycol working fluid

lead to a very low entrance length of $L_e \approx 6$mm. Thus, the flow is fully developed within the length of the cells and leaves the cell with a laminar velocity profile. In addition to damping turbulent fluctuations through laminarization of the cell flow, the honeycomb structure itself produces turbulence. This is primarily attributable to the break up of the mean profile emanating from each cell and subsequent interaction with its neighbours [51]. Additional screens downstream of the honeycomb ameliorate this effect, but in the present work the removal of non-axial flow components is paramount to minimizing turbulent fluctuations. Screens can be installed after testing of the tunnel if further reduction of turbulence intensity is required.

It has been observed that in practice, the fouling and obstruction of the honeycomb by debris and deposits can have a greater effect on the resulting flow conditions than the selection of the honeycomb geometry itself [54]. As shown in Figure 3.5c), considerable fouling of the honeycomb cell walls takes place after relatively brief exposures to non-deionized water. The deposits are primarily mineral scale which have been found to be easily removed with a short bath in strong acid and scrubbing with a soft bristle brush. Deionized water is used in the flow tunnel, which significantly reduces the rate of fouling. However, as discussed in Section 4.3, the use of electrolytic flow visualization techniques will exacerbate the fouling and deterioration of the honeycomb structure. To this end, the honeycomb element is designed to be modular and easily removable for cleaning and replacement.

3.1.3.2 Contraction

Contractions serve to increase flow uniformity and reduce turbulent fluctuations by accelerating the flow from the low speeds of the settling chamber to the desired inlet velocity and pressure at the test section. This allows for the inlet and flow conditioning elements (honeycomb in the case of the present design) to work at lower flow speeds, where the pressure drops will be reduced by a factor of c^2 where c is the contraction ratio [49, 50]. The contraction ratio is defined as $c = \frac{A_1}{A_2}$ where A_1 and A_2 are the areas at the inlet and outlet of the contraction respectively. For the present flow tunnel, a contraction ratio of $c = 3.73$ is selected. The selected contraction ratio is primarily the result of practical constraints rather than rigorous optimization; to match the constraint of keeping the outer dimension below 48 inches, the maximum width achievable inside the tunnel is 40 inches. Although lower than the typical range for low speed air and water tunnels of $c = 10$ to $c = 25$, it is of less concern for the present design. The vocal fold model geometry is such that (referring to Figure 2.8) it inherently contains a contraction of $c_{vf} \approx 25$. When the inherent contraction of the vocal fold model is included, the contraction ratio from the

settling chamber to glottal duct is equivalent to $c_{\text{eq}} = 100$, which is well above the range typical of low speed flow tunnels!

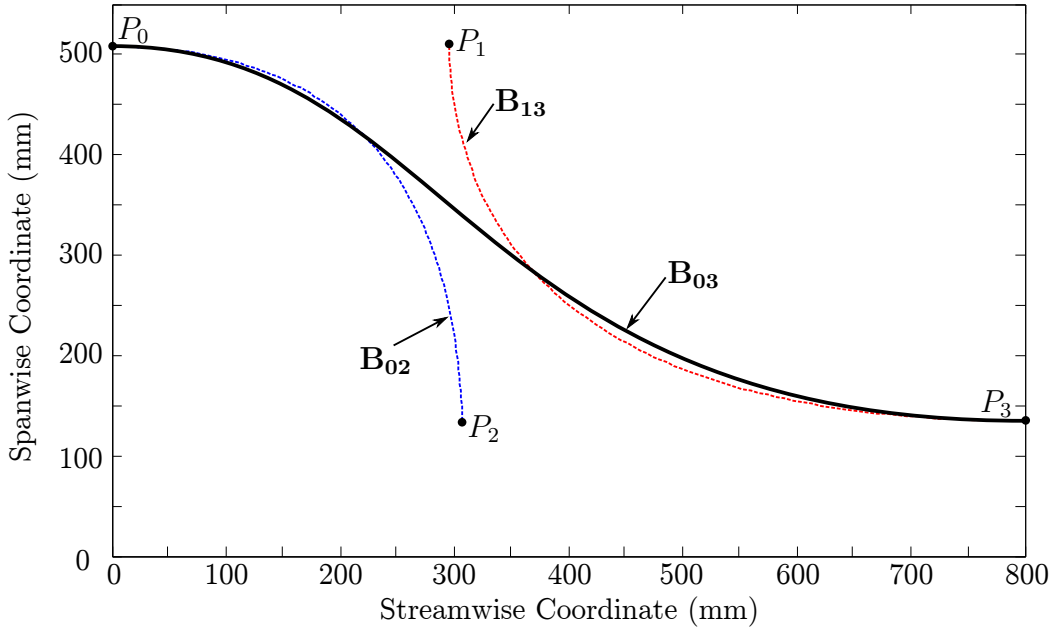

Figure 3.6: A cubic Bézier curve definition of the contraction contour, showing the two quadratic Bézier curves, $\mathbf{B_{02}}$ and $\mathbf{B_{13}}$ that are linearly combined to produce the cubic.

With the contraction ratio established at $c = 3.73$ based on dimensional constraints, the contour and the length are the remaining variables of interest [55]. Determining the length of the contraction is crucial because separation can occur if the the contraction is too short, and increased boundary layer growth can occur in a long contraction. Also, more pertinent to the present analysis, the limited space available means the contraction should be as short as is feasible to leave length available for other tunnel elements.

The contraction contour is defined such that it transitions smoothly from the parallel walls of the settling chamber and the test section. This implies the curvature is zero at the upstream and downstream extremities of the contour. Prior works have employed a 5^{th} degree polynomial or two cubic polynomials with a shared tangential intersection point [55, 56]. For ease of design and manufacturing, the same contour can be represented with a cubic Bézier curve. Bézier curves are ubiquitous in computer design and graphics and allow for simple communication of curvilinear geometries [57].

A Bézier curve is a parametric curve defined by a series of control points. The geometry of the tunnel contraction, with parallel start and end points, necessitates a cubic Bézier

curve which is based on four control points as shown in Figure 3.6. A cubic Bézier curve can be represented by the linear combination of two quadratic Bézier curves, $\mathbf{B_{02}}$ and $\mathbf{B_{13}}$, where

$$\mathbf{B_{02}}(t) = (1-t)[(1-t)\mathbf{P_0} + t\mathbf{P_1}] + t[(1-t)\mathbf{P_1} + t\mathbf{P_2}] \tag{3.3a}$$
$$\mathbf{B_{13}}(t) = (1-t)[(1-t)\mathbf{P_1} + t\mathbf{P_2}] + t[(1-t)\mathbf{P_2} + t\mathbf{P_3}] \tag{3.3b}$$

for $t \in [0, 1]$. The points $\mathbf{P_0}$ and $\mathbf{P_3}$ are the endpoints of the contour, while the two inner points $\mathbf{P_1}$ and $\mathbf{P_2}$ define the direction that the curve leaves and approaches the endpoints. Linearly combining the curves of Equation 3.3 gives the cubic Bézier

$$\mathbf{B_{03}}(t) = (1-t)\mathbf{B_{02}}(t) + t\mathbf{B_{13}}(t) \tag{3.4}$$

The distance between $\mathbf{P_0}$ and $\mathbf{P_1}$ is less than the distance from $\mathbf{P_2}$ and $\mathbf{P_3}$, this biases the curvature of the contraction towards the inlet. This reduces the curvature at the exit of the contraction and gives a smooth transition to the test section.

Use of the Bézier curve definition allows the contour of the contraction to be considered mathematically, simply drawn and manipulated in a computer aided design environment, and plotted at 1:1 scale such that it can be replicated in construction.

3.1.4 Exit

Once the fluid passes through the model in the test section it must return to the reservoir to feed the pump and continue the flow loop. A simple drain, like a bath tub drain, would cause the formation of 3-D vortical structures around the drain. These affects would diffuse upstream and could introduce 3-D effects in the test section.

Circular drain housings in the exit section, as shown in Figure 3.7, are added to encourage the flow to smoothly change direction and enter the drain. The circular housing has a diameter $D_e = 12$ inches ≈ 305 mm. A vertical section of pipe of diameter $D_d = 3$ inches ≈ 76 mm spans from the floor to the ceiling of the exit section. The pipe is perforated with holes, similar to the inlet stacks in the settling chamber (see Figure 3.4), that also encourages 2-D flow. ABS schedule 40 pipe is used to make the drains. The circular housings around the drains are extended to sweep an arc of 260°in an effort to confine the effect of the rotating fluid to the drain section. This helps to prevent the presence of the drains from diffusing upstream and affecting the flow in the test section.

As mentioned in Section 3.1.1, an acrylic window is included in the drain section. The window affords optical axis in the plane perpendicular to the axial flow direction.

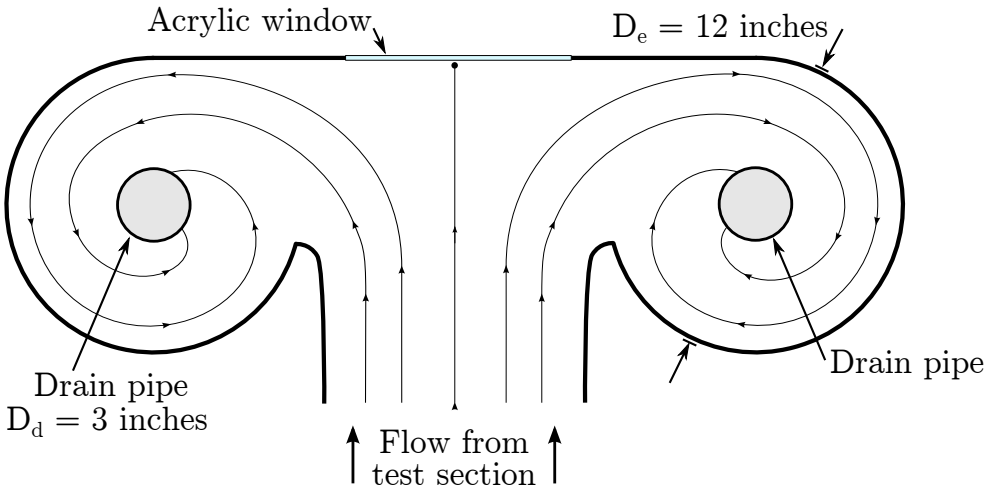

Figure 3.7: Schematic of design of exit drains, showing sketched streamlines of the desired flow.

3.1.5 Pump

With the flow requirements found in Section 3.1.1.2, the specification and selection of an appropriate pump can begin. The maximum flow rate estimate is $Q_{\max} = 0.0019$ m^3/s, more commonly expressed in the imperial unit U.S. gallons per minute (GPM) for water pumps, gives approximately 30 GPM. The flow rate will likely exceed the average value for brief periods as transients occur in the tunnel or if the dynamics vary significantly from the previous experimental work the estimate is based on. Thus a 50% margin is added to the flow rate requirement of the pump, giving 45 GPM.

A centrifugal pump is selected as the required head is relatively low. The pump only needs to provide sufficient head to pump the fluid from the reservoir to the inlet stack – a change of height of approximately 1.5 m, or a pressure change of 14.7 kPa for water. Powering the pump with an electric motor is the best option given the low power requirements, accurate speed control required, and laboratory operating environment.

Pumping the propylene glycol solution, with a viscosity 10 times that of water, will reduce the pump performance compared to published performance data from the manufacturer. Figure 3.8a) shows the maximum efficiency typical of centrifugal pumps pumping liquids with densities greater than water [58]. For $\mu/\mu_{H_2O} = 10$, the maximum efficiency drops from 85% to 76%. The pump flow rate requirements are adjusted accordingly so that the pump provides a name-plate flow rate of 51 GPM. A centrifugal pump, shown in Figure 3.8b), is selected to meet the specifications for flow rate and head. The perfor-

mance data for the pump is shown (for water) as Figure 3.8c). The pump comes aligned and face-mounted to a 1.5 HP 3-phase totally enclosed fan cooled motor.

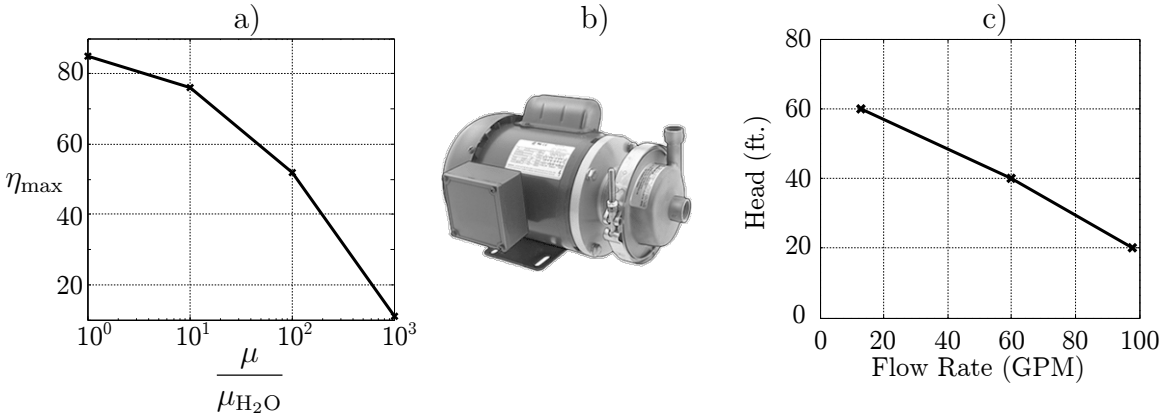

Figure 3.8: a) Maximum efficiency of centrifugal pumps for pumping fluids with viscosities greater than water (data from [58]), b) the selected centrifugal pump coupled to a 1.5 HP electric motor, and c) pump performance data from manufacturer.

Since it is not feasible to place the pump at a significantly lower elevation than the reservoir, there will only be approximately 6 inches of head available at the pump inlet. This increases the risk of cavitation, and it is therefore necessary that the pump have a required net positive suction head (NPSH) close to zero and that the pump be run at reduced speed to mitigate the risk of cavitation.

Although the design of the constant pressure inlet, shown in Section 3.1.2, does not require control of the flow rate, it will still be advantageous to control the speed of the pump. A variable frequency drive (VFD) can be used to modulate the frequency of the 3-phase inlet voltage to the motor. This allows for speed ramp up and ramp down, and more flexibility of operation.

3.1.6 Structural requirements

A frame is needed to support the weight of the tunnel, fluid, reservoirs, and hardware. The frame is supported on casters to increase mobility. The volume of fluid contained in the tunnel is estimated at approximately 200 L. When all of the fluid is in the tunnel, the reservoirs must maintain a sufficient level to keep the pump inlet immersed, so an additional 80 L of fluid is needed. The weight of the working fluid is 279 kg, or 615 lbs. The tunnel adds approximately 150kg to this, plus any additional hardware or equipment,

meaning the support structure must be capable of supporting in excess of 450 kg, or 1000 lbs.

Figure 3.9: Steel supports to brace acrylic ceiling against pressure loading, shown during preliminary leak testing.

In addition to the weight, the tunnel also has to withstand the pressure the fluid applies to the inner surfaces. Transparent acrylic plastic is an ideal choice for the tunnel ceiling, as the improved optical access is an asset in monitoring the flow throughout the tunnel. However, referring to Appendix A, the deformation of an acrylic sheet is too great if unsupported over the span of the tunnel. The simple analysis conducted in Appendix A predicts a midpoint deflection of 9 cm and radial stress within 50% of the ultimate tensile strength of the material. To this end, steel supports are included across the span of the tunnel ceiling. The supports are fixed with threaded rod to the tunnel base to transfer the pressure load from the ceiling, as shown in Figure 3.9.

3.2 Construction

With the design considered in Section 3.1, the flow tunnel is constructed. A brief overview of the materials and techniques used for tunnel construction are provided herein.

3.2.1 Material selection

The complex geometries of the contraction and the exit drain housings limit the selection of appropriate building materials. Stainless steel, aluminium, plastic, and fibreglass are considered as they can all be formed into almost arbitrary curved surfaces and can be constructed to be waterproof. Stainless steel and aluminium are ruled out based on cost, and the fact that outside speciality labour would be required to form and weld the metal. A plastic, such as acrylic or lexan, lacks the structure to form the entire tunnel, and cutting, bending, and bonding the acrylic to sufficient accuracy and adequate leak resistance would be difficult. A wood frame with fibreglass skin for structural reinforcement and waterproofing is selected. Wood and fibreglass provide excellent formability, strength, and water resistance.

Epoxy resin is selected over polyester resin as it offers improved strength and is easier to work with. Polyester resin contains volatile solvents; as the solvents evaporate they leave small voids in the cured product. This results in increase permeability to water and are therefore at increased risk for failure to water delamination and rotting of the wood substrate. A high performance epoxy resin system, the West System, is selected. This system is specifically designed for use on wood in high performance yacht construction and repair. Glass cloth is used as a reinforcement in the epoxy matrix. The composite material is adhered directly to the underlying porous wood surface.

3.2.2 Layout and frame

A 4 foot by 8 foot sheet of 3/4 inch thick Baltic birch plywood forms the base of the water tunnel. The curved contour for the contraction and exit drain enclosures, created with design software, are plotted on paper at full scale and traced onto the plywood base. The circular exit drain housings are formed from polystyrene foam fitted into a wooden enclosure. The polystyrene foam is coated with resin and chopped glass fibre mixture that is allowed to cure and then is sanded smooth, as shown in Figure 3.10.

Replicating the contour of the contraction smoothly and accurately is paramount to smoothly accelerate the flow and prevent separation. The contour of the contraction walls are created by first screwing 1×2 ribs to the plywood base. The ribs are positioned and orientated such that they are tangent to the wall contour. Continuous strips of 1/4 inch plywood, steamed and bent, are glued along the ribs. The plywood skin requires even clamping along its length to ensure good adhesion and to prevent flat spots from forming.

The back wall of the settling chamber is formed in a manner similar to the contraction,

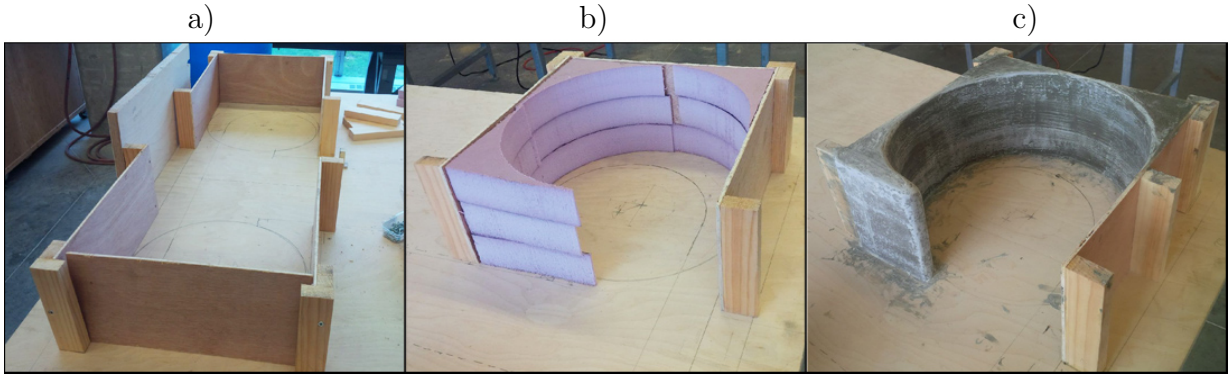

Figure 3.10: Exit drain enclosure construction. a) wooden box outline from 1×2 pine ribs and 1/4 inch plywood, b) polystyrene inserts to give circular geometry, and c) stranded glass fibre and resin layer for structure.

as seen in Figure 3.11c), and foam inserts are again used to build up a radius in the corner to mitigate flow separation. A flange is formed along the top of the ribs that extends around the entire perimeter of the tunnel. The flange is built from 1/2 inch plywood and provides a surface for the tunnel ceiling to seal and clamp against while also increasing the rigidity of the assembly. In Figure 3.11c), the right side of the contraction has the plywood flange installed in the photograph, while the left side does not.

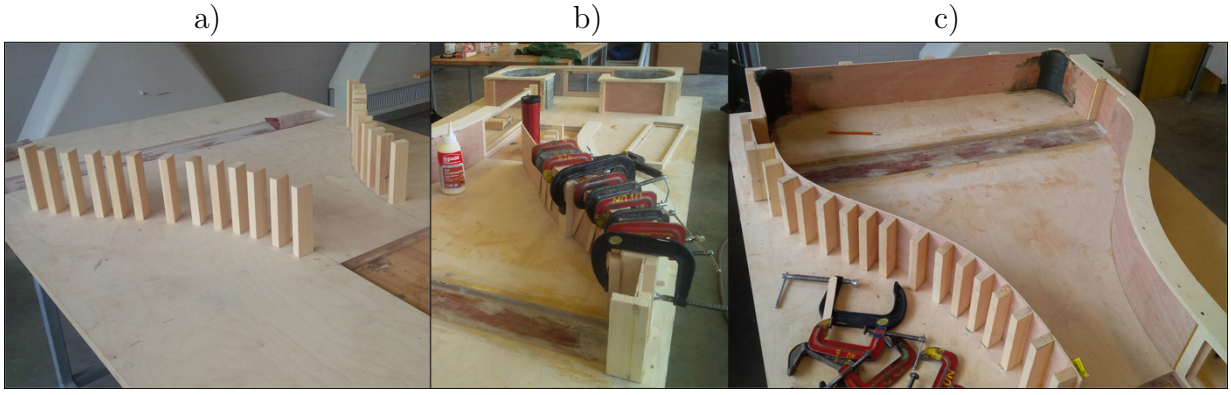

Figure 3.11: Construction of contraction contour. a)vertical 1×2 ribs fixed to plywood base to form contour, b) clamping to glue plywood skin onto ribs, and c) finished contour once clamps are removed.

Frames are cut from pieces of 3/4 inch Baltic birch plywood to hold the acrylic windows around the test section and at the exit drain section. A 1/2 inch deep relief is cut around

the extremity of the window frame such that a 1/2 inch thick acrylic window can be flush mounted with the wall. The wooden window frames are fixed in the wall assembly, supported by 1×2 ribs, and topped with the flange, as seen in Figure 3.12. To prevent damage due to any strain on the fibreglass while moving or shifting the tunnel, the plywood base is mounted to a welded steel support frame. For rigidity and to prevent warping of the plywood, the plywood base is bolted directly to tapped holes in the steel tubing of the frame.

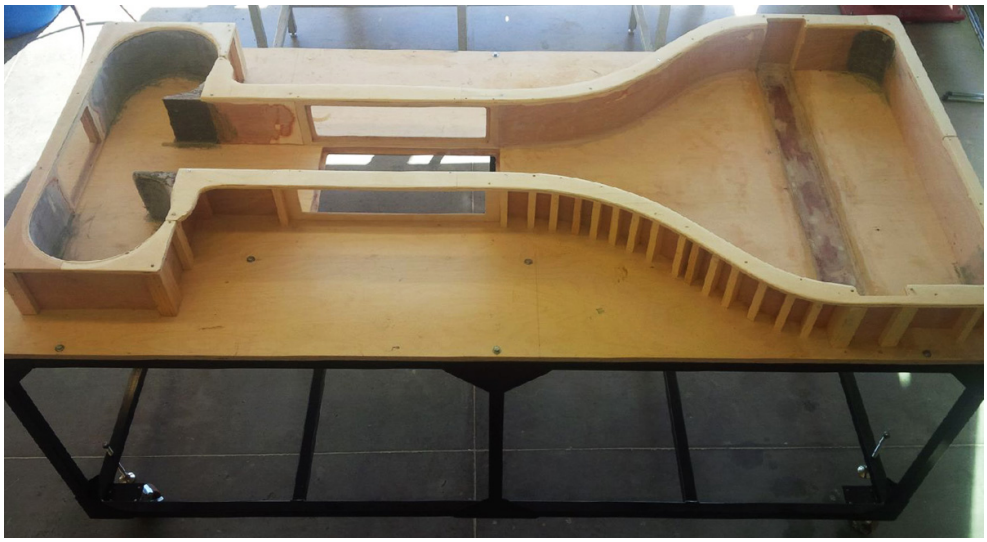

Figure 3.12: Completed wood substructure, mounted to steel frame, ready for fibreglass application.

3.2.3 Fibreglass coating

The wood subframe is rigidized and waterproofed with the application of multiple layers of fibreglass cloth and epoxy resin composite material. As mentioned in Section 3.2.1, West System two-part epoxy resin is used as a resin matrix, and fibreglass cloth provides fibre reinforcement. Two types of fibreglass cloth are used: 7.25 oz./yard midweight standard weave cloth for large open sections such as the tunnel floor, and 8.8 oz./yard modified twill cloth for bends and intersections. Modified twill, with a two-under-two-over weave, possesses better draping ability than standard weave, this makes it perform much better in tight radii such as around the walls and flange.

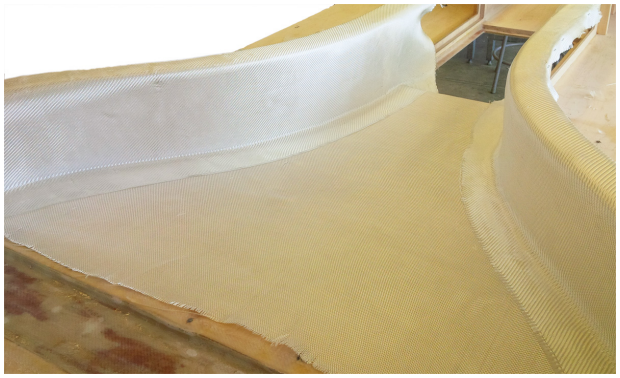

Figure 3.13: Fibreglass cloth layup on contraction floor and walls before resin application.

All wetted areas of the tunnel are covered with at least two layers of fibreglass cloth saturated with resin. Wood seams are overlapped by atleast two inches of cloth on each side to ensure water resistance and rigidity. Any excess glass fibres are trimmed and cloth transitions are faired and sanded smooth. After sanding and washing, 4 additional layers of resin are applied. The cured resin top coats are dry and wet block sanded for fairing and to remove any bubbles formed by out-gassing. Finally, a tipped finish coat is applied. Amine blush is removed with warm water between resin coats, and after the finish coat is cured.

3.3 Flow characterization

Before the pseudo-self-oscillating vocal fold apparatus is installed into the flow tunnel, the flow within the empty test section must be characterized. Although prior vocal fold model flow studies have not taken extensive care to control and characterize the incoming flow, it is still important to characterize the spatial and temporal variation of the incoming velocity field. Since the oscillatory dynamic behaviour of the vocal folds is of paramount interest, any strong periodic fluctuations of the incoming flow field must be well characterized.

The working fluid of the flow tunnel is an aqueous propylene glycol mixture with a viscosity of $\mu = 0.01$ Pa s. For shakedown testing and flow characterization, where the tunnel needs to be drained and refilled often for adjustment and possible leakage, water is used in place of the glycol solution. Using water for testing saves considerable cost and time and allows for greater flexibility in testing. Of course, the order of magnitude reduction of viscosity will likely have considerable effect on the observed flow behaviour.

Flow coming into the glottal model should be relatively uniform across the span and height of the empty test section. To reiterate from Section 3.1.3.2, the inherent contraction ratio of the vocal fold model geometry relaxes the constraints on flow uniformity, as compared to typical research flow facilities. A laser Measurement Sciences Enterprises miniLDV Doppler velocimetry (LDV) system is employed to measure the axial flow velocity u at discrete locations across the test section, as shown in Figure 3.14.

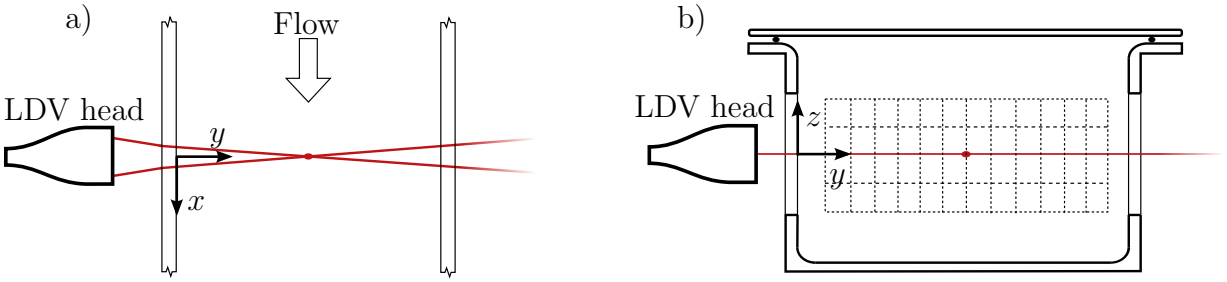

Figure 3.14: Schematic of LDV measurement system in tunnel test section. a) a top view of the partial test section, and b) cross-section view through the test section showing the 65 measurement station locations

The LDV measurement head is mounted on a two-axis stage to move positions in the y and z directions, referring to Figure 3.14, to measure at 65 locations across a single x plane. To capture enough data to achieve reasonable predictions of the average and fluctuating velocity, at least 3000 burst measurements are recorded at each station. The average data rate across all stations is 12.9 Hz, but the data rate and signal quality is significantly higher at measurement locations close to the $y = 0$ wall. For the 5 stations at $y = 26$ mm the average data rate is 18.8 Hz, while for the stations at $y = 266$ mm the data rate drops to 7.1 Hz. Both the spatial and temporal variation of axial velocity u are evaluated with the LDV traverse data.

3.3.1 Spatial variation

For a x-plane through the midpoint of the test section, the spatial variation of mean axial velocity $\bar{u}(y, z)$ is measured at thirteen y-positions from $y = 26$ mm to $y = 266$ mm at 20 mm intervals. The traverse is repeated along five z lines from $z = 53$ mm to $z = 113$ mm at 15 mm intervals. All bursts at a given station that have a signal to noise ratio SNR ≥ 5.0 are retained and averaged. The results of the mean axial velocity for the 65 measurement stations are shown in Figure 3.15.

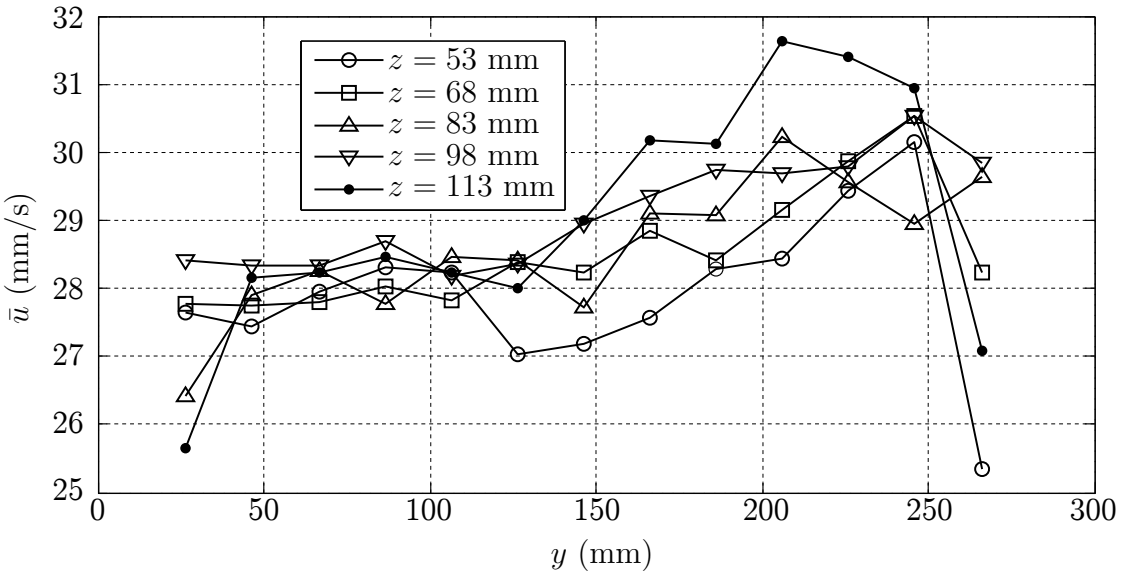

Figure 3.15: Mean axial velocity across the measurement grid.

The spatial variation of mean velocity is greater than what is typical of research tunnels. Spatial variation is especially high towards the wall opposite to that of the measurement head. The variance results shown in Figure 3.16 do show increased variance of the measurements recorded close to the far wall, at $y = 266$ mm; the large variation of mean velocity for stations at this y position is likely attributable to increased measurement error close to the wall.

Since PIV and surface pressure measurements for the vocal fold apparatus are all made within the small glottal duct and at the vertical midplane of the test section, the spatial variations observed herein are not likely to drastically affect results. If the spatial variation is found to be unacceptable large, screens can be added downstream of the honeycomb assembly to provide more uniform flow.

3.3.2 Temporal variation

For the same measurement stations described in Section 3.3.1, the temporal variation of the axial velocity at each location is evaluated. The standard deviation of all velocity measurement bursts that meet the SNR ≥ 5.0 criteria at each location is calculated. The relative standard deviation for each location is shown in Figure 3.16.

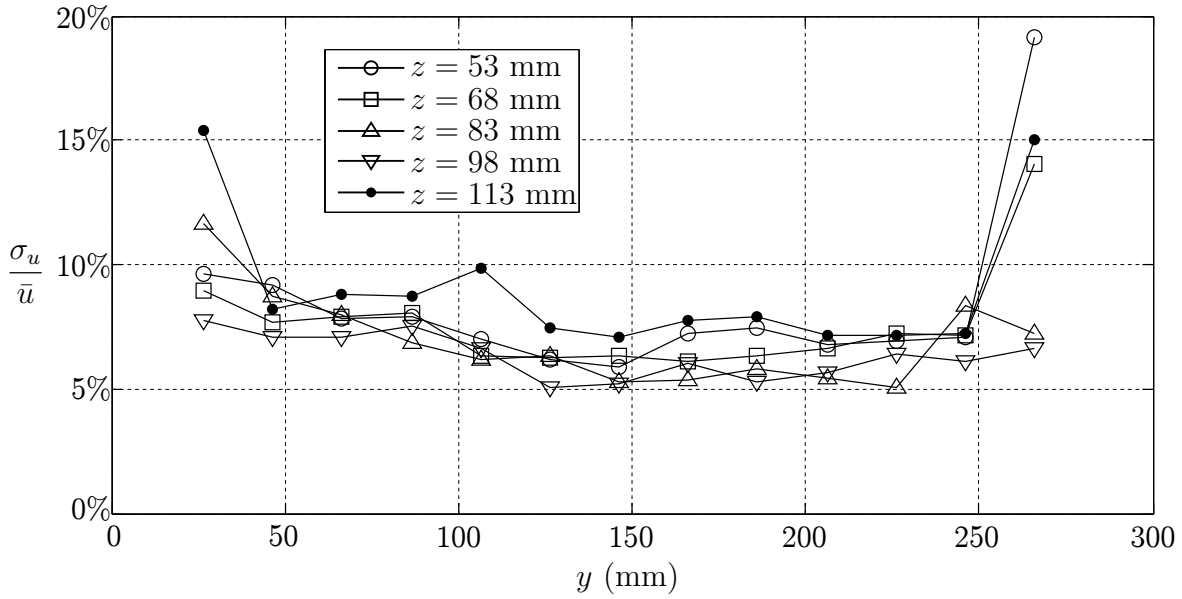

Figure 3.16: Relative standard deviation of time history of axial velocity measurements recorded at each measurement station in test section.

Near the tunnel walls, for $y = 26$ mm and $y = 266$ mm, the relative standard deviation is approximately double to the deviation near the midline of the tunnel. This is likely attributable to the increased measurement error near the wall, and the greater relative contribution of the varying velocity component at the reduced mean velocity of the boundary layer. For the central seven measurement stations the average relative standard deviation is 6.81%. Again these temporal variations are likely to be further damped by the presence of the large contraction of the vocal fold models.

Chapter 4

Results and Validation

To successfully model the fluid-structure interactions of the vocal folds with the coupled numerical-experimental facility, all of the components outlined in previous sections must function as specified. Characterizing the response of the system is complicated by the multitude of individual components and by the interconnectivity and simultaneity of their operation.

As a result, the system was developed and validated in multiple phases, each with incremental increases in complexity. The early phases utilize a single degree of freedom structure model; first, to characterize the open loop response to a step change in pressure, and second to test the response of a flexibly mounted flat plate perpendicular to a flow of air. Once the dynamic solver and slide actuation system are validated for a single degree of freedom, a two degree of freedom model of a jet impinging perpendicular to the vocal fold surface is pursued. The two degree of freedom impinging jet configuration necessitates correct operation of all of the components described in Chapter 2. The vocal fold geometry of the apparatus is tested in the flow tunnel to ensure the behaviour is acceptable.

4.1 Single degree of freedom system

A simple single degree of freedom (1-DOF) spring-mass-damper system archetypal to dynamical analysis is considered. The 1-DOF oscillator, shown in Figure 4.1, consists of a spring-mass-damper dynamical system under an applied load F. Integrating the pressure distribution $P(r)$ across the surface gives the applied load F. The differential equation

dictating the response of the system is

$$\ddot{x} + 2\zeta\omega + \omega^2 x = \frac{F}{m} \tag{4.1}$$

where $\omega = \sqrt{k/m}$ and $\zeta = b/\left(2\sqrt{mk}\right)$ are the natural frequency and damping of the system respectively. The algorithm described in Section 2.1.2 is implemented with equation 4.1 as the dynamical model.

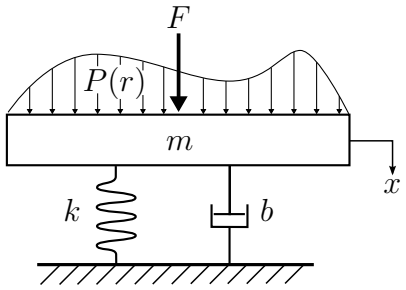

Figure 4.1: 1-DOF model that governs the structural response of the test apparatus.

While Equation 4.1 provides the numerical structure model, the experimental flow aspect of the coupled system is shown in Figure 4.2. A circular aluminium disk is mounted to a RB12 linear stage (as described in Section 2.2.2.1) to translate the disk in the streamwise direction. The disk is instrumented with pressure taps, distributed radially, which are read by small PCB mount pressure sensors. The voltage signals from the pressure sensors are read into the real time controller and are integrated to solve for F, as per the algorithm outlined in Figure 2.5. The response of the mass $x(t)$ is thus calculated in real time with dynamics dictated by Equation 4.1, and the position of the linear stage moved accordingly by the stepper motor.

Two experiments are considered with the 1-DOF system in an effort to evaluate the functionality of the coupled numerical-experimental measurement architecture. The first tests the open loop response of the system by applying a step change of pressure to the pressure taps, and the second tests the coupled nature of the fluid and structure problems by placing the 1-DOF system in the uniform free stream of a wind tunnel. The measured pressures are compared to analytical solutions to the idealized flow over the plate.

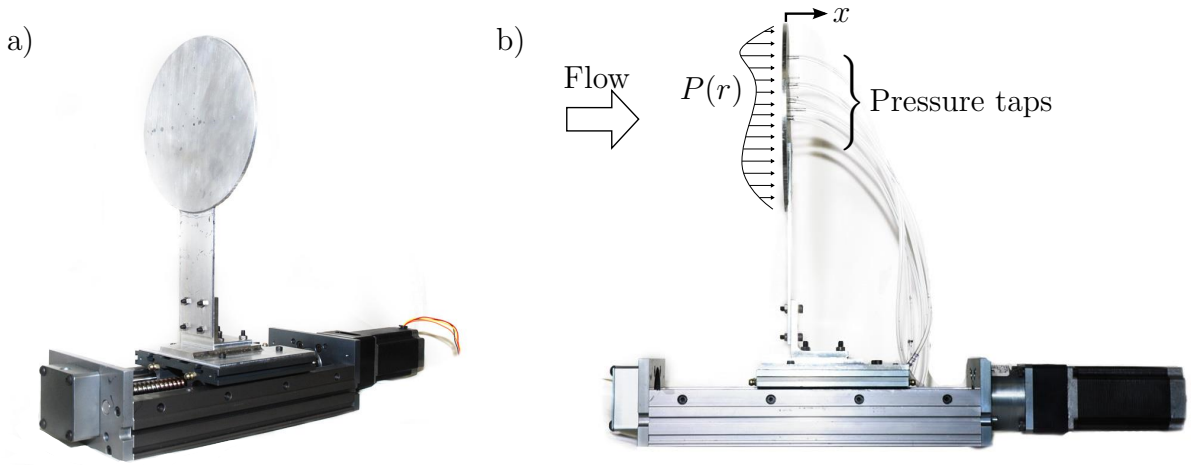

Figure 4.2: Experimental apparatus for single degree of freedom test system. a) an overview of the system with the instrumented plate mounted to the linear actuator and, b) schematic view of the apparatus with perpendicular impinging freestream.

4.1.1 Step change in applied pressure

The step response of the 1-DOF oscillator is considered to test the dynamical response to a pressure input and the ability to actuate the physical system in real time. A step change of pressure is modelled by applying a constant elevated pressure $P(r) = P_0$ to the oscillator until time $t = t_0$ and rapidly dropping the pressure to $P(r) = 0$ at time $t > t_0$.

The pressure taps of the 1-DOF apparatus shown in Figure 4.2 are connected to a single reservoir and a thin membrane is placed over the reservoir opening. Air is pumped into the reservoir until the pressure P_0 is reached. At time $t = t_0$, the membrane is ruptured and the pressure rapidly drops uniformly to $P(r) = 0$

The analytical response of the structure to a step input is solved and plotted as x_{exact}. At each time step, based on the present pressure input, the prescribed response of the system is updated by the controller; shown as x_{presc} in Figure 4.3. Excellent agreement between the analytical response and the prescribed response indicates the pressure measurement, integration, and differential equation solver of the system function effectively. As can also be noted from Figure 4.3, the actual position of the actuator, x_{act}, always lags the prescribed position, x_{presc}. This lag is a result of the open-loop control strategy used. A finite time lag is inevitable, due to the physical inertia of the system and computational delays, but must not be so great that it interferes with the fluid-structure coupling. The maximum time lag between the actual and prescribed response is approximately 0.15 seconds for

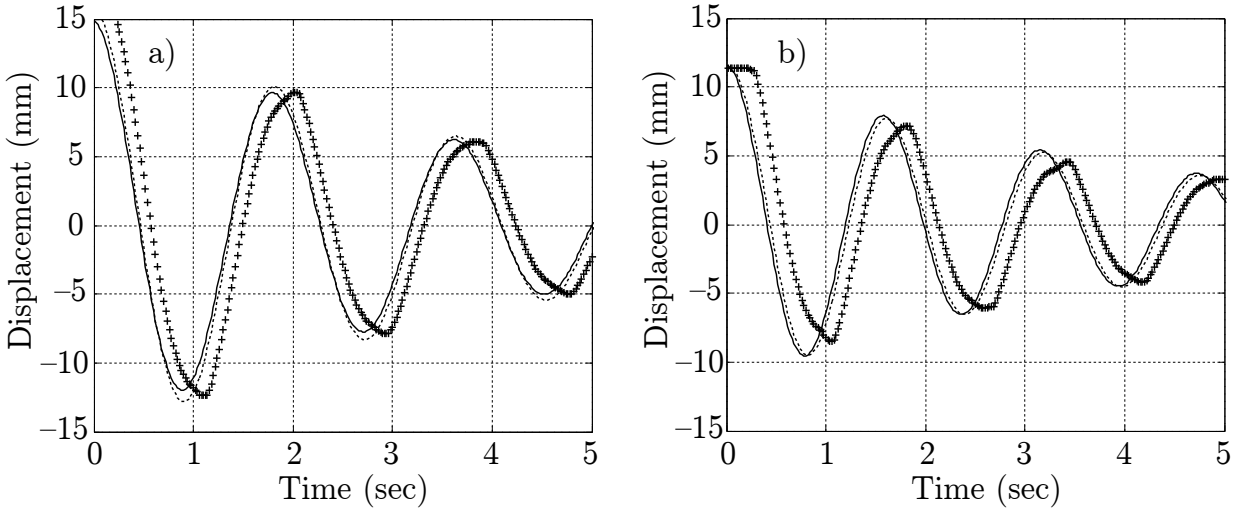

Figure 4.3: Response of 1-DOF system to a step change of pressure with system parameters a) $\omega = 2.4\ \frac{\text{rad}}{\text{s}}$, $\zeta = 0.07$, and b) $\omega = 4.0\ \frac{\text{rad}}{\text{s}}$, $\zeta = 0.07$. Analytical response of system x_{exact} —. Prescribed response x_{presc} - - -. Actual position of actuator x_{act} +.

both the $\omega = 2.4\ \frac{\text{rad}}{\text{s}}$ and $\omega = 4.0\ \frac{\text{rad}}{\text{s}}$ cases; this leads to a maximum phase lag of 20°and 30°respectively. Bearing in mind that the two test cases presented herein represent more demanding motion requirements than will be typical of the full vocal fold apparatus, the time lag is deemed acceptable.

4.1.2 Uniform freestream flow

The single degree of freedom system, shown in Figure 4.2 and with dynamics governed by Equation 4.1, is placed in an open flow wind tunnel to evaluate the system response to a perpendicular uniform freestream flow. This further tests the pressure measurement system's ability to resolve surface pressures from a flow and to use the measured pressures as inputs to the dynamical model.

Homann's analysis [53, 59] is used to solve the analytical solution to the pressure distribution on an infinite circular plate in an infinite freestream. The analysis is included in Appendix B. The resulting pressure distribution is compared to the results of wind tunnel tests at varying freestream velocities, shown in Figure 4.4a). Excellent agreement between the analytical and measured pressures is observed near the centre of the plate for $r/R < 0.2$. Moving towards the edge of the plate, the agreement between experimental and analytical

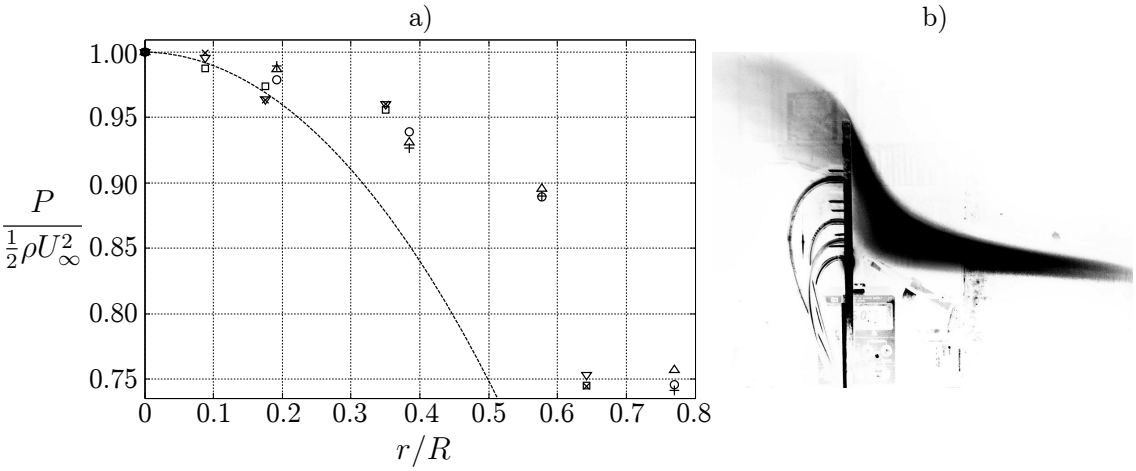

Figure 4.4: Single degree of freedom apparatus in uniform freestream. a) Comparison of measured pressure for 3 freestream velocities (each test conducted twice) against analytical solution by Homman [59] for $U_\infty = 5.8$ $\frac{\text{m}}{\text{s}}$: $\circ$, $\square$. $U_\infty = 9.8$ $\frac{\text{m}}{\text{s}}$: $\triangle$, $\triangledown$. $U_\infty = 15$ $\frac{\text{m}}{\text{s}}$: $+$, $\times$. P_{Homann}: - - -. b) Enhanced smoke flow visualization of flow over plate in wind tunnel.

pressure values decreases. As can be observed with the flow visualization of Figure 4.4b), near the centre of the plate the flow visually resembles, and is more physically similar, to the infinite idealized case. Towards the edge of the plate, the finite effects become more pronounced and the idealized flow is no longer a representative analogue.

Successful validation of the 1-DOF test system with the step response test and the wind tunnel test demonstrates the ability for a pressure feedback numerical-experimental system to model fluid-structure interactions. As a result of the open-loop control strategy, the inevitable time lag between desired and actual outputs is characterized. This result serves as a milestone to pursue the detailed design and construction of the rotational axis and vocal fold geometry, as well as design and implementation of the full vocal fold dynamic solver and collision algorithms.

4.2 Single vocal fold model with impinging jet

Having validated the controller and slide axis in Section 4.1, two more primary design challenges remain: the rotational axis assembly, and using a liquid working fluid. The rotational axis assembly, as described in Section 2.2.2.2, must be tested to ensure it meets the dynamic requirements. The addition of a liquid working fluid, rather than air used in

the tests described in Section 4.1, provides many additional complications with sealing and ensuring electronics function correctly. An experiment is proposed to test a single 2-DOF vocal fold model under pressure loading from an impinging jet.

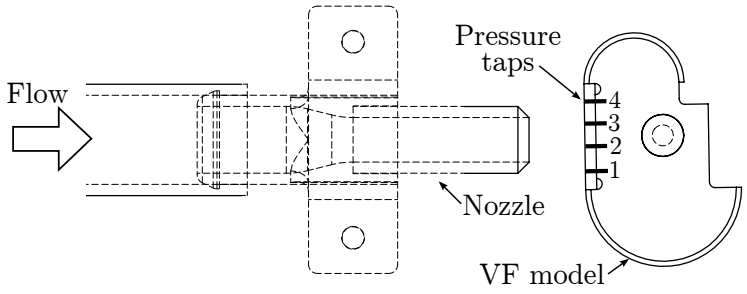

Figure 4.5: Schematic of impinging jet experimental set-up. A jet impinges on vocal fold (VF) model surface and the resulting surface pressure is read by 4 pressure taps.

A nozzle is positioned 25 mm from the rigid vocal fold model with the flow issuing perpendicular to the medial surface of the model. Flow of water is provided from a reservoir and is fed by gravity. Initially, 1 m of head pressure is available at the nozzle but the pressure falls to zero as the water level drops. Four pressure taps evenly distributed across the plate of the rigid vocal fold, as shown in Figure 2.2.4, measure the surface pressure. The response is governed by the Steinecke and Herzel dynamical model described in Section 2.3.2. The vocal fold model is actuated by both the translational and rotational motion assemblies described in Section 2.2.2.

The measured integrated pressure loading on the vocal fold model and the system response are shown in Figure 4.6. The time history of the force is given in physiological scale in Figure 4.6b). The force builds as the jet accelerates and then decreases as the level in the reservoir is depleted. The motion of the vocal fold model is shown in Figure 4.6a), where X_1 and X_2 are the inferior and superior map points respectively. As described in the inverse kinematic analysis of Section 2.3.3, the map points are experimentally scaled-up coordinates based on the positions of the two masses of the governing model.

The vocal fold model responds to the pressure loading acting on the inferior mass. The inferior mass (X_1) responds first, and the superior mass (X_2) lags. This phase lag between the inferior and superior masses is analogous to the mucosal wave of the glottis. The results of Figure 4.6 suggest that the response of the structure is being determined by the pressure field of the fluid; that is, the fluid is affecting the structure. This represents one half of the coupled fluid-structure interaction, the other being that the motion of the structure results in discernible changes in the flow.

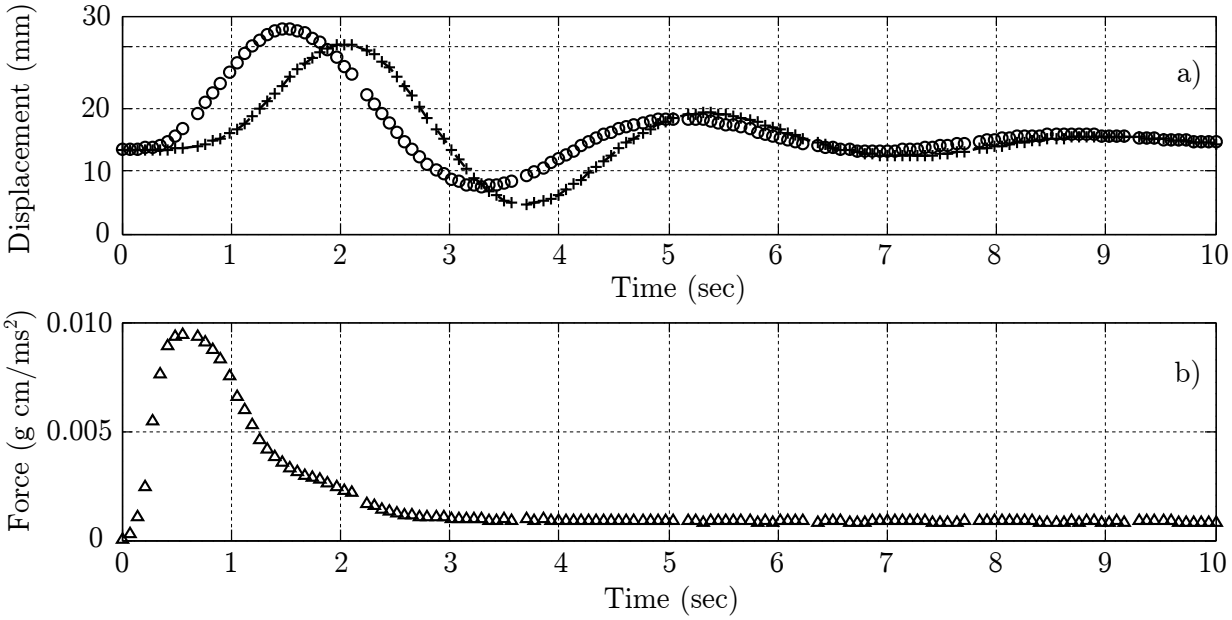

Figure 4.6: Results of impinging jet experiment for 2-DOF single vocal fold model, showing a) the actual response of the model X_1 ($\circ$) and X_2 ($\times$), and b) the integrated force ($\triangle$) measured on the medial surface as a function of time.

To test the effect of the movement of the vocal folds on the flow field, the spatial pressure distribution across the vocal fold surface is recorded as the flow develops. Figure 4.7 shows the jet flow developing and the spatial distribution of pressure at four instances through the interaction. Flow is visualized with fluorescein dye excited by a laser plane through the middle of the jet flow. The pressure measured by the four pressure stations is plotted below each corresponding instance in the flow.

As the jet begins to develop, the pressure taps near the centre of the jet begin to show increased pressure, shown in Figure 4.7a) and b). The maximum measured pressure at the stagnation point is located roughly at pressure station 2. The resulting force causes the inferior mass of the 2MM to accelerate and the vocal fold model to rotate. After the model rotates, in Figure 4.7c), the stagnation point shifts in the superior direction towards pressure tap 3 and 4. The flow visualization shows the majority of the jet flow is split in the inferior direction. Rotation continues and the model begins to translate away from the jet. The spatial pressure distribution in Figure 4.7d) shows the stagnation point is now located approximately at station 4 and the flow visualization shows a very different flow than was initially observed.

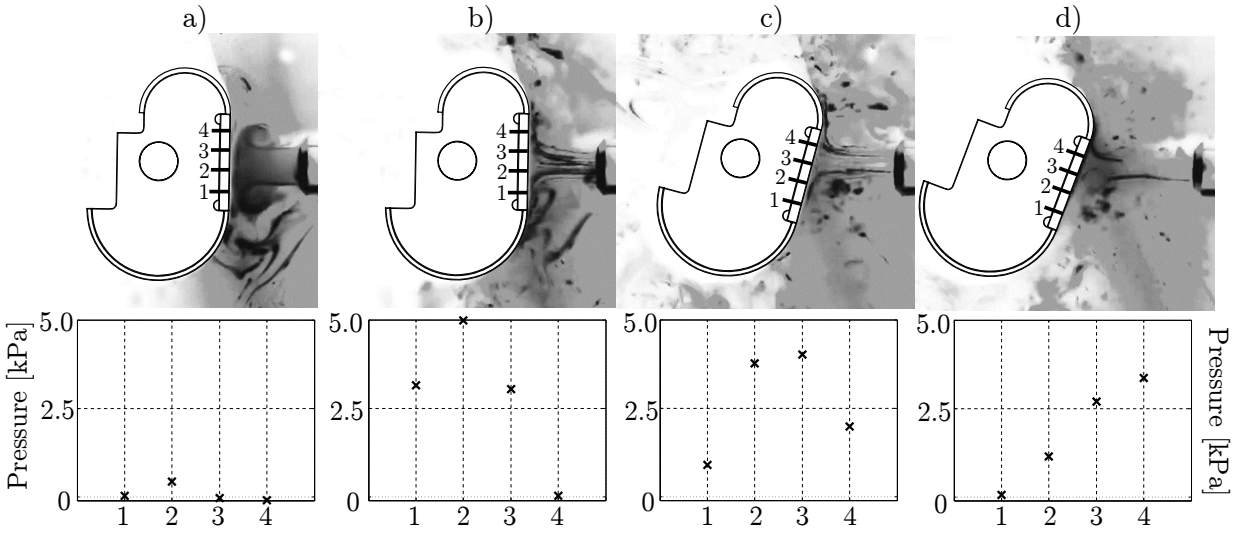

Figure 4.7: Surface pressure distribution and flow visualization for impinging jet on Vocal Fold

4.3 Static vocal fold model

The experiments performed in prior sections have demonstrated the apparatus' ability to respond to pressure loading in a physically relevant way, and that fluid-structure interactions can be captured. The last validation before performing the fully coupled experiment with the propylene glycol working fluid is to ensure the model vocal folds and the flow from the tunnel provide relevant analogues to human speech. To test this, the vocal fold models are configured in the test section of the flow tunnel in a static configuration, thus making the results comparable to the prior studies of flow through rigid vocal fold models outlined in Section 1.2.1.1.

4.3.1 Streamwise velocity variation through the glottis

The vocal fold models are configured to form a parallel glottis with a glottal gap of 10 mm (0.67 mm physiological). The inlet stacks and drain valves are set such that the flow through the glottis has a Reynolds number of $Re = \rho D_h \bar{U}/\mu = 4865$, with the hydraulic diameter of the glottal duct D_h as the characteristic length scale and the average velocity $\bar{u}$ through the glottis. LDV measurements are taken along the medial line through the glottis, starting at the entrance to the vocal folds ($x = 0$ mm) to the exit of the glottis

(x = 160 mm) at 15 mm intervals. Figure 4.8a) shows the measured velocity at each measurement station, and Figure 4.8b) shows the position of the stations relative to the vocal fold geomtry. The fluid smoothly accelerates through the glottis until it reaches the exit radii and exits as a free jet. As predicted, the velocity fluctuations within the vocal fold geometry are significantly damped as compared to those measured in the empty test section in Section 3.3. At $x = 70$ mm the velocity fluctuations $\sigma_u/\bar{u} = 2.4\%$, less than half what was measured in the empty test section.

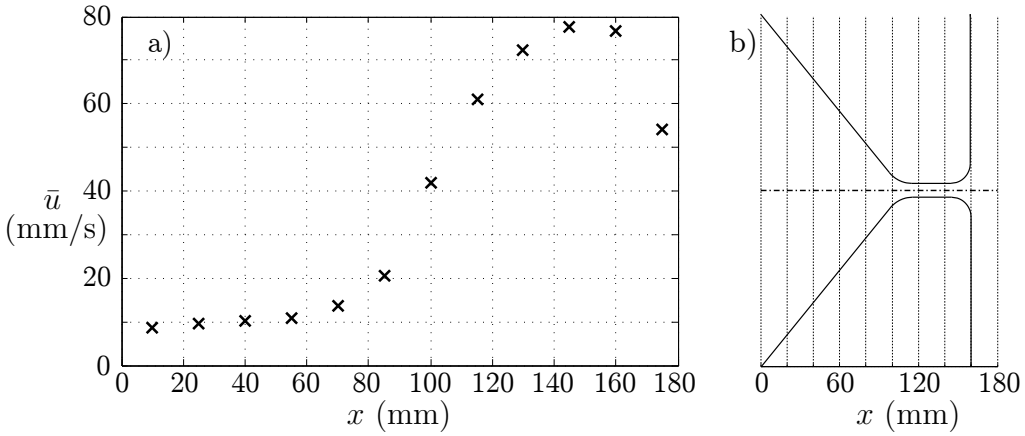

Figure 4.8: Streamwise velocity at centreline through vocal fold model with $\theta = 0°$

4.3.2 Flow through divergent glottis

As described in Section 1.1.2, the motion of the vocal folds is such that the geometry of the glottal duct transitions from a converging to diverging channel, known as a the mucosal wave. The mucosal wave has been demonstrated to be crucial in the efficient exchange of energy from the flow to the tissue. This is because in the diverging configuration, flow separation through the glottis reduces the loading on the vocal fold walls as compared to in the converging configuration. Asymmetric wall loading, the difference between the attached flow wall and the non-flow wall, has been observed in static, pulsatile, and driven experiments as well as numerical studies.

Hydrogen bubble flow visualization, with a laser sheet for illumination, is used to visualize the flow within the glottis, shown in Figure 4.9. The vocal folds are positioned to form a divergent glottis with enclosed angle $\theta = 15°$. The Reynolds number, as before, is $Re = 4865$. Flow visualization reveals separation at the minimum glottal area, shown as

S1 in Figure 4.9, and the flow attaching to the left vocal fold wall through the remainder of the glottis. The recirculation zone and slow moving flow along the right vocal fold wall are indicative of the complete separation from the right wall. The jet then separates from the left wall at the exit radius, shown as S2 in Figure 4.9, to form a free jet.

The results of Figure 4.9 are compared to the well validated simulation results of Scherer et al. [22] shown in Figure 4.10. Separation points are similarly predicted in Figure 4.10a), noting that the S1 inferior separation point is further downstream than the vocal fold model of the experimental results presented herein. This is hypothesized to be a result of the slight protrusion of the acetate sheet that forms the flexible vocal fold surface causing early separation. This can be remedied by modifying the attachment of the sheet to the rigid vocal fold surface to prevent such a disturbance to the flow.

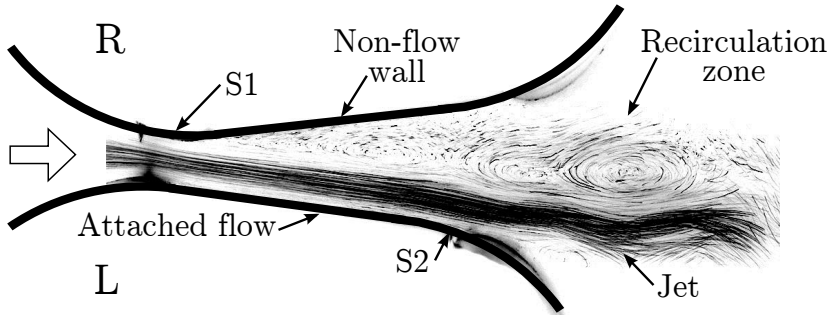

Figure 4.9: Hydrogen bubble flow visualization of flow within glottis for divergent geometry with $\theta = 15°$, noting the two separation points S1 and S2.

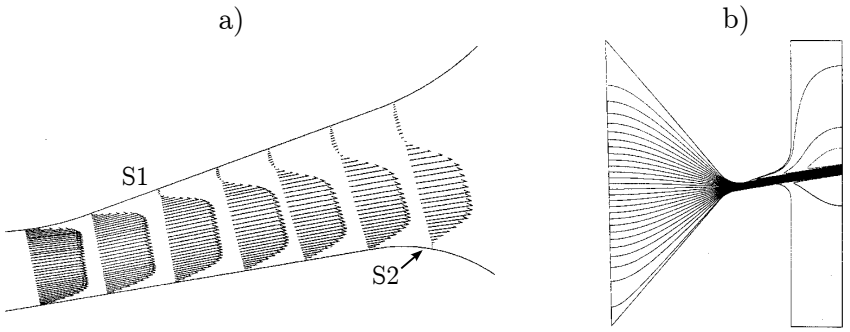

Figure 4.10: Velocity distribution of an oblique glottis with $\theta = 10°$ from simulation by Scherer et al. [22]. a) Velocity vectors of flow within the glottis and, b) streamlines of simulated flow through vocal folds.

Similar behaviour of glottal jet skewing, separation, and the presence of a recirculation zone at the non-flow wall are consistent with the static model results shown in Figure 4.10, as well as the driven model results of Erath et al. [27] shown as Figure 3.3.

4.4 Driven vocal fold model

To capture the effect of the moving walls on flow development, and to ensure the motion and controller systems are working correctly, the vocal fold models are driven with *a priori* prescribed motion. Distilled water is used as the working fluid, which results in a slower experimental scale frequency of oscillation compared to using the propylene glycol solution. A fundamental frequency of $f_{\text{phys}} = 200$ Hz is modelled, which scales to an experimental frequency of oscillation of $f_{\text{exp}} = 0.067$ Hz. A laser volume is created with two cylindrical lenses to illuminate the hydrogen bubbles as well as any small particles in the flow. The flow visualization results from the driven vocal fold model test are shown in Figure 4.11 for four instances over a single phonatory cycle; the two locations of separation S1 and S2 are indicated in each frame.

Visualization of the flow field shows significant changes in flow behaviour as the motion progresses. A cycle is defined as $t/T = 0$ being the instant the vocal folds begin to separate. When the glottis is closed in software, and the physical vocal fold models are close together, a narrow, stable, high speed jet issues from the small glottal gap separating almost symmetrically on the left and right sides. This behaviour continues through the opening phase of the motion while the glottis maintains a converging geometry. After $t/T \approx 0.45$ the medial surface of both models is parallel as the glottal duct transitions from converging to diverging. Shortly after the geometry becomes diverging, at $t/T = 0.58$, the first separation point S1 moves rapidly in the inferior direction as the jet separates from the right vocal fold wall and adheres to the left wall. At this instance, large vortices can be observed rolling up at the shear layer at the exit of the glottis. The formation of vortices in the shear layer is important to the production of speech as it has been demonstrated to correlate directly to tonal components in the radiated spectra [60].

The flow visualization is qualitatively similar to the PIV results of Erath and Plesniak, shown in Figure 3.3. Erath and Plesniak define the instance in the phonatory cycle based only on the time period the glottis is open, that is t/T_{open}. Converting the results of Figure 4.11, $t/T = 0.58$ corresponds to $t/T_{\text{open}} = 0.69$; which is almost the same instant shown in Figure 3.3b) of Erath and Plesniak's results with $t/T_{\text{open}} = 0.70$. Similar separation locations, jet skewing, and vortical structures are observed in both the PIV of Erath and

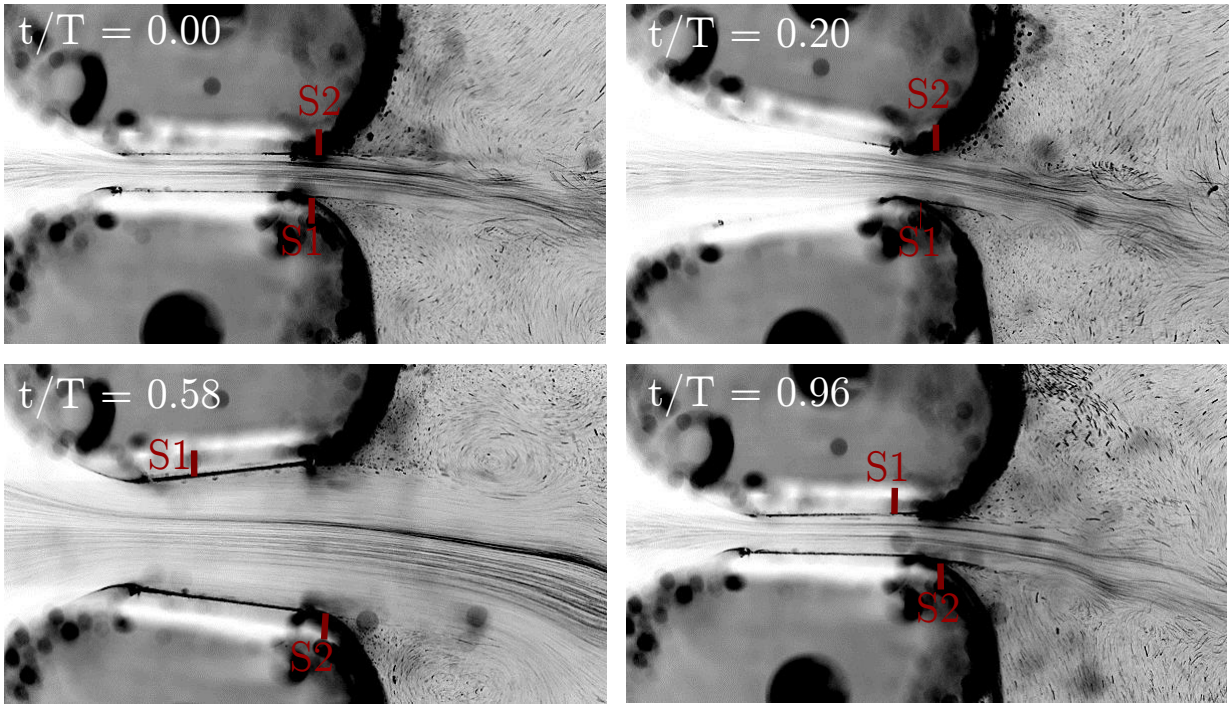

Figure 4.11: Hydrogen bubble flow visualization of flow through driven vocal fold models over a single period. The two separation points, S1 and S2, are marked in each frame. Flow is from left to right.

Plesniak and the flow visualization of the present study. In the PIV results, the glottal jet is adhered to the right wall whereas it is adhered to the left wall in the present work.

Chapter 5

Conclusions and Future Work

The previous chapter aimed to validate the facility in two ways: one, that coupled fluid-structure interactions can be accurately modelled with a pressure feedback numerical-experimental facility; two, that the geometry and flow parameters of the experimental facility can accurately model the flow through the human vocal folds. In conjunction, these two broad validations serve to support the use of this facility to model the fluid-structure interactions of the vocal folds. Difficulties encountered in the development of the facility and proposed changes to improve the operation of the facility are presented in the following sections.

5.1 Conclusions

A flow facility has been developed that utilizes real time simulation of the dynamics of the vocal fold tissue in conjunction with a representative flow field for pressure measurement. The ability to capture the fluid structure interactions and to accurately calculate and achieve the dyanamical response of the numerical model is demonstrated through simplified tests. Flow visualization of flow through the vocal folds models at physically representative Reynolds and Strouhal numbers exhibits similar qualitative flow behaviour to previous experimental and numerical studies. In conjunction, these results provide a high confidence that the fluid-structure interactions of human speech can be investigated with the facility developed herein.

Difficulties encountered in development mainly pertained to achieving a good pressurization seal inside the tunnel such that fluid does not leak out and so that consistent

subglottal pressure is maintained. Achieving a strong seal between the vocal fold models and the tunnel walls and ceiling was also difficult and results in less physically accurate pressure build-up when the vocal folds are in close contact.

5.2 Recommendations for future work

It remains to control the vocal fold dynamics directly based on the representative flow experiment to achieve fully coupled oscillations. This necessitates the use of the propylene glycol solution, with increased viscosity, to allow for sufficient pressure resolution to control the dynamics. Before proceeding with fully coupled operation with propylene glycol, the sealing systems of the tunnel and the vocal fold models should be made more robust to reduce the risk of leakage. The addition of a simple chilling system, to maintain a set-point temperature, would allow for more control over the viscosity of the working fluid and thus more flexibility.

A significant fraction of the flow was observed flowing between the vocal fold models and the test section walls and ceiling. Reduction of this flow, by increasing the flow resistance with improved sealing at these locations, would provide more physically relevant flow dynamics. This is especially important when the glottal gap is small, and the proportion of by-pass flow is significant. The addition of a compliant layer over the rigid vocal fold model assembly would allow for physical contact between the models which would provide higher flow resistance and therefore more accurate build-up of subglottal pressure.

The addition of absolute encoder feedback to both the translational and rotational motion axes would be extremely useful in offering more accurate control of the vocal folds. It is recommended that absolute position feedback be incorporated to reduce the errors inherent to manually zeroing the vocal fold positions before a run. It was found to be difficult to provide a reliable datum to reference the positions of the physical model to allow for programming the initial positions in the software.

For modelling coupled self-oscillation, with propylene glycol as the working fluid, it is recommended that more accurate measurements be taken to quantify the flow field. Particle image velocimetry (PIV) would offer detailed spatial and temporal resolution. In conjunction with the wall surface pressure measurements, the velocity data from PIV would give an invaluable tool in understanding the physics of the fluid-structure interactions of speech. These data would also be extremely useful in validating past and future numerical models of the flow through the vocal folds.

References

[1] N. Roy, R. M. Merrill, S. D. Gray, and E. M. Smith, "Voice disorders in the general population: prevalence, risk factors, and occupational impact," *The Laryngoscope*, vol. 115, no. 11, pp. 1988–1995, 2005.

[2] B. D. Erath, M. Zañartu, K. C. Stewart, M. W. Plesniak, D. E. Sommer, and S. D. Peterson, "A review of lumped-element models of voiced speech," *Speech Communication*, vol. 55, no. 5, pp. 667–690, 2013.

[3] R. Mittal, B. D. Erath, and M. W. Plesniak, "Fluid dynamics of human phonation and speech," *Annual Review of Fluid Mechanics*, vol. 45, pp. 437–467, 2013.

[4] J. Van den Berg, "Myoelastic-aerodynamic theory of voice production," *Journal of Speech, Language, and Hearing Research*, vol. 1, no. 3, pp. 227–244, 1958.

[5] S. L. Thomson, L. Mongeau, and S. H. Frankel, "Aerodynamic transfer of energy to the vocal folds," *The Journal of the Acoustical Society of America*, vol. 118, no. 3, pp. 1689–1700, 2005.

[6] M. Hirano, "Phonosurgery: basic and clinical investigations," *Otologia (Fukuoka)*, vol. 21, no. suppl 1, pp. 239–260, 1975.

[7] I. R. Titze, "Principles of voice production," 1994.

[8] C. Tao and J. J. Jiang, "Chaotic component obscured by strong periodicity in voice production system," *Physical Review E*, vol. 77, no. 6, p. 061922, 2008.

[9] B. D. Erath, M. Zaartu, S. D. Peterson, and M. W. Plesniak, "Nonlinear vocal fold dynamics resulting from asymmetric fluid loading on a two-mass model of speech," *Chaos: An Interdisciplinary Journal of Nonlinear Science*, vol. 21, no. 3, pp. –, 2011.

[10] D. A. Berry, D. W. Montequin, and N. Tayama, "High-speed digital imaging of the medial surface of the vocal folds," *The Journal of the Acoustical Society of America*, vol. 110, no. 5, pp. 2539–2547, 2001.

[11] Q. Xue, X. Zheng, R. Mittal, and S. Bielamowicz, "Subject-specific computational modeling of human phonation," *The Journal of the Acoustical Society of America*, vol. 135, no. 3, pp. 1445–1456, 2014.

[12] B. D. Erath, S. D. Peterson, M. Zañartu, G. R. Wodicka, and M. W. Plesniak, "A theoretical model of the pressure field arising from asymmetric intraglottal flows applied to a two-mass model of the vocal folds," *The Journal of the Acoustical Society of America*, vol. 130, no. 1, pp. 389–403, 2011.

[13] S. L. Thomson, "Fluid-structure interactions within the human larynx," 2004.

[14] R. L. Miller, "Nature of the vocal cord wave," *The Journal of the Acoustical Society of America*, vol. 31, no. 6, pp. 667–677, 1959.

[15] M. Döllinger, D. A. Berry, and G. S. Berke, "Medial surface dynamics of an in vivo canine vocal fold during phonation," *The Journal of the Acoustical Society of America*, vol. 117, no. 5, pp. 3174–3183, 2005.

[16] A. Chan, L. Mongeau, and K. Kost, "Vocal fold vibration measurements using laser doppler vibrometry," *The Journal of the Acoustical Society of America*, vol. 133, no. 3, pp. 1667–1676, 2013.

[17] D. E. Sommer, I. T. Tokuda, S. D. Peterson, K.-I. Sakakibara, H. Imagawa, A. Yamauchi, T. Nito, T. Yamasoba, and N. Tayama, "Estimation of inferior-superior vocal fold kinematics from high-speed stereo endoscopic data in vivo," *Journal of the Acoustical Society of America*, vol. 136, no. 6, 2014.

[18] J. Van den Berg, J. Zantema, and P. Doornenbal Jr, "On the air resistance and the bernoulli effect of the human larynx," *The Journal of the Acoustical Society of America*, vol. 29, no. 5, pp. 626–631, 1957.

[19] R. Wegel, "Theory of vibration of the larynx," *Bell System Technical Journal, The*, vol. 9, pp. 207–227, Jan 1930.

[20] K. Ishizaka and M. Matsudaira, *Fluid mechanical considerations of vocal cord vibration*. Spech Communications Research Laboratory, 1972.

[21] R. C. Scherer, I. R. Titze, and J. F. Curtis, "Pressure-flow relationships in two models of the larynx having rectangular glottal shapes," *The Journal of the Acoustical Society of America*, vol. 73, no. 2, pp. 668–676, 1983.

[22] R. C. Scherer, D. Shinwari, K. J. De Witt, C. Zhang, B. R. Kucinschi, and A. A. Afjeh, "Intraglottal pressure profiles for a symmetric and oblique glottis with a divergence angle of 10 degrees," *The Journal of the Acoustical Society of America*, vol. 109, no. 4, pp. 1616–1630, 2001.

[23] A. Hirschberg, X. Pelorson, G. Hofmans, R. VAN HASSEL, and A. Wijnands, "Starting transient of the flow through an in-vitro model of the vocal folds," *Les Cahiers de l'ICP. Bulletin de la communication parlée*, no. 5, pp. 3–14, 1996.

[24] G. C. J. Hofmans, G. Groot, M. Ranucci, G. Graziani, and A. Hirschberg, "Unsteady flow through in-vitro models of the glottis," *The Journal of the Acoustical Society of America*, vol. 113, no. 3, pp. 1658–1675, 2003.

[25] B. D. Erath and M. W. Plesniak, "The occurrence of the coanda effect in pulsatile flow through static models of the human vocal folds," *The Journal of the Acoustical Society of America*, vol. 120, no. 2, pp. 1000–1011, 2006.

[26] L. Mongeau, N. Franchek, C. H. Coker, and R. A. Kubli, "Characteristics of a pulsating jet through a small modulated orifice, with application to voice production," *The Journal of the Acoustical Society of America*, vol. 102, no. 2, pp. 1121–1133, 1997.

[27] B. D. Erath and M. W. Plesniak, "An investigation of asymmetric flow features in a scaled-up driven model of the human vocal folds," *Experiments in Fluids*, vol. 49, no. 1, pp. 131–146, 2010.

[28] M. Triep, C. Brücker, and W. Schröder, "High-speed piv measurements of the flow downstream of a dynamic mechanical model of the human vocal folds," *Experiments in Fluids*, vol. 39, no. 2, pp. 232–245, 2005.

[29] J. S. Drechsel and S. L. Thomson, "Influence of supraglottal structures on the glottal jet exiting a two-layer synthetic, self-oscillating vocal fold model," *The Journal of the Acoustical Society of America*, vol. 123, no. 6, pp. 4434–4445, 2008.

[30] J. Neubauer, Z. Zhang, R. Miraghaie, and D. A. Berry, "Coherent structures of the near field flow in a self-oscillating physical model of the vocal folds," *The Journal of the Acoustical Society of America*, vol. 121, no. 2, pp. 1102–1118, 2007.

[31] K. Ishizaka and J. L. Flanagan, "Synthesis of voiced sounds from a two-mass model of the vocal cords," *Bell system technical journal*, vol. 51, no. 6, pp. 1233–1268, 1972.

[32] R. Schwarz, M. Döllinger, T. Wurzbacher, U. Eysholdt, and J. Lohscheller, "Spatio-temporal quantification of vocal fold vibrations using high-speed videoendoscopy and a biomechanical model," *The Journal of the Acoustical Society of America*, vol. 123, no. 5, pp. 2717–2732, 2008.

[33] D. Wong, M. R. Ito, N. B. Cox, and I. R. Titze, "Observation of perturbations in a lumped-element model of the vocal folds with application to some pathological cases," *The Journal of the Acoustical Society of America*, vol. 89, no. 1, pp. 383–394, 1991.

[34] I. T. Tokuda, M. Zemke, M. Kob, and H. Herzel, "Biomechanical modeling of register transitions and the role of vocal tract resonatorsa)," *The Journal of the Acoustical Society of America*, vol. 127, no. 3, pp. 1528–1536, 2010.

[35] I. Steinecke and H. Herzel, "Bifurcations in an asymmetric vocal-fold model," *The Journal of the Acoustical Society of America*, 1995.

[36] D. E. Sommer, B. D. Erath, M. Zañartu, and S. D. Peterson, "The impact of glottal area discontinuities on block-type vocal fold models with asymmetric tissue properties," *The Journal of the Acoustical Society of America*, vol. 133, no. 3, pp. EL214–EL220, 2013.

[37] J. Liljencrants, "A translating and rotating mass model of the vocal folds," *STL-QPSR*, vol. 32, no. 1, pp. 1–18, 1991.

[38] I. R. Titze and B. H. Story, "Rules for controlling low-dimensional vocal fold models with muscle activation," *The Journal of the Acoustical Society of America*, vol. 112, no. 3, pp. 1064–1076, 2002.

[39] G. C. J. Hofmans, G. Groot, M. Ranucci, G. Graziani, and A. Hirschberg, "Unsteady flow through in-vitro models of the glottis," *The Journal of the Acoustical Society of America*, vol. 113, no. 3, pp. 1658–1675, 2003.

[40] H. Schlichting, K. Gersten, and K. Gersten, *Boundary-layer theory*. Springer, 2000.

[41] M. P. Paıdoussis, S. J. Price, and E. de Langre, "Fluid-structure interactions: Cross flow induced instabilities," 2011.

[42] C. Williamson and R. Govardhan, "Vortex-induced vibrations," *Annu. Rev. Fluid Mech.*, vol. 36, pp. 413–455, 2004.

[43] F. Hover, S. Miller, and M. Triantafyllou, "Vortex-induced vibration of marine cables: experiments using force feedback," *Journal of fluids and structures*, vol. 11, no. 3, pp. 307–326, 1997.

[44] A. W. Mackowski and C. H. Williamson, "Developing a cyber-physical fluid dynamics facility for fluid–structure interaction studies," *Journal of Fluids and Structures*, vol. 27, no. 5, pp. 748–757, 2011.

[45] A. Mackowski and C. Williamson, "An experimental investigation of vortex-induced vibration with nonlinear restoring forces," *Physics of Fluids*, vol. 25, no. 8, p. 087101, 2013.

[46] G. O. Curme, *Glycols*, vol. 114. Reinhold, 1952.

[47] D. E. Sommer, B. D. Erath, M. Zanartu, and S. D. Peterson, "Corrected contact dynamics for the Steinecke and Herzel asymmetric two-mass model of the vocal folds," *The Journal of the Acoustical Society of America*, vol. 132, no. 4, pp. EL271–EL276, 2012.

[48] L. P. Fulcher, R. C. Scherer, and T. Powell, "Pressure distributions in a static physical model of the uniform glottis: Entrance and exit coefficients," *The Journal of the Acoustical Society of America*, vol. 129, no. 3, pp. 1548–1553, 2011.

[49] J. H. Bell and R. D. Mehta, "Design and calibration of the mixing layer and wind tunnel," 1989.

[50] P. Bradshaw and R. Pankhurst, "The design of low-speed wind tunnels," *Progress in Aerospace Sciences*, vol. 5, pp. 1–69, 1964.

[51] J. L. Lumley and J. McMahon, "Reducing water tunnel turbulence by means of a honeycomb," *Journal of Fluids Engineering*, vol. 89, no. 4, pp. 764–770, 1967.

[52] J. Lumley, "Passage of a turbulent stream through honeycomb of large length-to-diameter ratio," *Journal of Fluids Engineering*, vol. 86, no. 2, pp. 218–220, 1964.

[53] F. M. White and I. Corfield, *Viscous fluid flow*. McGraw-Hill New York, 3rd ed., 1991.

[54] J. Scheiman, "Considerations for the installation of honeycomb and screens to reduce wind-tunnel turbulence," vol. 81868, 1981.

[55] T. Morel, "Comprehensive design of axisymmetric wind tunnel contractions," *Journal of Fluids Engineering*, vol. 97, no. 2, pp. 225–233, 1975.

[56] J. H. Bell and R. D. Mehta, "Contraction design for small low-speed wind tunnels," *NASA STI/Recon Technical Report N*, vol. 89, p. 13753, Aug. 1988.

[57] R. H. Bartels, J. C. Beatty, and B. A. Barsky, *An introduction to splines for use in computer graphics and geometric modeling*. Morgan Kaufmann, 1987.

[58] F. M. White, *Fluid Mechanics*. McGraw-Hill, 2008.

[59] F. Homann, "Der einfluss grosser zähigkeit bei der strömung um den zylinder und um die kugel," *ZAMM-Journal of Applied Mathematics and Mechanics/Zeitschrift für Angewandte Mathematik und Mechanik*, vol. 16, no. 3, pp. 153–164, 1936.

[60] J. Suh and S. H. Frankel, "Numerical simulation of turbulence transition and sound radiation for flow through a rigid glottal model," *The Journal of the Acoustical Society of America*, vol. 121, no. 6, pp. 3728–3739, 2007.

Appendix A

Deformation of tunnel ceiling

A simple analysis is performed to estimate the order of magnitude deflection of the 1/4 inch acrylic sheet used as a ceiling for the tunnel. The material properties of acrylic sheet are taken as

$$E = 3.2 \text{ GPa} \tag{A.1}$$

$$\nu = 0.35 \tag{A.2}$$

$$\sigma_{\text{UTS}} = 70 \text{ MPa} \tag{A.3}$$

and the applied load, based on the maximum pressure loading inside the tunnel, is a uniformly distributed load of $q = 7.5$ kPa. The material thickness is $H = 2h = 0.25$ in $=$ 6.35 mm

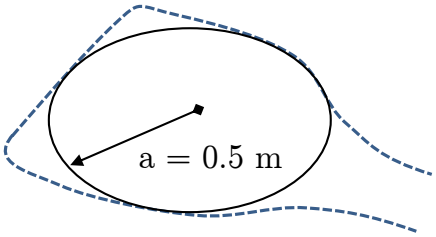

Figure A.1: Schematic of clamped circular plate used in analysis.

The plate is assumed to be circular with radius $a = 1$ m, based on the gentle curvature of the tunnel contraction as shown in Figure A.1, and clamped uniformly on all sides. This allows the problem to be treated as a Kirchoff-Love plate, with governing equation

$$\nabla^2\nabla^2 w = -\frac{q}{D} \tag{A.4}$$

where $w(r)$ is the vertical displacement of the plate at any radial location, and D is the bending stiffness defined as

$$D = \frac{2Eh^3}{3(1-\nu^2)} \tag{A.5}$$

Direct integration and applying the boundary conditions of clamped edges yielding

$$w(r) = -\frac{q}{64D}(a^2 - r^2)^2 \tag{A.6}$$

The deformation $w(r)$ is shown in Figure A.2.

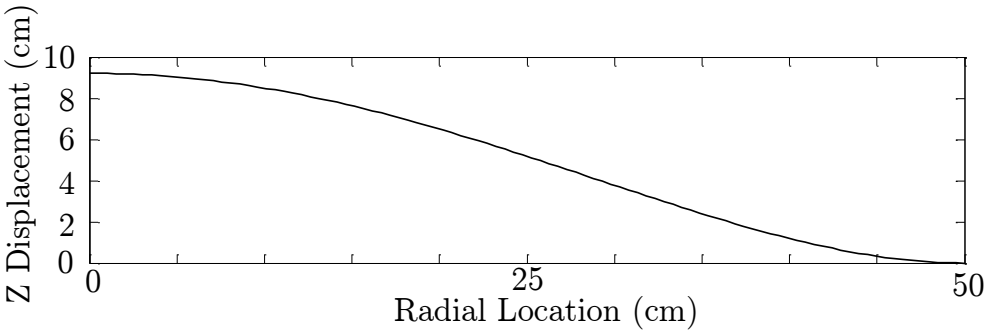

Figure A.2: Deformation of circular plate..

Similarly the in-plane stresses throughout the plate σ_{rr} and $\sigma_{\theta\theta}$ can be found with

$$\sigma_{rr} = \frac{3qz}{32h^3}\left((1+\nu)\,a^2 - (3+\nu)\,r^2\right) \tag{A.7}$$

$$\sigma_{\theta\theta} = \frac{3qz}{32h^3}\left((1+\nu)\,a^2 - (1+3\nu)\,r^2\right) \tag{A.8}$$

The results of σ_{rr} and $\sigma_{\theta\theta}$ are plotted in Figure A.3.

The highest observed stress is found at $r = 0.5$ m and is equal to $\sigma_{rr} = 34$MPa. This is 48.5% of the ultimate tensile strength of the material and suggests that additional bracing is certainly required to take the load of the internal pressure of the tunnel.

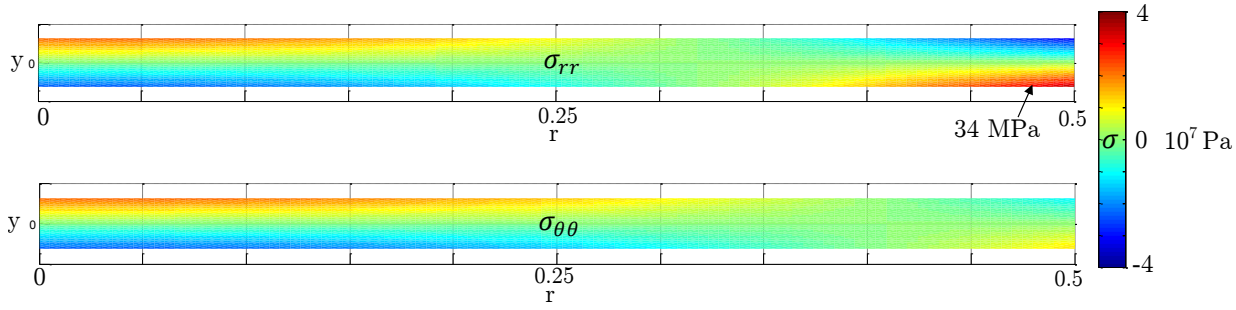

Figure A.3: Internal in-plane stress distribution calculated in plate.

Appendix B

Homann flow analysis

For a potential axisymmetric stagnation flow, the radial velocity v_r, axial velocity v_z, and potential function ψ can be defined as

$$v_r = \frac{Ur}{a} \tag{B.1}$$

$$v_z = \frac{2Uz}{a} \tag{B.2}$$

$$\psi = -\frac{U}{a} r^2 z \tag{B.3}$$

where U is the freestream velocity and a is some characteristic length of the body [53]. The potential flow, by definition, cannot capture the viscous effects near the wall. The similarity analysis pioneered by Hiemenz and Homann is followed in pursuit of a viscous flow solution [40, 53, 59]. Continuity for the axisymmetric flow is given by

$$\frac{\partial v_z}{\partial z} + \frac{1}{r}\frac{\partial (r v_r)}{\partial r} = 0 \tag{B.4}$$

and conservation of radial and axial momentum are given, respectively, by

$$(V \cdot \nabla) v_r = -\frac{1}{\rho}\frac{\partial p}{\partial r} + \nu \left(\nabla^2 v_r - \frac{v_r}{r^2} \right) \tag{B.5}$$

$$(V \cdot \nabla) v_z = -\frac{1}{\rho}\frac{\partial p}{\partial z} + \nu \nabla^2 v_z \tag{B.6}$$

Based on the form of the potential flow velocities of Equation B.1 and Equation B.2, the axial velocity will vary as a function of z, such that

$$v_r = rf'(z) \tag{B.7}$$
$$v_z = -2f(z) \tag{B.8}$$
$$\psi = -r^2 f(z) \tag{B.9}$$

The radial velocity v_r is found by substituting v_z into the continuity equation of Equation B.4 and integrating. This ensures that continuity is inherently satisfied by the velocity components. Substituting the expressions for v_r and v_z into the momentum equations of Equation B.5 and Equation B.6 gives

$$(f')^2 r - 2ff''r = -\frac{1}{\rho}\frac{\partial p}{\partial r} + \nu f'''r \tag{B.10}$$
$$4ff' = -\frac{1}{\rho}\frac{\partial p}{\partial z} - 2\nu f'' \tag{B.11}$$

The modified momentum equations are only in terms of r and the unknown function f and its derivatives. Integrating Equation B.10 with respect to z gives

$$\frac{1}{\rho}P = 2f^2 + 2\nu f' + g(r) \tag{B.12}$$
$$\frac{1}{\rho}\frac{\partial P}{\partial r} = \frac{\partial g}{\partial r} \tag{B.13}$$

Since the pressure gradient $\partial P/\partial z = f(z)$ only, Equation B.13 can be used with the modified radial momentum equation to solve for the unknown function $g(r)$.

$$\frac{1}{r\rho}\frac{\partial P}{\partial r} = \frac{1}{r}\frac{\partial g}{\partial r} = (f')^2 - 2ff'' - \nu f''' = \text{const} \tag{B.14}$$

This result is important because it shows that the radial pressure gradient only varies as some linear function of r. The constant can be solved by, noting from the potential flow, $f''' = f'' = 0$ and $f' = U/a$. Substitution of these values shows the constant to be equal to U/a.

Finally, the pressure distribution can be found to be

$$\frac{P - P_0}{\rho} = -2f^2 - 2\nu f' - \frac{U^2}{2a^2}r^2 \tag{B.15}$$

All that remains is to evaluate the function f over the domain of interest. To do this, the similarity variables

$$\eta = y\sqrt{\frac{U}{a\nu}} \tag{B.16}$$

$$F(\eta) = f\sqrt{\frac{a}{U\nu}} \tag{B.17}$$

are introduced and substituted into the modified radial momentum equation, Equation B.10. The governing equation relating the similarity variables is then found to be

$$F''' + 2FF'' - F'^2 + 1 = 0 \tag{B.18}$$

This 3rd order ordinary differential equation is solved numerically as the two nonlinear terms of Equation B.18 inhibit analytical treatment. The boundary conditions of the system are $F(0) = F'(0) = 0$ and $F'(\eta \to \infty) \to 1$. The boundary condition for F captures the no-through flow condition at the wall, and the boundary condition for F' captures the no-slip condition at the surface. The assumption for F' is that the flow far from the wall should asymptotically approach U in the far field. A value for $F''(0) = 1.3119$ is found by an iterative shooting method [53].

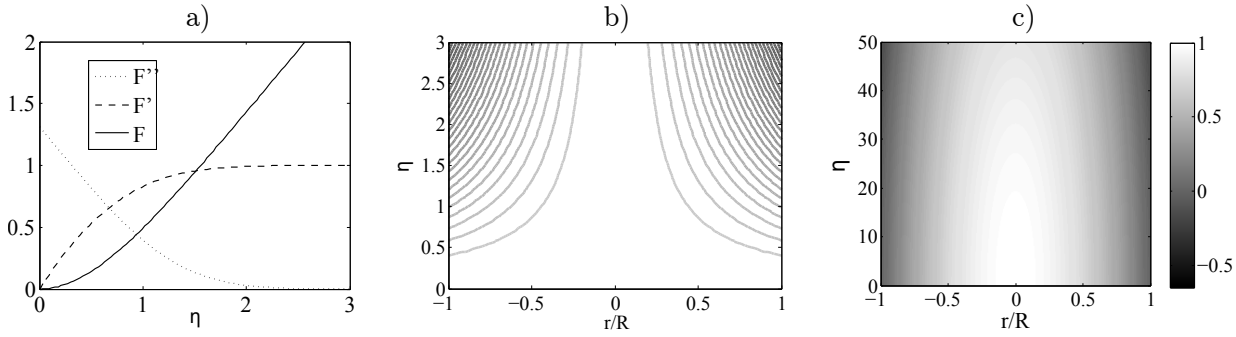

Figure B.1: Homann flow solution. a) Numerical integration to solve for Equation B.18, b) Streamlines of viscous flow plotted from Equation B.9, and c) pressure distribution of solved flow from Equation B.15.

Appendix C

Dynamical equation solver code

```
%Experimental facility parameters
scale = 15;
rho_m = 995;
mu_m = 5e-3;
cm2mm = 10; %constant for conversion
%Air properties (for physiological scale)
rho_ph = 1.2;
mu_ph = 1.98e-5;
%Calculate scaling factors to move between phys. and exp.
tscale = (rho_m/rho_ph)*(mu_ph/mu_m)*(scale)^2
pscale = (rho_ph/rho_m)*(mu_m/mu_ph)^2*(1/scale)^2
%2MM solver parameters
dt = 0.05;   %exp. time scale dt
dtph = 1000*dt/tscale; %phys time scale dt
t = [0:dt:10];
%2MM Parameters
Z=1;   % asymmetry factor
Ps = 0.015; %subglottal pressure

%Load Constants of 2MM
[m1_R, m1_L,m2_R,m2_L,k1_R, k1_L,k2_R,k2_L,kc_R,kc_L,d1,d2,rho,r1,r2,P2,
   P0,c1_R,c1_L,c2_R,c2_L,a01,a02,l,x0] = Constants(Z);

%Set ICs of 2MM (as per SH95)
x1lph_p = 0.1;
x2lph_p = 0;
x1rph_p = 0.1;
x2rph_p = 0;
v1lph_p = 0.0;
```

```
v2lph_p = 0;
v1rph_p = 0.0;
v2rph_p = 0;

%Exp scale ICs
x1l_p = 0.1*cm2mm*scale;
x2l_p = 0*cm2mm*scale;
x1r_p = 0.1*cm2mm*scale;
x2r_p = 0*cm2mm*scale;
v1l_p = 0;
v2l_p = 0;
v1r_p = 0;
v2r_p = 0;

%Inverse kinematic (IK) algorithm solver parameters
sL0 = 32.074;
sR0 = 32.074;
thetaL0 =  0.5668;
thetaR0 = -0.5668;

%Set previous slide position as guess for IK solver
sL(1) = sL0;
sR(1) = sR0;
thetaL(1) = thetaL0;
thetaR(1) = thetaR0;

%Newton-Raphson solver parameters
relax = 3;
coltol = 4;
safe = 16;

%Begin Real-time loop for simulation
for i = 2:length(t)
%Solve invisid aerodynamic loading (when not using experimental inputs)
[F_L,F_R]=BernLoading(x1rph_p,x2rph_p,x1lph_p,x2lph_p,a01,a02,Ps,d1,d2,l)
    ;

%2MM Area calculation (for collision model and comparison to SH95)
a1R = a01/2+l*x1rph_p; a1L = a01/2+l*x1lph_p;
a2R = a02/2+l*x2rph_p; a2L = a02/2+l*x2lph_p;
a1 = a1R+a1L; a2 = a2R+a2L;



% RK4 Solution
```

```
y1 = [x1rph_p,v1rph_p,x2rph_p,v2rph_p,x1lph_p,v1lph_p,x2lph_p,v2lph_p]';
x=y1;
F(1,1) = x(2);
F(2,1) = (F_R - r1*x(2)-k1_R*x(1)-theta(-a1,a01)*(c1_R*((1/(Z+1))*(x(5)+x
    (1)+a01/l)))-kc_R*(x(1)-x(3)))/m1_R;
F(3,1) = x(4);
F(4,1) = (-k2_R*x(3)-r2*x(4)-theta(-a2,a02)*(c2_R*((1/(Z+1))*(x(3)+x(7)+
    a02/l)))-kc_R*(x(3)-x(1)))/m2_R;
F(5,1) = x(6);
F(6,1) = (F_L - r1*x(6)-k1_L*x(5)-theta(-a1,a01)*(c1_L*((Z/(Z+1))*(x(5)+x
    (1)+a01/l)))-kc_L*(x(5)-x(7)))/m1_L;
F(7,1) = x(8);
F(8,1) = (-k2_L*x(7)-r2*x(8)-theta(-a2,a02)*(c2_R*((Z/(Z+1))*(x(3)+x(7)+
    a02/l)))-kc_L*(x(7)-x(5)))/m2_L;

y2 = y1+0.5*dtph*F(:,1);
x=y2;
F(1,2) = x(2);
F(2,2) = (F_R - r1*x(2)-k1_R*x(1)-theta(-a1,a01)*(c1_R*((1/(Z+1))*(x(5)+x
    (1)+a01/l)))-kc_R*(x(1)-x(3)))/m1_R;
F(3,2) = x(4);
F(4,2) = (-k2_R*x(3)-r2*x(4)-theta(-a2,a02)*(c2_R*((1/(Z+1))*(x(3)+x(7)+
    a02/l)))-kc_R*(x(3)-x(1)))/m2_R;
F(5,2) = x(6);
F(6,2) = (F_L - r1*x(6)-k1_L*x(5)-theta(-a1,a01)*(c1_L*((Z/(Z+1))*(x(5)+x
    (1)+a01/l)))-kc_L*(x(5)-x(7)))/m1_L;
F(7,2) = x(8);
F(8,2) = (-k2_L*x(7)-r2*x(8)-theta(-a2,a02)*(c2_R*((Z/(Z+1))*(x(3)+x(7)+
    a02/l)))-kc_L*(x(7)-x(5)))/m2_L;

y3 = y1+0.5*dtph*F(:,2);
x=y3;
F(1,3) = x(2);
F(2,3) = (F_R - r1*x(2)-k1_R*x(1)-theta(-a1,a01)*(c1_R*((1/(Z+1))*(x(5)+x
    (1)+a01/l)))-kc_R*(x(1)-x(3)))/m1_R;
F(3,3) = x(4);
F(4,3) = (-k2_R*x(3)-r2*x(4)-theta(-a2,a02)*(c2_R*((1/(Z+1))*(x(3)+x(7)+
    a02/l)))-kc_R*(x(3)-x(1)))/m2_R;
F(5,3) = x(6);
F(6,3) = (F_L - r1*x(6)-k1_L*x(5)-theta(-a1,a01)*(c1_L*((Z/(Z+1))*(x(5)+x
    (1)+a01/l)))-kc_L*(x(5)-x(7)))/m1_L;
F(7,3) = x(8);
F(8,3) = (-k2_L*x(7)-r2*x(8)-theta(-a2,a02)*(c2_R*((Z/(Z+1))*(x(3)+x(7)+
    a02/l)))-kc_L*(x(7)-x(5)))/m2_L;
```

```
y4 = y1+dtph*F(:,3);
x=y4;
F(1,4) = x(2);
F(2,4) = (F_R - r1*x(2)-k1_R*x(1)-theta(-a1,a01)*(c1_R*((1/(Z+1))*(x(5)+x
    (1)+a01/l)))-kc_R*(x(1)-x(3)))/m1_R;
F(3,4) = x(4);
F(4,4) = (-k2_R*x(3)-r2*x(4)-theta(-a2,a02)*(c2_R*((1/(Z+1))*(x(3)+x(7)+
    a02/l)))-kc_R*(x(3)-x(1)))/m2_R;
F(5,4) = x(6);
F(6,4) = (F_L - r1*x(6)-k1_L*x(5)-theta(-a1,a01)*(c1_L*((Z/(Z+1))*(x(5)+x
    (1)+a01/l)))-kc_L*(x(5)-x(7)))/m1_L;
F(7,4) = x(8);
F(8,4) = (-k2_L*x(7)-r2*x(8)-theta(-a2,a02)*(c2_R*((Z/(Z+1))*(x(3)+x(7)+
    a02/l)))-kc_L*(x(7)-x(5)))/m2_L;

Y = y1 + (dtph/6)*(F(:,1) + 2*F(:,2) + 2*F(:,3) + F(:,4));

%Load physiological response from RK4 solution
x1rph = Y(1);
v1rph = Y(2);
x2rph = Y(3);
v2rph = Y(4);
x1lph = Y(5);
v1lph = Y(6);
x2lph = Y(7);
v2lph = Y(8);


%Scale up to exp. values
x1l = -(x1lph+a01/(2*l))*cm2mm*scale;
x2l = -(x2lph+a02/(2*l))*cm2mm*scale;
x1r = (x1rph+a01/(2*l))*cm2mm*scale;
x2r = (x2rph+a02/(2*l))*cm2mm*scale;
v1r = 1000*v1rph*cm2mm*scale/tscale;
v2r = 1000*v2rph*cm2mm*scale/tscale;
v1l = -1000*v1lph*cm2mm*scale/tscale;
v2l = -1000*v2lph*cm2mm*scale/tscale;

%Run collision algorithm on inferior masses
[x1l_s(i),x1r_s(i)] =  VFcol_f(x1l,v1l,x1r,v1r,coltol,safe,dt);
%Run collision algorithm on superior masses
[x2l_s(i),x2r_s(i)] =  VFcol_f(x2l,v2l,x2r,v2r,coltol,safe,dt);

%Solve inverse kinematics for motor outputs
[sL(i),sR(i),thetaL(i),thetaR(i)] = VFinvkin(x1l_s(i),x2l_s(i),x1r_s(i),
```

```
    x2r_s(i),sL0,sR0,relax);

%Save previous values of 2MM solution
%to pass to next iteration
x1lph_p = x1lph;
x2lph_p = x2lph;
x1rph_p = x1rph;
x2rph_p = x2rph;
v1lph_p = v1lph;
v2lph_p = v2lph;
v1rph_p = v1rph;
v2rph_p = v2rph;

sL0 = sL(i);
sR0 = sR(i);
end
```

Appendix D

Inverse kinematic function code

```
function [sL,sR,thetaL,thetaR] =
VFinvkin(x1l_s,x2l_s,x1r_s,x2r_s,sL0,sR0,relax)

%Define geometry of exp. vocal fold model
alphaL =        1.5708;
betaL =     -1.0990;
alphaR =        -1.5708;
betaR =     1.0990;
RL =        15.0825;
RE =        16.9321;
FRE =       14.8050;
FRL =       22.5000;

%RIGHT VOCAL FOLD SOLUTION
s_j = sR0; %use previous slide position as  initial guess for solution
s_jm1 = sR0+0.5; %change slightly from 0 to remove singularity of s_j=0
count = 0;
%Newton-Raphson solver loop
while(abs(s_j-s_jm1)>0.001)
    s_jm1=s_j;
    %Function
    f   =    real(RL*cos(betaR-alphaR-acos((s_jm1-FRE-x2r_s)/RE))+FRL-
       s_jm1+x1r_s);
    %Derivative
    fp  =   real((RL*sin(betaR-alphaR-acos((s_jm1-FRE-x2r_s)/RE))./sqrt
       (1-((s_jm1-FRE-x2r_s)/RE).^2))-1);
    %Relaxed N-R solution
    s_j = s_jm1+relax*f/fp;
    count = count+1;
```

```
end
%Right slide position found
sR = s_j;

%check for singularity in acos() function
if abs( (sR-FRE-x2r_s)/RE - 1) < 0.0001
    thetaR = real(-betaR);
else
    thetaR = real(acos( (sR-FRE-x2r_s)/RE) - betaR);
end

% LEFT VOCAL FOLD SOLUTION
s_j = sL0; %use previous slide position as  initial guess for solution
s_jm1 = sL0+0.5;  %change slightly from 0 to remove singularity of s_j=0
count = 0;
%Newton-Raphson solver loop
while(abs(s_j-s_jm1)>0.001)
    s_jm1=s_j;
    %Function
    f   =    real(RL*cos(alphaL-betaL-acos((x2l_s+s_jm1-FRE)/RE))+FRL-
       x1l_s-s_jm1);
        %Derivative
    fp  =   real((RL*sin(alphaL-betaL-acos((x2l_s+s_jm1-FRE)/RE))/sqrt
       (1-((x2l_s+s_jm1-FRE)/RE).^2))-1);
    %Relaxed N-R solution
    s_j = s_jm1+relax*f/fp;
    count = count+1;
end
%Left slide position found
sL = s_j;
thetaL = -1*(acos( (x2l_s + sL - FRE)/RE) + betaL);
```